



UNIVERSITÀ  
DEGLI STUDI  
FIRENZE

International doctorate in  
Atomic and Molecular Photonics

CYCLE XXXIII

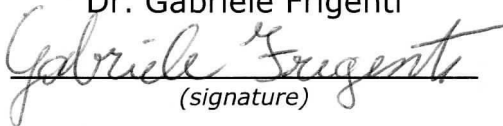
COORDINATOR Prof. Francesco Saverio Cataliotti

Microbubble resonators for sensing and  
light generation applications

Academic Discipline (SSD) FIS/03

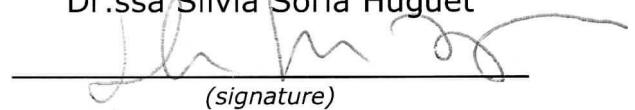
**Doctoral Candidate**

Dr. Gabriele Frigenti

  
(signature)

**Supervisor**

Dr.ssa Silvia Soria Huguet

  
(signature)

**Co-Supervisor**

Dr.ssa Costanza Toninelli

  
(signature)

**Co-Supervisor**

Dr. Gualtiero Nunzi Conti

  
(signature)

**Coordinator**

Prof. Francesco Saverio Cataliotti

  
(signature)

Years 2017/2020

---

# Contents

<b>Contents</b>	<b>iii</b>
<b>List of Abbreviations</b>	<b>v</b>
<b>List of Figures</b>	<b>vii</b>
<b>Abstract</b>	<b>ix</b>
<b>1 Introduction</b>	<b>1</b>
1.1 Whispering Gallery mode resonators overview . . . . .	1
1.2 The microbubble resonator . . . . .	3
1.3 Biomedical photoacoustics . . . . .	5
1.4 Single-photon sources . . . . .	9
<b>2 Whispering Gallery modes of a microbubble resonator</b>	<b>13</b>
2.1 Modelling the microbubble . . . . .	13
2.2 Formal solution . . . . .	15
2.3 Spectrum of the MBR system . . . . .	16
2.4 Energy density . . . . .	19
2.5 Waveguide coupling . . . . .	25
2.6 Modal volume . . . . .	29
2.7 Conclusions . . . . .	30
<b>3 Photoacoustic sensing</b>	<b>33</b>
3.1 The experimental setup . . . . .	33
3.2 Static contrast agent configuration . . . . .	39
3.3 Flowing contrast agent configuration . . . . .	47
3.4 Conclusions . . . . .	50
<b>4 Absorption sensing</b>	<b>53</b>
4.1 The experimental setup . . . . .	53
4.2 Experiment description . . . . .	57
4.3 Conclusions . . . . .	66

<b>5 Light collection from single-photon sources</b>	<b>67</b>
5.1 Dibenzoterrylene molecules . . . . .	67
5.2 The microbubble implementation . . . . .	69
5.3 Evaluating system performance . . . . .	71
5.4 Conclusions . . . . .	76
<b>6 Conclusions and outlook</b>	<b>77</b>
<b>A Details on derivation of the microbubble WGMs</b>	<b>79</b>
A.1 Wave equation in a homogeneous medium . . . . .	79
A.2 Field matching and characteristic equation . . . . .	84
A.3 Computation of the radial function $F$ . . . . .	88
<b>List of Publications</b>	<b>91</b>
<b>Bibliography</b>	<b>93</b>

# List of Abbreviations

WGM	Whispering Gallery mode
MBR	Microbubble resonator
SPS	Single photon source
PA	Photoacoustic
GNRs	Gold nanorods
DBT	Dibenzoterrylene
ZPL	Zero phonon line
TE	Transverse electric
TM	Transverse magnetic
FEM	Finite element method
SEM	Scanning electron microscope



# List of Figures

1.1	Examples of Whispering Gallery mode resonators . . . . .	2
1.2	Microbubble fabrication and characterisation . . . . .	4
1.3	Photoacoustic images of biological tissues . . . . .	7
1.4	Possible coupling strategies for single photon sources . . . . .	10
2.1	Modelling of the microbubble resonator . . . . .	14
2.2	Optical spectrum of the microbubble resonator . . . . .	17
2.3	Comparison of TE and TM spectra . . . . .	18
2.4	Angular dependency of the energy density . . . . .	21
2.5	Radial dependency of the energy density . . . . .	22
2.6	Radial dependency for high order modes . . . . .	23
2.7	Distribution of the energy density . . . . .	24
2.8	Overlap between a microbubble WGM and a fiber mode . . . . .	26
2.9	Fiber coupling of different MBR modes . . . . .	28
2.10	Modal volume for TE and TM modes . . . . .	30
3.1	Setup for PA sensing through an MBR . . . . .	34
3.2	Characterisation of the beam focusing . . . . .	36
3.3	Detection of the pulse energy . . . . .	37
3.4	Checking PA generation with an ultrasound transducer . . . . .	38
3.5	Read-out of the PA wave through the MBR transducer . . . . .	40
3.6	Measurement of the PA response trend . . . . .	42
3.7	Fourier spectrum of the MBR read-out signal . . . . .	43
3.8	Results of the FEM simulation reproducing the MBR detection . . . . .	45
3.9	Miniaturisation predictions . . . . .	46
3.10	MBR transmission for the flow configuration . . . . .	48
3.11	PA wave read-out through Fourier analysis . . . . .	49
3.12	PA response trend for the flow configuration . . . . .	50
4.1	Setup for absorption sensing through an MBR . . . . .	54
4.2	Characterisation of the beam focusing . . . . .	56
4.3	Characterisation of the laser source . . . . .	57
4.4	Measuring the absorption-induced optical shift . . . . .	59

4.5	Preliminary reconstruction of the nanoparticles absorption . . . . .	60
4.6	Real-time reconstruction of the temperature trend . . . . .	61
4.7	Thermal contribution of the nanoparticles and the host liquid . . . . .	63
4.8	Nanoparticles absorption spectrum measured by the MBR . . . . .	65
5.1	Dibenzoterrylene fluorescence . . . . .	68
5.2	Sketch of the quantum optics experiment . . . . .	69
5.3	Coupling between a WGM and a DBT molecule . . . . .	72
5.4	Single-photon emission figures of merit . . . . .	74



# Abstract

Microbubble resonators (MBR) are micro-sized optical resonators belonging to the Whispering Gallery mode (WGM) family. On practical terms, these resonators are produced by inflating a glass capillary, with the resulting spherical bulge being the resonator itself. In analogy with other WGM resonators, MBRs are realised with highly transparent material (e.g. silica), have a very small footprint (below 0.5 mm) and their optical modes are concentrated on circular path running along the MBR equator. These features lead to high quality factors, high finesse and little modal volumes. At variance with other WGM resonators, MBRs have a hollow structure and through their capillary stem can be easily filled with liquids or gasses. This allows the MBR to be used as optical sensor to study the properties of the hosted fluid (e.g. viscosity, refractive index), or study the properties of particles dissolved into the fluid.

In this thesis MBRs are studied for their implementation as optical sensors for the characterisation of photoacoustic (PA) contrast agents and then as micro-cavities for the collection of the emission from single-photon sources (SPS).

The first study is experimental and focuses on two experiments aimed at implementing the MBR as an all-optical transducer for the characterisation of photoacoustic (PA) contrast agents. In both experiments the MBR plays the double role of vial containing the PA agent and of optical sensor, allowing to reach ultra-compact configurations with an active volume below 100 nl. More specifically, in the first experiment the MBR resonances are used to sense the ultrasound wave produced by the PA contrast agent and deduce its photostability curve. To challenge the system, this measurement is performed in a static and in and in a flow-cytometry configuration (i.e. contrast agent running through the MBR), showing that in both cases the photostability curve is measurable. In prospective, the miniaturisation of the MBR promises better performance and the mechanical spectrum, which has an important role in the sensing mechanism, could be exploited through positive interference or lock-in amplification. In addition to the characterisation of PA contrast agents, the system could be implemented in the analysis of flowing samples (e.g. the measurement of blood cells oxygenation or the detection of venous thrombi and/or circulating tumour cells through a minimal blood draw).

In the second experiment, instead, the MBR allows to reconstruct the contrast agent absorption spectrum through a thermometric measurement. In particular, the MBR resonance are used to track the temperature shift generated by the PA agent optical

absorption, making the system insensitive towards light scattering from both the PA agent or the host solution. This aspect is particularly interesting for applications aimed at the analysis of highly opaque biological samples. In addition, due to the similarities between the two setups, it is possible to envisage the combination of the two experiments to perform the two characterisation measurements in quick succession.

At variance with the first, the second study of this thesis is theoretical/computational and focuses on the implementation of an MBR as a micro-cavity for the collection of fluorescence from a single-photon sources. In this study, the reference quantum emitters are dibenzoterrylene (DBT) molecules, which are known and efficient quantum emitters under investigation for the implementation into photonic devices. The presented feasibility study evaluates the performance of the system based on the indistinguishability of the produced photons and on the overall photon collection efficiency. The results of the computation are promising for an actual implementation of the system, since strong coupling regime is reached at cryogenic configuration, but also room temperature indistinguishability remains high. In addition, the system has an overall better performance with respect to a cavity-less configuration.

To support this part of the thesis work, an analytical theory of the MBR modes extending the microsphere case to the microbubble case was developed, since no similar dissertation was found in literature. The theory is developed formally and is aimed at the computation of key quantities related to the DBT-WGM coupling, such as the volume and the distribution of the WGM.

This document is structured in six Chapters. Chapter 1 is an introduction that contextualises the thesis work and briefly summarises the topic area where the MBR implementation contributes. Chapter 2 presents the modelling used to describe the MBR modes. In Chapter 3 the first experiment aimed at the detection of a PA wave from contrast agents is described, while in Chapter 4 the second experiment reconstructing the absorption spectrum through the thermometric measurements is described. Then, in Chapter 5, the theoretical study on the light collection from quantum emitters is discussed. Finally, Chapter 6 is dedicated to conclusions and outlooks.

# Chapter 1

## Introduction

This Chapter focuses on presenting the features of a MicroBubble Resonator (MBR) and contextualise this thesis work. In particular, Section 1.1 and Section 1.2 give an overview of the properties of Whispering Gallery mode (WGM) resonators and of the MBRs, respectively. Then, Section 1.4 and Section 1.3 give a brief description of the research fields to which this thesis work contributes with the MBR implementation: biomedical photoacoustics (Section 1.3) and control of single photon sources (Section 1.4).

### 1.1 Whispering Gallery mode resonators overview

At the start of the twentieth century, Lord Rayleigh studied the acoustics of the Saint Paul's Cathedral in London and explained the singular acoustic phenomenon taking place in the gallery under the dome. In this place, in fact, a word whispered against the gallery walls could be heard by a listener regardless of its position along the 105-meter walkway. For this peculiar feature the gallery was named “Whispering Gallery” and, even today, this acoustic phenomenon represents a fascinating attraction for the cathedral visitors. Lord Rayleigh showed that this phenomenon was caused by the curved walls of the gallery, which continuously refocused and guided the acoustic wave during its propagation [1, 2]. In particular, this curved guiding forced the acoustic wave to run along gallery walls, producing a “wall sticking” effect, and proved to be energy-efficient, allowing the wave to travel for the entire walkway length. With the advent of laser technology and the possibility of refining extremely pure glasses, it was possible to translate this phenomenon into optics, using curved dielectric surfaces to efficiently guide an electromagnetic wave. In analogy with their acoustic counterpart, these optical modes were named *Whispering Gallery modes* (WGMs) [3, 4, 5].

There is a wide variety of systems that can support optical WGMs (cfr. Figure 1.1), such as microspheres [6, 7, 8, 9, 10, 11, 12], microdroplets [13, 14] microdisks [15], microtoroids [16], microrings [17] and micropillars [18, 19]. In addition, even hollow structures are possible such as microbubbles [20, 21, 22] and microbottles [23, 24, 25]. In all cases, the systems present a cylindrical symmetry around one axis, have curved

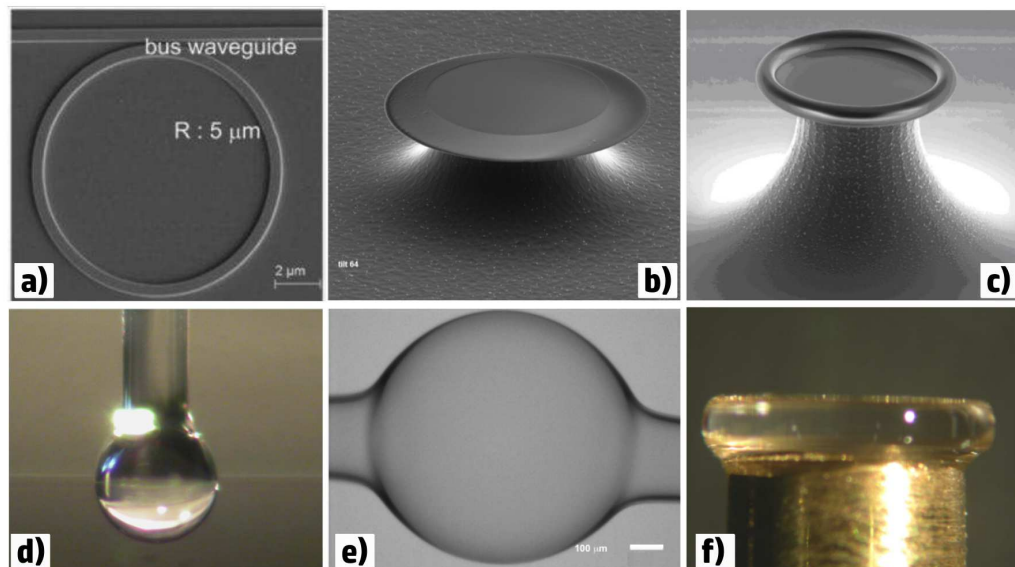


Figure 1.1: Series of panels showing examples of WGM resonators (adapted from [26]). Moving from left to right one has (a) an embedded microring resonator coupled to an embedded waveguide, (b) a microdisk, (c) a micro-toroid, (d) a microsphere, (e) a microbubble, and (f) a niobate crystalline milli-disk.

dielectric surfaces and present an high refractive index contrast with the surrounding medium. These features allow the formation of the optical WGMs, which are produced by the combination of the total internal refraction and the guiding effect provided by the curved interfaces. As consequence, WGMs are concentrated in close proximity to the dielectric interfaces (“wall sticking”), while running circular paths around the symmetry axis. In this regard, WGMs can be easily and effectively visualised as rings of light localised at the dielectric boundaries.

The physical process leading to the WGMs formation is the interference of the guided wave with itself on these closed paths [27, 28, 29, 30]. This formation is analogous to the one happening in interferometers (e.g. Gires-Tournis, bowtie), where the guiding is instead provided by a set of mirrors. As consequence, WGMs form a set of discrete confined electromagnetic modes and the systems sustaining them are called *Whispering Galley mode resonators*. Since the wave must run several round trips without significant attenuation for the interference process to happen, WGM resonators must be fabricated with low-loss materials and must have a little footprint.

More formally, the WGMs are found as solutions of the vectorial Helmholtz equations after the application of appropriate boundary conditions on both the electric and the magnetic fields. In particular, this resolution defines both the resonance wavelengths of the WGMs as well as their spatial distributions. As a general feature, WGMs are mostly localised within the resonator physical boundary (i.e. within the dielectric surfaces), but they also have a very small fraction extending in the surrounding environment

as evanescent tails. In practical terms, these evanescent tails play an important role since they allow to couple the WGMs to an external waveguide and then inject and/or extract light from the WGMs. There are different waveguides and strategies that can be implemented to achieve the WGM-waveguide coupling, but all implementation share two main goals: achieving both a good spatial overlap and phase matching between the WGMs and the waveguide mode.

Once that the coupling is achieved, laser light can be injected into the resonator to excite its WGM resonances. By scanning the laser wavelength and recording the system transmission, it is then possible to observe the lineshape of the WGM resonances and define a series of parameters to characterise the resonator. This list of figures-of-merit is inherited from interferometry and comprises, for example, the quality factor, the finesse, the contrast (or visibility), the full-width half-maximum (FWHM) and the free spectral range. Among these parameters, the quality factor, the finesse and the contrast are the most important in applications, since they quantify the sharpness of the WGM resonances, the average number of photon round-trips and the loaded energy in the WGM, respectively.

Due to their sharp optical spectrum, their little modal volume and little footprint, WGM resonators have found applications in several fields [27, 28, 29, 30, 31, 32, 33]. For example, they have been used as optical sensors to measure physical and chemical perturbation [34, 35, 36], as optical filters to stabilise opto-electrical oscillators and laser sources, and optical micro-cavities for the generation of non-linear effects (e.g. Kerr frequency combs, Brillouin scattering) or the coupling to quantum emitters. In particular, these last two applications benefit also from the small modal volume of the WGMs, which can reduce the threshold intensity of the non-linear effect and increase the WGM-emitter coupling. Finally, the little footprint of the resonator is promising for the development for the development of ultra compact systems or even on-chip devices [37].

## 1.2 The microbubble resonator

This thesis focuses on the implementation of microbubble resonators (MBR), which are hollow WGM resonators produced by the inflation of a glass capillary. In practical terms, this inflation is achieved by pressuring the capillary with with an inert gas (e.g. nitrogen) and then rapidly heating it (e.g. through a laser pulse [20] or an electric discharge [21]). This rapid heating produces a softening of the capillary walls, which expand to a spherical bulge due to the internal pressure: this bubble-shaped bulge is the resonator itself.

At variance with other WGM resonators, MBRs are hollow and can be filled with liquids or gasses through their capillary stem [38, 39, 40, 41, 42, 43, 44, 45]. For this reason, MBR are ideal optical sensor for studying the properties of the hosted fluid, focusing, for example, on their viscosity [40, 42] or their refractive index [46, 38]. In addition, if particles are dissolved into the fluid, their interaction with the WGM internal evanescent tail can be exploited to make the MBR an optical sensor for chemistry or

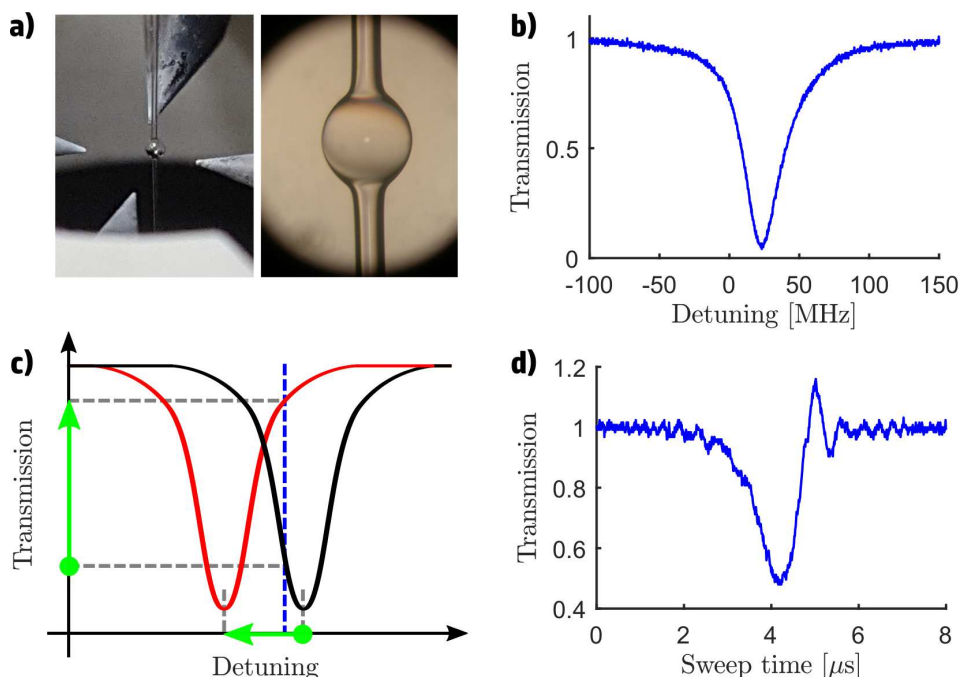


Figure 1.2: Panel a: wide shot showing the MBR and the electrodes used for the arch discharge (left), and microscope image of the MBR (right). Panel b: typical profile of an MBR resonance. Panel c: sketch highlighting the optical sensing mechanism assuming to lock the probe laser to specific wavelength (blue dashed line). Panel d: cavity ring down profile of an MBR resonance

biochemistry [47, 44]. Finally, due to their minute mass and their sharp mechanical spectrum, MBRs are interesting platforms for fundamental studies in optomechanics [48, 49, 43, 50].

In this thesis, the MBRs are studied both from a theoretical and an experimental point view. In particular, Chapter 2 deduces the WGM of the microbubble and Chapter 5 uses these results to study the potential of the MBR as a micro-cavity for the control of single-photon sources. Chapters 3 and 4, instead, describe the implementation of an MBR for the detection of a photoacoustic wave generated by nanoparticles [51, 52] and for the measurement of their absorption spectrum, respectively. In the following of this Section, the fabrication and the characterisation of the MBRs used for the experiments of Chapters 3 and 4 are discussed. In prospective, these methods will also be tested for the implementation of the MBR for the control of single-photon sources.

The MBRs used in this thesis work were fabricated with the arc discharge technique described in [21]. They were produced from fused silica capillaries (Z-FSS-200280 and Z-FSS-100-165 from Postnova Analytics GmbH, Landsberg, Germany) and their typical radius fell in the [200  $\mu\text{m}$  - 250  $\mu\text{m}$ ] range. Panel a of Figure 1.2 shows one of the MBRs mounted on the discharge system after the inflation process.

After the fabrication process, the MBR was characterised by coupling it to a home-

made tapered fiber [53] and then scanning its WGM spectrum through a tunable laser source (Tunics plus, NetTest; spectral range 1500 nm - 1640 nm, in-fiber emission). As shown in Panel b of Figure 1.2 by a representative resonance, the MBR resonances show a high contrast (0.95), a high quality factor ( $6.0 \cdot 10^6$ ) and a narrow FWHM (32 MHz), making them promising for optical sensing. In particular, if a small perturbation has to be detected, the steep resonance fringe allows to read little shifts of the resonance position as significant changes in the system transmission (cfr. panel c of Figure 1.2, red curve). Otherwise, if large perturbations has to be detected, the steepness allows to accurately define the position of the resonance on a larger detuning scale (cfr. panel c of Figure 1.2, blue curve). As shown in Chapters 3 and 4, both conditions were found during the experiments.

Finally, it is important to highlight that these promising optical features are a consequence of the little value of the intrinsic losses and the coupling losses of the system as well as their little difference (*critical coupling*). More in detail, the intrinsic losses ( $\eta^2$ ) are the ones connected with the quality of the fabrication process and account for the absorption of the material making up the MBR, the scattering produced by the roughness of the MBR surface and the contaminations of the MBR surface by impurities (e.g. dust). Coupling losses ( $\kappa^2$ ), instead, quantify the energy exchange between the waveguide and the MBR. These quantities can be retrieved by performing a fast wavelength scan of the WGM resonance and analysing the resulting cavity ring down (CRD) profile [54, 55]. Panel d of Figure 1.2 shows an example of these CRD profiles, whose analysis leads to  $\eta^2 = 2.8 \cdot 10^{-5}$  and  $\kappa^2 = 6.4 \cdot 10^{-6}$ , proving the overall small values and little difference. In addition, the intrinsic losses  $\eta^2$  can be used to compute an intrinsic quality factor  $Q_0 = 3.3 \cdot 10^8$ , proving the high quality of the the arc discharge fabrication process.

### 1.3 Biomedical photoacoustics

The first studies on the generation of sound waves through the light-matter interaction are dated back in the 1870-1880 decade, and are especially associated with the activity of Alexander Graham Bell on telecommunications. In particular, using the photoconductivity properties of selenium foils discovered by Willoughby Smith in 1873, Bell designed an ingenious device called the *phonophone*, which allowed to translate speech into light modulation and then light modulation again into speech, achieving the first wireless phone call in history [56]. This result sparked the interest of the scientific community of the time and several experimental and theoretical investigations of the interaction between sound and light were performed. After this initial boost, however, the subject became less investigated, since a quantitative approach to the subject was limited by the technology available at the time (i.e. mostly due to the lack of sensitive microphones and bright light sources). This technology barrier was overcome in the XX century, with the advent of capacitive microphones and of laser sources, which brought new life to the subject and allowed the implementation of the photoacoustic effect in several fields [56].

In a nutshell, the photoacoustic (PA) effect is the emission of an acoustic shockwave from an optical absorber after its excitation with a short laser pulse. The emission of the shockwave is the final step of a complex chain of thermo-elastic processes involving the absorber and the host material surrounding it. On a general level, this chain starts with the transfer of heat from the absorber to the host material in its proximity, producing a local change in density and pressure (thermo-elastic conversion). Then, this perturbation in density and pressure propagates away from the absorber and through the remaining part of the host material as an acoustic wave. For basic studies, the PA effect is an effective tool for the investigation of the absorption spectrum of the absorber, its elastic properties and its non-radiative de-excitation, since it combines high optical selectivity and mechanical relaxation.

In recent times, the effect has been implemented with success in the biomedical field for its optical specificity towards optical absorption and unhindered propagation of acoustic waves into biological tissues. In the biomedical context, the typical host material is a biological tissue (e.g. skin, blood), the absorber is a particle naturally present in the tissue (e.g. melanin, hemoglobin, lipids, collagen) or artificially inserted into it (e.g. noble-metal, carbon-based, semiconducting polymer nanoparticles; organic dyes), and the objective is to diagnose the health state of a tissue by reading-out the PA wave or use the PA wave to apply a treatment. One of the most successful technique in this regard is PA imaging, which allows to produce an image of a biological structure by reconstructing the optical absorption map of the sample [57, 58, 59, 60] and can be easily adapted to a treatment protocol in the case of cancerous tissue, effectively combining imaging/diagnosis and treatment (theranostics) [61, 62, 63, 64, 65, 66].

In practise, the PA image is reconstructed by scanning the biological sample with a pulsed laser and recording the ultrasound wave generated by each illuminated point, in analogy with a raster scan in optical microscopy. To a microscopic level, the ultrasound wave is produced by the de-excitation of the optical absorbers making up or marking the biological structure of interest [67]. Figure 1.3 exemplifies this concept in two cases. In panel a, a PA image of the red cells in a blood sample is obtained by searching the PA response of haemoglobin [68]. In panel b, instead, an in-vivo image of a group of veins is obtained: even in this case the targeted absorber is the haemoglobin in the red cells [60].

In general, the targeted optical absorber is referred to as *PA contrast agent* because its PA response highlights the structure of interest with respect to the other elements in the sample. As shown with the examples of Figure 1.3, PA contrast agents can be naturally present in biological tissues, but they can also be artificially synthesised [69, 70, 71, 72, 73, 70, 74]. In particular, these synthetic agents can be inserted into the tissue of interest to increase its PA response or simply elicit one if the tissue is naturally lacking of PA agents. In addition to these implementation, synthetic PA agents are also used for the treatment of cancerous tissues through hyperthermia [63, 64, 65]. In this case, after an initial imaging phase, the cancerous tissues is illuminated by CW light to overheat the synthetic PA agent and induce thermal damage into the tumour cells.

Due to its promising combination of imaging/diagnosis and treatment, PA imaging



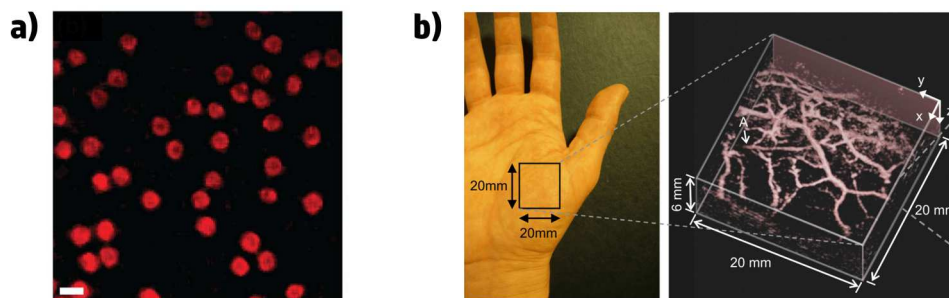


Figure 1.3: Panel a shows the PA image of the red cells in a blood sample (adapted from [68]), while panel b shows an in-vivo PA image of a group of veins (adapted from [60]). In both cases the targeted PA contrast agent is the haemoglobin in the red cells.

is greatly investigated to improve its performances. In this regard, a first improvement roadmap is the development of new PA detectors. The most straightforward detectors that one can think of using in PA imaging setup are piezoelectric ultrasound transducers. Due to their widespread use and advanced industry, these detectors are available on the market in various designs, allowing to cover various possibilities in terms of detection figures of merit (e.g. bandwidth, acceptance angle, sensitivity). However, these transducer are typically designed for echographic tests and therefore their specifications do not match the levels required for PA imaging [75]. In addition, they are difficult to miniaturize because this process leads to strong degradation in performances. Optical detection of the PA wave represents a solution to these problems, since it proved to combine miniaturisation with high-performances [75, 68, 60]. One interesting possibility in this regard is given by embedded WGM microrings, which combine a wide detection bandwidth with an extremely small detection area [76, 77, 68, 60].

A second improvement roadmap for PA imaging is the development of new PA contrast agents. In this case, the challenge is to design and synthesize contrast agents having an increased PA response during the imaging phase and an increased heat release during the therapeutic phase. Due to the complexity of the PA process, which is made up of an articulated chain of thermoelastic processes [58, 78, 79], this task is not easy and is an open problem that interests both chemistry and material science. On top of this fundamental considerations, contrast agents must also comply to low-toxicity requirements for their usage in a clinical scenario, meaning that also biology is involved in their development. As a matter of fact, the development of PA contrast agents has to be tackled with a multidisciplinary approach due to its multi-faceted challenge.

Among the various possibilities tested in research gold nanorods (GNR) are an interesting option, as proved by their long implementation history [72, 71, 74, 69, 70, 73]. Their main advantages are the ease of synthesis, the possibility to finely tune their absorption wavelength during the synthesis process and their high absorption cross section. In particular, the absorption wavelength of a GNR is fixed by its aspect ratio, which is the ratio between the longitudinal and the transversal length. Typically, the target value is close to 4, to produce absorption in the [650 nm - 1300 nm] spectral window. This

window is particularly important for clinical applications and bio-optics in general, since biological tissue have maximum transmission for these wavelengths, allowing a deeper penetration of the laser beam and therefore a deeper imaging/treatment. In terms of improvements, an important goal is the increase of their photostability threshold (i.e. the maximum optical exposure before particle reshaping), which would allow the illumination with higher fluences and lead to a performance increase for both imaging and therapy [80, 81, 82].

In this context, the MBR system combines a series of promising features for its implementation as an optical PA transducer aimed at the characterisation (and possibly the development) of contrast agents. On a general level, in analogy with other optical transducers [83, 84, 85, 40, 42], the MBR system can detect the PA wave generated by a contrast agent through the optical shift induced in its WGM resonances. More specifically, by impinging on the MBR walls, the PA wave perturbs the MBR radius and the walls refractive index, leading ultimately to the optical shift. Indeed, this detection mechanism is similar to the one of other optical transducers, but the hollowness of the MBR allows for a unique configuration regarding the positioning of the contrast agent. At variance with both piezoelectric ultrasound transducers and other WGM transducers, in fact, the MBR can host internally the contrast agent and therefore can forgo any acoustic impedance-matching medium. As consequence, this allows to work with minimal samples due to the MBR minute volume, and it also allows a more direct detection of the PA wave, without the mediation of the matching medium. Another important and unique feature of the MBR system is the presence of mechanical resonances, which can be used to filter mechanical environmental noise and/or to achieve positive mechanical interference. The implementation here outlined is extensively discussed in Chapter 3. In particular, the first part of this Chapter aims at proving the sensitivity of the MBR towards the PA wave through a proof-of-concept experiment, and the second part challenges the MBR in an application-like context: a flow-cytometry configuration [86, 87, 88, 90].

Finally, by adopting a similar implementation, MBRs can also perform a measurement of the contrast agent absorption spectrum. In this case, the MBR reconstructs the agent absorption spectrum by detecting the temperature increase produced by the optical absorption. In practise, this temperature increase is detected by reading the shift of a WGM resonance, effectively implementing the MBR as a thermo-optical sensor. Even in this case, the sensing element are the MBR walls, which are uniformly heated and deformed by the contrast agent temperature increase and expansion. Since the measurement is based on a thermal phenomenon and scattering cannot rise the contrast agent temperature, this implementation implies sensitivity only towards the contrast agent absorption spectrum, and not towards its scattering spectrum. This is at variance with measurements based on optical extinction (e.g. spectrophotometry), which is produced by both absorption and scattering, and represents a characteristic feature for the MBR system. Chapter 4 describes the implementation here outlined using two different experimental approaches: one where the probing laser is constantly scanning the WGM resonances and one where it is positioned on the side of the resonance fringe.

## 1.4 Single-photon sources

The stringent requirements on secure communications, the management of massive data amounts and the ever-growing complexity of scientific models are strong drivers for the development of quantum technologies [91, 92, 93, 94, 95]. The building block of these technologies is the quantum bit (simply referred to as *qubit*), which can be generally defined as a two-level system whose state  $|\psi\rangle$  can be prepared and manipulated with precision and reliability. At variance with the classical bit, which can only be prepared into two states (0 or 1), the qubit can be prepared in a superposition of the two levels ( $|0\rangle$  and  $|1\rangle$ ) by taking advantage of the superposition principle of quantum mechanics:  $|\psi\rangle = \alpha|0\rangle + \beta|1\rangle$ . When considering all the  $(\alpha, \beta)$  combinations (both in terms of phase and amplitude), it is straightforward to understand that a qubit can single-handedly represent a massive amount of information. In addition, when more qubits are available, it is possible to entangle their states and maintain information correspondence even when the two qubits are separated by a great distance. This feature, which is intrinsically associated with the quantum nature of the qubit, is impossible to replicate with classical bits and represents the most unique and revolutionary aspect for these new technologies.

In addition to solid-state implementations, where the spin state of an atom, a ion, a nucleus or a crystalline defect is used as the qubit state  $|\psi\rangle$ , a promising qubit implementation is represented by single-photon wavepackets. In this case, the quantum state  $|\psi\rangle$  can be represented by the polarisation state of the photon (e.g.  $|0\rangle$  for the horizontal polarisation and  $|1\rangle$  the vertical polarisation  $|1\rangle$ ) or by the its presence/absence in the wave packet (in this case  $|0\rangle$  and  $|1\rangle$  are the vacuum and one-photon Fock state, respectively). An important advantage in using single-photon wavepackets as qubits is their natural propagative nature, which represents an incredibly promising feature for quantum communication. A challenging aspect, instead, is represented by the generation of these wavepackets with precision and reliability, in order for them to undergo successive processing through optical ports (e.g. an Hong-Ou-Mandel interferometer to produce photon coalescence).

Great research effort was made to develop sources that could reliably produce this non-trivial light states, with the ultimate goal being the realisation of the so-called *photon gun*: a source capable of producing on-demand single-photon wavepackets with 100% certainty. Many single-photon sources (SPS) have been investigated with this prospective [96, 97], with the most promising systems being nano-emitters such as atoms, ions, organic molecules [98, 99, 100, 101], quantum dots [102, 103], crystal defects [104, 105] and nanocrystals. For these systems, the physical process leading to the emission of single-photons wavepackets is the relaxation fluorescence (i.e. spontaneous emission) following the pumping of the system into an excited state. The three main parameters used to characterise SPS emission are: antibunching, indistinguishability and quantum efficiency (also referred to as *quantum yield*). More in detail, antibunching defines the “quantumness” of the SPS emission by estimating the temporal separation between each wavepacket, which has to be greater than the one associated with laser light and thermal light (hence the name). Indistinguishability, instead, defines the degree of equality

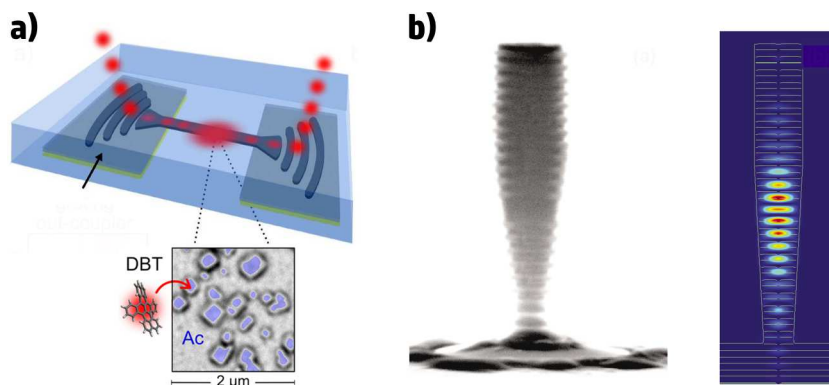


Figure 1.4: Panel a: sketch of a waveguide system used to collect the emission from dibenzoterylene (DBT) molecules (adapted from [106, 101]). Panel b: micropost resonator used to collect the emission from an embedded quantum dot (on the left: SEM image of the micropost cavity, on the right field distribution of the fundamental mode) (adapted from [107]).

between the wavepackets and its a very important parameter for successive photon processing, since quantum interference effects require a high level of indistinguishability to happen (e.g. photon coalescence). Finally, the quantum efficiency quantifies the number of generated photons with respect to the number of excitation cycles and its another important parameter with respect to applications, since it defines the energy efficiency of the SPS as well as the maximum information rate that the SPS can provide. For comparison, the ideal photon gun has a quantum efficiency equal to one (i.e. on-demand emission).

On top of this efficiency, one has also to account for the collection efficiency, which the is the ratio between the collected and the generated photons. At variance with the parameters previously defined, collection efficiency is mostly influenced by the environment surrounding the SPS and, in particular, by the presence of photonics structures. These structures, in fact, can redirect the free-space emission of the SPS into well-defined spatial modes, allowing for a more efficient collection. Two common photonics structures used for this purpose are micro-cavities [108, 109, 110, 28, 111, 112, 113, 114, 115, 107, 116, 117] and waveguides [118, 119, 106], but even more straightforward approaches like the use of solid immersion lenses proved to be effective in redefining the SPS emission [120]. In addition to enhanced light collection, micro-cavities can also modify the emission rate of the SPS through Purcell effect, therefore allowing to exceed the SPS natural emission rate.

In this context, an MBR can be envisaged as a micro-cavity for both the enhancement of the SPS emission and the improvement of light collection, with the microbubble WGMs acting as the cavity modes [28, 115, 117, 114, 113, 111]. In particular, taking again advantage of the hollowness of the MBR, the SPS can be placed inside of the MBR, achieving a configuration where the internal evanescent tail of the WGM couples the WGM to the SPS, while the external evanescent tail couples the WGM to a waveguide.

In this way, the WGM can both collect light efficiently from the SPS and, at the same time, launch it into a guiding structure (i.e. the waveguide) for detection or processing. In Chapter 5 this implementation is studied from a theoretical/computational point of view using the results of Chapter 2 as the computational foundations. In particular, the discussion of Chapter 5 represents a feasibility study for the implementation of the experimental scheme here outlined, and focuses on deducing the collection efficiency and the photon indistinguishability. The single-photon sources selected for this study are dibenzoterrylene (DBT) molecules, which are organic molecules belonging to the family of polycyclic aromatic hydrocarbons (PAH). These molecules are known to be efficient quantum emitters both at room and cryogenic temperatures and are under study for the implementation in photonic devices [121, 106, 101]. DBT molecules are typically embedded in a PAH matrix to make them photo-stable and photo-resistant and this aspect can be exploited for the MBR configuration. In fact, the PAH matrix can be used as a suspension material to infiltrate the DBTs inside the MBR, in analogy with other experimental configurations [122].



## Chapter 2

# Whispering Gallery modes of a microbubble resonator

This Chapter presents the derivation of the Whispering Gallery modes (WGM) of a microbubble resonator (MBR) and the computation of quantities of interest for the design of experiments. In particular, the Chapter aims at evaluating the coupling of the microbubble WGMs with an external waveguide (Section 2.5) and the WGMs modal volume (Section 2.6). Both parameters, in fact, are important for the discussion of Chapter 5, where the control of single photon source through a microbubble mode is discussed. In performing these computations, other stand-alone quantities such as field distribution (Section 2.4) are also analytically deduced.

The theory used to deduce the microbubble WGMs, which is mostly concentrated in the first four Sections of the Chapter, is developed with a formal approach, using analytical expression as much as possible and resorting to numerical methods only in a few instances. This makes the theory versatile and enables finalizations that can be different from the ones here presented. This formal derivation follows the argument of [123, 124], where the WGMs of a microsphere are deduced, and constitutes an original contribution, since no similar dissertation about the MBR system was found in literature.

### 2.1 Modelling the microbubble

Before starting the derivation of the microbubble WGMs, the approximations and the assumptions used to describe the dielectric structure and the geometry of the microbubble are presented.

The microbubble system can be divided into three dielectric sectors, each representing a different part of the microbubble and each having spherical symmetry. The first sector represents the material hosted inside the MBR and it is a core sphere of refractive index  $n_c$  and radius  $R_c$ . The second sector represents the MBR walls and it is a spherical shell of refractive index  $n_w$  with internal radius  $R_c$  and thickness  $W$ , or equivalently with external radius  $R_e = R_c + W$ . Finally, the third sector represents the medium surrounding the MBR and it is a spherical shell of refractive index  $n_e$ , internal radius  $R_e$

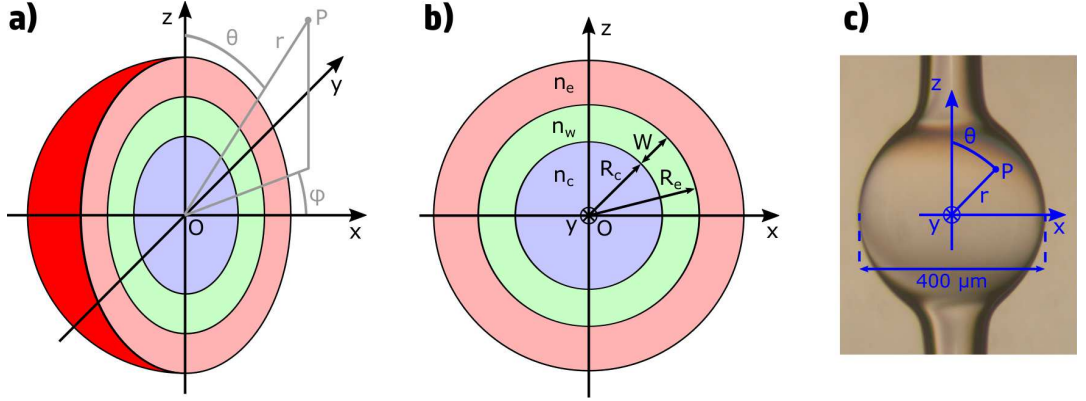


Figure 2.1: Panel a and b show two sketches of the microbubble modelling presented in this Section. Different colors are used to mark the three dielectric sectors: blue for core, green for walls, red for external medium. Panel c shows the orientation of the spherical coordinate system used in this theory with respect to a real microbubble.

and infinite thickness. The refractive indexes  $n_c$ ,  $n_w$  and  $n_e$  are assumed to be uniform within each sector and therefore the index changes abruptly at the sectors boundaries.

Panel a and b of Figure 2.1 show this modelling through a sagittal cut of the microbubble, using a 3D and 2D perspective, respectively. In these panels the dielectric sectors are depicted with different colors, the geometrical parameters are marked with arrows and the spherical coordinate system used in the following Sections is shown. In addition, panel c of Figure 2.1 shows the orientation of the coordinate system with respect to a real microbubble, highlighting the correspondence of the  $z$ -axis with the capillary stem direction and of the  $xy$  plane with the equatorial plane of the microbubble.

This modelling of the microbubble implies a uniform wall thickness along the meridians, which may appear a rather strong approximation when considering the wall tapering shown in panel c of Figure 2.1). However, this is just an apparent problem, since WGMs have a very limited extensions outside the equatorial plane (see Section 2.4) and therefore only the wall thickness at the equator is relevant for their properties. For these reasons, it is the wall thickness at the equator that has to be used as the  $W$  value. A real approximation, instead, is made by neglecting the absorption of the media making up the three sectors, therefore assuming the refractive indexes to be real-valued parameters. This approximation produces real-valued characteristic equations in Section A.2 and allows to implement basic numerical methods for their solution.

Finally, focusing on the advantages of this modelling, it is important to highlight its versatility in terms of refractive indexes and radii. In fact, since there are no constraints on these parameters, several experimental configurations can be simulated: both in terms of different materials by changing  $n_c$ ,  $n_w$  and  $n_e$ , as well as in terms of different sizes by changing  $R_c$  and  $W$  (or equivalently  $R_e$ ).



## 2.2 Formal solution

By solving the scalar Helmholtz equation in spherical coordinates and then using the Hansen method to obtain the vectorial solution to the Helmholtz equation, it is possible to write the analytical expressions for both the electric field and the magnetic fields in each sector of the MBR. For compactness, the analytical derivation leading to these expressions is described in Subsection A.1 of Appendix A and here only the main results are reported.

In particular, the scalar solution for the Helmholtz equation for a dielectric sector having index  $n$  (wavenumber  $k = k_0 n = 2\pi n/\lambda_0$ ) is written as

$$\psi(r, \theta, \phi) = F(kr) Y_{\ell,m}(\theta, \phi) \quad (2.1)$$

where the function  $F(kr)$  accounts for the radial dependence and the spherical harmonic  $Y_{\ell,m}(\theta, \phi)$  accounts for the angular dependence. As shown in Subsection 2.6, the function  $F(kr)$  is a key quantity for the computation of the modal volume, while  $Y_{\ell,m}(\theta, \phi)$  fixes the WGM distribution along the meridian.

With this factorisation, the field expressions for the TE (transverse electric) and the TM (transverse magnetic) modes are

$$\text{TE mode} \begin{cases} \mathcal{E} = F(kr) \mathbf{X}_{\ell,m} & (2.2) \\ \mathcal{H} = \frac{i}{\omega\mu_0} \left[ \frac{\ell(\ell+1)}{r} F(kr) \mathbf{Z}_{\ell,m} + \frac{1}{r} \frac{d}{dr} (rF(kr)) \mathbf{Y}_{\ell,m} \right] & (2.3) \end{cases}$$

$$\text{TM mode} \begin{cases} \mathcal{E} = \frac{\ell(\ell+1)}{kr} F(kr) \mathbf{Z}_{\ell,m} + \frac{1}{kr} \frac{d}{dr} (rF(kr)) \mathbf{Y}_{\ell,m} & (2.4) \\ \mathcal{H} = \frac{ik}{\omega\mu_0} F(kr) \mathbf{X}_{\ell,m} & (2.5) \end{cases}$$

with the auxiliary vectors  $\mathbf{X}_{\ell,m}$ ,  $\mathbf{Y}_{\ell,m}$  and  $\mathbf{Z}_{\ell,m}$  defining the spatial direction of each field component. These vectors are defined in Equations (A.22)-(A.24) and form an orthogonal base, with  $\mathbf{Z}_{\ell,m}$  being parallel to  $\hat{\mathbf{r}}$  and with  $\mathbf{X}_{\ell,m}$  and  $\mathbf{Y}_{\ell,m}$  being a combination of  $\hat{\boldsymbol{\theta}}$  and  $\hat{\boldsymbol{\phi}}$ . In particular, these definitions lead to the usual classification of TE and TM modes, since the electric field  $\mathcal{E}$  is totally tangential (i.e. orthogonal to the radial direction) in the TE case and, in turn, the magnetic field  $\mathcal{H}$  is totally tangential in the TM case.

After writing the solutions (2.2)-(2.5) for each of the three dielectric sectors making up the MBR (i.e. core, walls, external), boundary conditions have to be imposed on both the electric and the magnetic fields. This procedure is detailed in Subsection (A.2) and consists in placing a series of requirements on the four amplitudes needed to define  $F(kr)$  (cfr. Equation (A.34)). For convenience, these conditions are resumed with the matrix formalism, leading to one matrix being defined for the TE modes and one for the TM modes (cfr. Equations (A.47) and (A.50)). To guarantee the physical meaning of the four amplitudes making up the  $F(kr)$  function, these matrices must have null determinant and this leads to the characteristic equations for both mode families (cfr.

Equations (A.47) and Equations (A.50)). Since the geometry and the composition of the MBR are considered input parameters, the only unknown variables in the characteristic equations are the vacuum wavelength  $\lambda_0$  and the integer  $\ell$ , as highlighted by the explicit dependences in Equations (A.49) and (A.51)).

### 2.3 Spectrum of the MBR system

To deduce the structure of the WGM spectrum of the MBR, it is necessary to solve for  $\lambda_0$  the characteristic equations (A.49) and (A.51). Due to the presence of the Bessel functions and the high number of terms required to compute the determinant of  $\mathcal{M}_{\text{TE}}$  and  $\mathcal{M}_{\text{TM}}$  (cfr. (A.47) and (A.50)), it is not possible to find an analytical solution to these equations and therefore a numeric approach must be implemented. In practise, the resolution method consists in locking  $\ell$  and scanning  $\lambda_0$  to find a set of zeroes; then  $\ell$  is moved to another value and the process is repeated, leading to various  $\lambda_0$  sets labelled by  $\ell$ . A second index  $n = \{1, 2, 3, \dots\}$  is then used to label the solutions within each set, assigning  $n = 1$  to the highest zero (i.e longest wavelength),  $n = 2$  to the second-highest zero and so on. In the end, each solution is uniquely identified by the  $(n, \ell)$  pair and is formally referred to as  $\lambda_0^{(n, \ell)}$ .

As previously mentioned, the structural parameters (i.e radii and indexes) of the MBR are to be considered fixed parameters. The configuration here studied features an MBR made in silica ( $n_w = 1.45$ ), filled with water ( $n_c = 1.33$ ) and surrounded by air/vacuum ( $n_e = 1$ ), having an external radius  $R_e = 150 \mu\text{m}$  and a wall thickness  $W = 4 \mu\text{m}$  ( $R_c = 146 \mu\text{m}$ ). These parameters are chosen for their similarity with the experimental configuration presented in Chapter 3.

Taking the TE characteristic equation (A.49) as example and applying the previously described resolution method, one obtains the results shown in Figure 2.2. In both panels each dot represents a  $\lambda_0^{(n, \ell)}$  solution and the same color code is used in both panels to mark the  $n$  value. These solutions are obtained by scanning  $\lambda_0$  between 740 nm and 760 nm and moving  $\ell$  between 1788 and 1793 (panel a) or between 1690 and 1822 (panel b). In particular, the  $\lambda_0$  window was arbitrarily chosen, while the  $\ell$  window was chosen to be close to the approximate  $\ell$  value given by

$$\ell \approx \frac{2\pi n_w R_e}{\lambda_0}, \quad (2.6)$$

where  $\ell$  is roughly estimated as the number of oscillations around the MBR equator ( $\ell \approx 1800$  in the case here considered). The fine details defining the exact  $\ell$  range are discussed in the following. By observing the two panels, it is possible to deduce the trends associated with the two labelling indexes, which give the general structure of the solutions and therefore of the WGM spectrum of the microbubble.

Starting with panel a, for example focusing on the  $\ell = 1790$  case, it is possible to notice that an increase in  $n$  produces a decrease in wavelength (around 7 nm) or, equivalently, an increase in frequency. In addition to this, as shown in Section 2.4, each increment of  $n$  produces a new node in the radial function  $F(kr)$ , and, in the end,  $n$

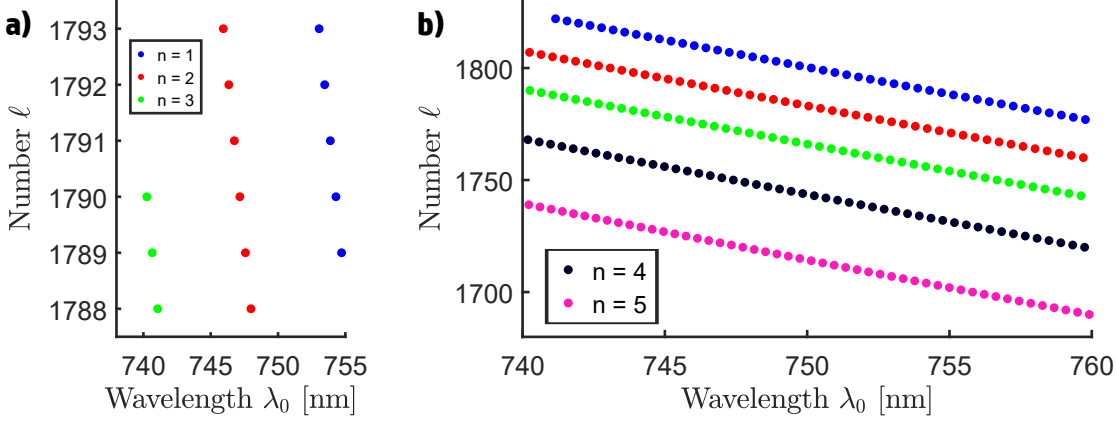


Figure 2.2: Each dot represents a numerical solution of Eq. (A.49), obtained by scanning  $\lambda_0$  between 740 nm and 760 nm for various values of  $\ell$ . The  $n$  values are marked with the same color code in both panels. The  $\ell$  set used for panel a is narrower than the one used in panel b to better highlight the structure in which the solutions organize.

equals the number of nodes incremented by 1:  $n = (\# \text{ nodes}) + 1$ . The frequency also increases if  $n$  is kept fixed and  $\ell$  is increased (cf. blue coloured  $n = 1$  branch in panel a). In particular, a one unit increment in  $\ell$  produces a decrease of 0.403 nm in the  $n = 1$  branch, which is within 2.5 % from the microbubble free spectral range estimated through the resonator size (FSR = 0.412 nm). In the end, the frequency increases with increasing  $\ell$  and with increasing  $n$ .

Moving to panel b, one can notice a great increase in the number of solutions when more  $\ell$  numbers are taken into account. The structure is the same of panel a and a zero with lower  $\ell$  needs an higher  $n$  to fit into the selected spectral window. This aspect is particularly evident with the lowest (1690) and the highest (1822)  $\ell$  values: in the first case, the  $n = 5$  solution barely enters the spectral window, while in the second case, all  $n > 1$  solutions fall outside of the spectral window.

Indeed, these considerations lead to the problem of defining the  $\ell$  range which produces a faithful representation of the WGM spectrum. Regarding the highest  $\ell$ , the case here presented gives the answer: the highest  $\ell$  is the one producing only the  $n = 1$  solution in the spectral window; increasing  $\ell$  beyond this value would be useless since the solutions will fall outside the spectral window. Regarding the lowest  $\ell$ , the limit is less sharply defined since it is based on the mode profile. As shown in Section 2.4, increasing  $n$  rises the number of nodes in the radial function  $F(kr)$ , but also the percentage of field outside the microbubble walls or, equivalently, its leakiness. After a certain  $n_{\text{lim}}$  value, the mode becomes too leaky to allow light confinement and solutions with  $n > n_{\text{lim}}$  are not physically acceptable. This, in turn, sets the lowest  $\ell$ , which is the one producing a  $n = n_{\text{lim}}$  solution at the beginning of the spectral window. In panel b,  $n_{\text{lim}}$  was arbitrarily set to 5 without taking into account the mode profile in order to have a clear plot. When using the correct  $n_{\text{lim}}$ , plots like this allow to estimate the density of modes for the microbubble resonator. Using panel b as an example, one has 241 solutions in

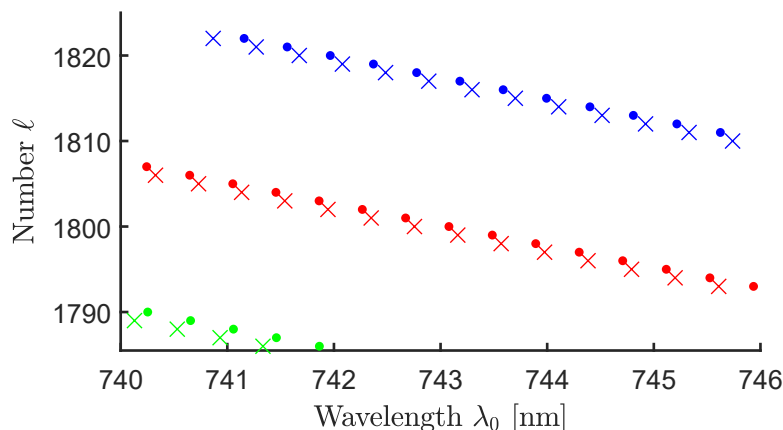


Figure 2.3: Comparison of TE solutions (dots) and TM solutions (crosses), using the color code of Figure 2.2. To visualise the differences between the two solution families, this Figure shows only a fraction of the  $(\lambda_0, \ell)$  plane shown in Figure 2.2b.

a 20 nm range, producing a density of modes equal to  $12 \text{ nm}^{-1}$  without accounting for mode degeneracy.

Up to this point, the discussion focused on the solutions of the TE characteristic equation, but these same conclusions are also valid for the TM solutions. Figure 2.3 highlights this parallelism by plotting the TM solutions (crosses) together with the TE solutions (dots), keeping the same color code used for Figure 2.2. Just as TE solutions, TM solutions increase in frequency with increasing  $n$  and  $\ell$ , and the two solution families are close. In Figure 2.3 the different positions of the two solution families are shown by plotting a fraction of the  $(\lambda_0, \ell)$  plane (cfr. Figure 2.2b). In terms of wavelength difference, one can notice that TE and TM solutions having the same  $(n, \ell)$  values are separated by a little less than one FSR for  $n = 1$  and  $n = 2$  (0.30 nm and 0.33 nm, respectively) and a little more than one FSR for  $n = 3$  (0.55 nm).

A final note regarding the structure of the  $\lambda_0^{(n, \ell)}$  solutions is its analogy with the particle-in-a-box problem in quantum mechanics [27]. In this analogy, the number  $\ell$  represents the angular momentum of the particle, the number  $n$  represents the principal quantum number, the refractive indexes are the heights of the potential barriers and the radii are their widths. Indeed, in this analogy the particle in the box is the photon and the WGMs become bound states for the photon.

Ending this Section, it is important to discuss the indexes needed to uniquely identify a WGM and how they relate with the  $(n, \ell)$  couple discussed so far. Indeed the  $(n, \ell)$  couple fixes the value of the resonance wavelength  $\lambda_0^{(n, \ell)}$ , but this is not enough to identify the geometry of the mode. To do so, recalling Eq. (A.21), it is necessary to add the number  $m$  to the list, ending with the triplet  $(n, \ell, m)$ . Since  $m$  does not appear in the characteristic equations (A.49) and (A.51), modes differing only for the  $m$  number share the same resonance wavelength  $\lambda_0^{(n, \ell)}$  and, in analogy with quantum mechanics, are

said to be degenerate. This degeneracy is important for the computation of the density of modes since it can strongly increase the final result. To a first approximation, in fact, one could assume to count each  $\lambda_0^{(n,\ell)}$  solution  $2\ell + 1$  times to consider all possible  $m$  values (roughly 3500 times for the case shown in Figure 2.2). However, as shown in Subsection 2.5, this approach overestimates severely the  $m$  degeneracy, since it does not take into account how the  $m$  value influences the mode geometry and the coupling with a waveguide. In particular, several  $m$  lead to WGMs that cannot be efficiently excited, therefore leading to an effective  $m$  degeneracy of a few units, rather than a few thousands.

## 2.4 Energy density

The energy density profile of a Whispering Gallery mode is a key element for the computation of the mode volume and allows to visualise clearly the field distribution. For these reasons, this Section focuses on working out this quantity, starting from the results of the previous Sections. In particular, it is assumed that the  $(n, \ell)$  couple and the resonance wavelength  $\lambda_0^{(n,\ell)}$  are already known from the solution of the characteristic equation. The third number  $m$ , instead, is assigned within the allowed range  $[-\ell, \ell]$  to completely identify the mode under study. Different possibilities for  $m$  are considered within this Section to show how this number dictates the geometrical properties of the WGM.

The total energy density  $u$  is formally defined as the sum of the electric energy density  $u_{\text{ele}}$  and the magnetic energy density  $u_{\text{mag}}$ . Both of these densities are deduced from the real fields  $\mathbf{E}$ ,  $\mathbf{D}$ ,  $\mathbf{H}$ ,  $\mathbf{B}$  through the equations

$$\begin{cases} u = u_{\text{ele}} + u_{\text{mag}} \\ u_{\text{ele}} = \frac{1}{2} \mathbf{E} \cdot \mathbf{D} = \frac{1}{2} \epsilon_0 \epsilon_r \mathbf{E}^2 \\ u_{\text{mag}} = \frac{1}{2} \mathbf{H} \cdot \mathbf{B} = \frac{1}{2} \mu_0 \mathbf{H}^2 \end{cases} ,$$

where Eq. (A.2) and Eq. (A.3) are used to obtain expressions featuring only  $\mathbf{E}$  and  $\mathbf{H}$ . For lossless materials, the two densities are equal ( $u_{\text{ele}} = u_{\text{mag}}$ , [123] for a detailed derivation starting from Maxwell's equations) and therefore the total density can be equivalently stated as  $u = 2u_{\text{ele}}$  or  $u = 2u_{\text{mag}}$ . Since the materials making up the MBR sectors are assumed to be lossless (cf. Section 2.1), these alternative forms for the density  $u$  are valid and lead to

$$\begin{cases} u = 2u_{\text{ele}} = \frac{1}{2} \epsilon_0 \epsilon_r \mathcal{E}(\mathbf{r}) \cdot \mathcal{E}^*(\mathbf{r}) \end{cases} \quad (2.7)$$

$$\begin{cases} u = 2u_{\text{mag}} = \frac{1}{2} \mu_0 \mathcal{H}(\mathbf{r}) \cdot \mathcal{H}^*(\mathbf{r}) \end{cases} , \quad (2.8)$$

where the complex fields  $\mathcal{E}$  and  $\mathcal{H}$  are inserted through Eq. (A.6) and the terms oscillating at the frequency  $2\nu$  are neglected, since they average to zero on any time scale of

interest for this work. Both forms are useful because they allow to exploit the formal similarity between the  $\mathcal{E}$  field in the TE case and the  $\mathcal{H}$  field in the TM case. In fact, by combining Eq. (2.7) with Eq. (2.2) and Eq. (2.8) with Eq. (2.5), one obtains

$$\begin{cases} \text{(TE case)} & u = \frac{\epsilon_0}{2} n^2 |F(kr)|^2 |\mathbf{X}_{\ell,m}(\theta, \phi)|^2 \\ \text{(TM case)} & u = \frac{1}{2\mu_0 c^2} n^2 |F(kr)|^2 |\mathbf{X}_{\ell,m}(\theta, \phi)|^2 \end{cases} \quad (2.9)$$

$$\quad (2.10)$$

which differ only by a multiplicative constant. In both functions the radial and the angular dependencies are factorised and can be analysed separately. In particular, Subsection 2.4.1 develops in detail the analytical expression of  $|\mathbf{X}_{\ell,m}(\theta, \phi)|^2$ , while Subsection 2.4.2 develops a method to compute  $F(kr)$ .

### 2.4.1 Angular function $\mathbf{G}$

To deduce the angular dependency of the energy density it is necessary to explicitly write the term  $|\mathbf{X}_{\ell,m}(\theta, \phi)|^2$  appearing in Equations (2.9) and (2.10). Since  $\mathbf{X}_{\ell,m}(\theta, \phi)$  is defined through the derivatives of the spherical harmonic  $Y_{\ell,m}(\theta, \phi)$  (cf. Eq. (A.22)), it is useful to express  $Y_{\ell,m}(\theta, \phi)$  through the Legendre polynomial  $P_{\ell,m}(\cos \theta)$ :

$$Y_{\ell,m}(\theta, \phi) = \sqrt{\frac{(2\ell+1)(\ell-m)!}{4\pi(\ell+m)!}} P_{\ell,m}(\cos \theta) e^{im\phi} \quad (2.11)$$

Using this expression, one obtains the following form for  $|\mathbf{X}_{\ell,m}(\theta, \phi)|^2$ :

$$|\mathbf{X}_{\ell,m}(\theta, \phi)|^2 = \frac{(2\ell+1)(\ell+m)!}{4\pi(\ell-m)!} \left[ \frac{m^2}{\sin^2 \theta} P_{\ell,m}^2(\cos \theta) + \sin^2 \theta (P'_{\ell,m}(\cos \theta))^2 \right] \quad (2.12)$$

To avoid the numerical computation of the derivative,  $P'_{\ell,m}(\cos \theta)$  is written through the difference of two Legendre polynomials:

$$P'_{\ell,m}(\eta) = \frac{1}{1-\eta^2} [P_{\ell,m}(\eta) - (\ell-m+1)P_{\ell+1,m}(\eta)] \quad (\eta = \cos \theta) \quad .$$

Then, all Legendre polynomials are substituted by the Schmidt seminormalized associated Legendre functions  $S_{\ell,m}(\eta)$  through

$$P_{\ell,m}(\eta) = \begin{cases} S_{\ell,m}(\eta) & m = 0 \\ (-1)^m \sqrt{\frac{(\ell+m)!}{2(\ell-m)!}} S_{\ell,m}(\eta) & m \neq 0 \end{cases}$$

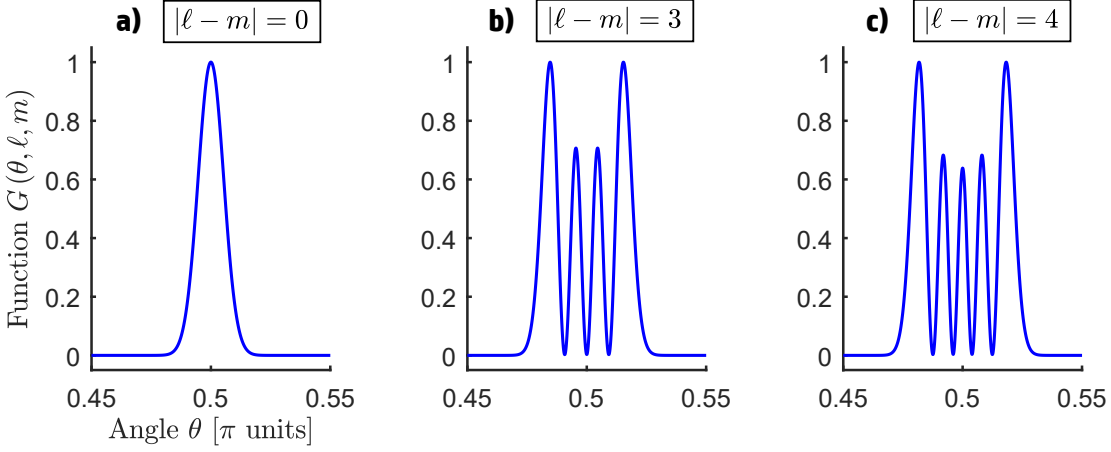


Figure 2.4: Angular functions  $G(\theta, \ell, m)$  for  $\ell = 1790$  and  $m = \{1790, 1787, 1786\}$ , giving the difference  $|\ell - m| = \{0, 3, 4\}$  for panel a, b and c, respectively. The axis labels are the same for the three panels and are omitted in the second and third panel for compactness. Each profile is normalized to its maximum.

to avoid the saturation of the floating point variables when computing high order Legendre polynomials. In the end,  $|\mathbf{X}_{\ell,m}(\theta, \phi)|^2$  is written as

$$|\mathbf{X}_{\ell,m}(\theta, \phi)|^2 = \frac{N_{\ell,m}}{\sin^2\theta} \left\{ (m^2 + 1) S_{\ell,m}^2(\cos\theta) + [(\ell + 1)^2 - m^2] S_{\ell+1,m}^2(\cos\theta) + \right. \\ \left. - 2\sqrt{(\ell + 1)^2 - m^2} S_{\ell,m}(\cos\theta) S_{\ell+1,m}(\cos\theta) \right\} \equiv G(\theta, \ell, m) \quad (2.13)$$

$$\text{with } N_{\ell,m=0} = \frac{2\ell + 1}{4\pi} \quad \text{and} \quad N_{\ell,m \neq 0} = \frac{2\ell + 1}{8\pi}$$

and where the compact notation  $G(\theta, \ell, m)$  is introduced to better handle this long expression and highlight the dependencies.

In particular, regarding this last point, the absence of  $\phi$  in Eq. (2.13) leads to rotational symmetry around the z axis or, equivalently, invariance when moving along the equator or any other parallel. The presence of  $\theta$ , instead, means that the mode is not invariant when moving along a meridian and that the function  $G(\theta, \ell, m)$  is the angular distribution of the mode. The distribution is fixed by the Schmidt seminormalized functions appearing in Eq. (2.13), which in turn are fixed by the  $(\ell, m)$  combination. Finally, the absence of  $\lambda_0$  means that modes with the same  $(\ell, m)$  combination have the same angular distribution, regardless of the  $n$  number and also regardless of the belonging to the TE or TM family.

In Figure 2.4 the function  $G(\theta, \ell, m)$  is plotted for  $\ell = 1790$  and a series of  $m$  values giving the following  $|\ell - m|$  differences:  $|\ell - m| = 0$  for panel a,  $|\ell - m| = 3$  for panel b and  $|\ell - m| = 4$  for panel c. In panel a, the function has a bell-shaped profile centred at  $\theta = \pi/2 = 90^\circ$  with a full-width half-maximum (FWHM) of  $0.012\pi = 2.3^\circ$ . In panel b and c, instead, the function has a comb-like profile, with two primary peaks at the

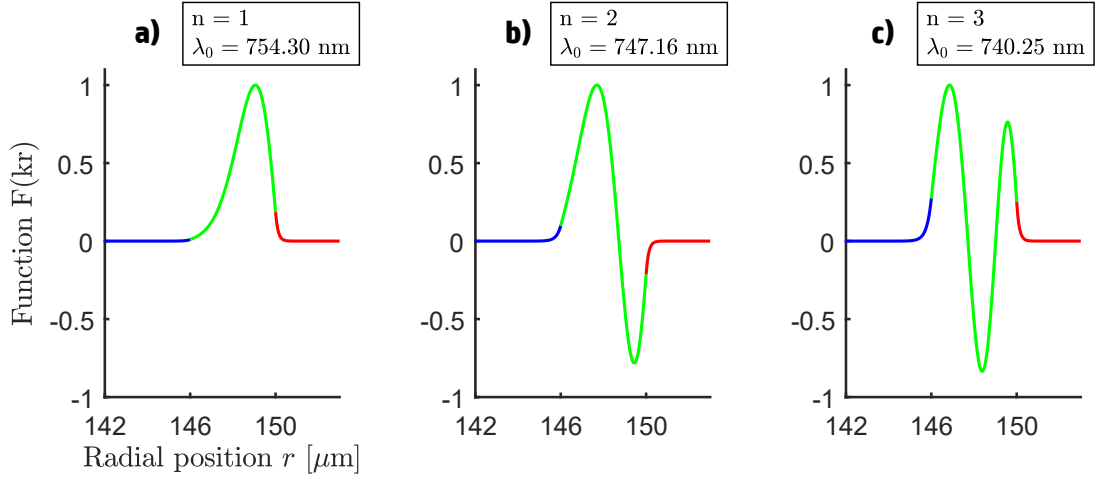


Figure 2.5: Radial functions  $F(kr)$  associated with the  $\ell = 1790$  TE solutions shown in Figure 2.2a. The profiles are deduced applying the methods discussed in Section A.3 and are normalized to their maximum. The axis labels are the same for the three panels and are omitted in the second and third panel for compactness. The color code specifies the sector over which the function  $F(kr)$  extends: blue for the core sector, green for the walls sector and red for the external sector.

extrema ( $\text{FWHM} = 7.2 \cdot 10^{-3}\pi = 1.3^\circ$ ) and a series of secondary peaks between them ( $\text{FWHM} = 4.6 \cdot 10^{-3}\pi = 0.82^\circ$ ). The number of nodes in the central region is equal to  $|\ell - m|$ , while the number of secondary peaks is  $|\ell - m| - 1$ . In other words, Figure 2.4 shows that, as  $|\ell - m|$  increases, the angular distribution  $G(\theta, \ell, m)$  moves away more and more from the equator ( $\theta = \pi/2 = 90^\circ$ ), with primary peaks occupying other parallels and secondary peaks occupying equator zone. As discussed in Subsection 2.4, these features are directly translated to the energy density distribution.

### 2.4.2 Radial function F

Moving to the radial dependency of Equations (2.9) and (2.10), the computation of the function  $F(kr)$  has to be performed. To do so, it is necessary to restart from the four amplitudes defining  $F(kr)$  (cfr. Equation (A.34)) and use the relationships imposed by the boundary conditions to work out an analytical expression for them (cfr. Equations (A.47) and (A.50)). In both the TE case and the TM case, the characteristic equation imposes a null determinant and therefore it is possible to write three amplitudes as function of the fourth, which remains a free parameter and becomes an overall scaling factor. The details of this calculation are reported in Subsection A.3 and, in particular, general expressions for the TE and TM amplitudes are worked out. It is in fact important to highlight that each  $\lambda_0^{(n, \ell)}$  solution has its own set of amplitudes, which, in turn, define its own radial function. In the following a series of  $F(kr)$  functions are commented to highlight their features.

Figure 2.5 shows the radial functions  $F(kr)$  obtained with the methods of Section



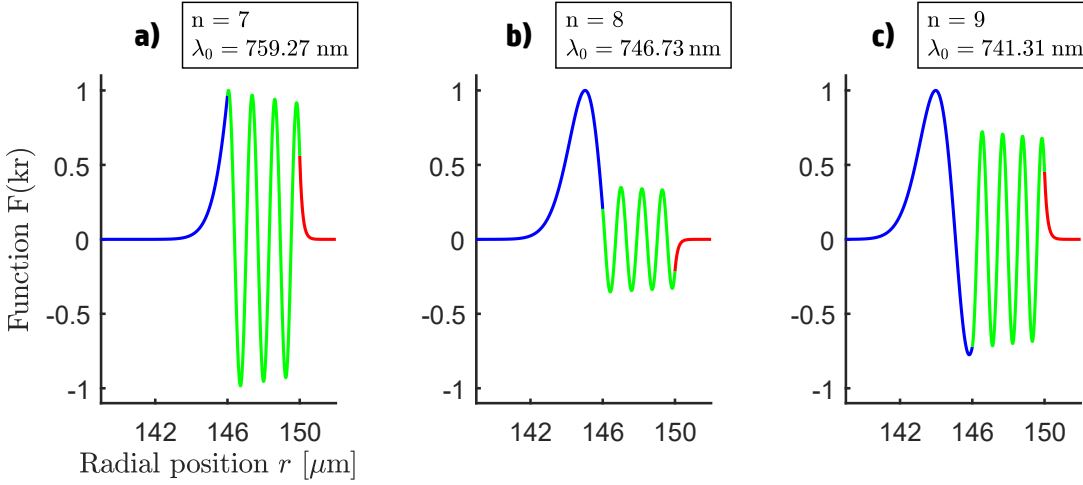


Figure 2.6: Radial functions  $F(kr)$  of TE modes with  $\ell = 1613$  falling in the  $[740 \text{ nm}, 760 \text{ nm}]$  spectral window used for Figure 2.2b. The profiles show the transition from wall modes (panel a) to core modes (panel b and c) due to the increase in  $n$ . This Figure adopts the same color code and the same conventions of Figure 2.5.

A.3 for the TE  $\ell = 1790$  modes appearing in Figure 2.2a: in particular, panel a shows  $F(kr)$  for the  $n = 1$  solution, panel b for the  $n = 2$  solution and panel c for the  $n = 3$  solution. In each panel  $F(kr)$  is normalized to its maximum and the color code specifies the sector over which the function extends: blue for the core, green for the walls and red for the external medium. As anticipated in Section 2.3, each  $n$  increment produces a new node in  $F(kr)$  and, in the end,  $n$  is equal to the number of nodes incremented by 1 ( $\# \text{ nodes} + 1$ ). In addition, an increase in  $n$  shifts the maximum of the  $F(kr)$  function towards the center of the microbubble (positions of maxima:  $149.05 \mu\text{m}$ ,  $147.69 \mu\text{m}$ ,  $146.82 \mu\text{m}$ ), and therefore away from the microbubble surface (at  $R_e = 150 \mu\text{m}$ ).

Due to the higher index of the microbubble walls ( $n_w = 1.45$  vs.  $n_c = 1.33$  and  $n_e = 1$ ), the mode is confined in the walls sector and only evanescent tails are present in both the core and the external sectors. Even if these evanescent tails represent a tiny fraction of the field distribution, both have important roles for the microbubble applicability. The external tail, in fact, can couple the WGM to a waveguide mode, allowing light injection and extraction [24]. The core tail, instead, allows to sense particles in proximity or in contact with the internal wall, enabling the implementation of the microbubble as an optical sensor [125, 25].

Finally, Figure 2.6 shows the radial function  $F(kr)$  for a set of TE modes in the  $[740 \text{ nm}, 760 \text{ nm}]$  window (cfr. Figure 2.2) having a low  $\ell$  number and an high  $n$  number. In particular, the three profiles have  $\ell = 1613$  and  $n = \{7, 8, 9\}$  for panel a, b and c, respectively. The three plots, which follow the same conventions of Figure 2.5, highlight the transition from WGMs totally confined in the microbubble walls (“wall modes”, panel a) to WGMs having their maxima in the core sector (“core modes”, panel b and c). This shift, which is a consequence of the  $n$  increase, is particularly interesting for

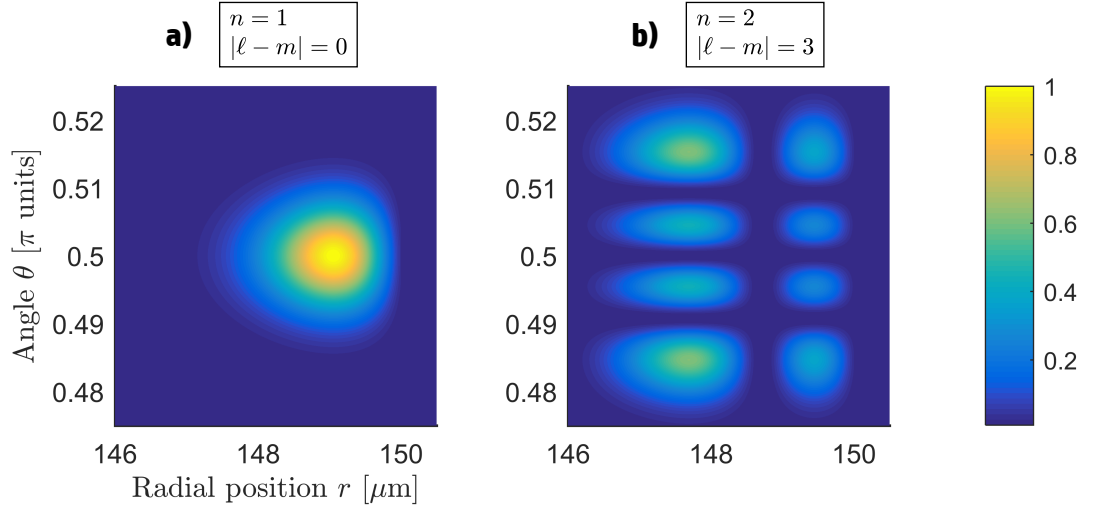


Figure 2.7: Normalized energy density  $u_{\text{norm}}$  for the fundamental WGM ( $n = 1$ ,  $\ell = 1790$ ,  $m = 1790$ ) (panel a) and for the non-fundamental WGM ( $n = 2$ ,  $\ell = 1790$ ,  $m = 1787$ ) (panel b). The two plots have the same axis labels and follow the same color scale, reported on the right side of the Figure.

sensing the microbubble contents, since it significantly increases the percentage of field in the core with respect to the low  $n$  cases, which only have the evanescent tails (cfr. Figure 2.5). Core modes are also fundamental to couple the microbubble WGMs to quantum emitters, as discussed in Chapter 5.

### 2.4.3 Energy density distribution

Now that the radial function  $F(kr)$  and the angular function  $G(\theta, \ell, m)$  are known from the Subsections 2.4.2 and 2.4.1, the energy density  $u$  can be computed directly using Equations (2.9) and (2.10). In particular, a 2D plot of  $u$  in the  $(\theta, r)$  coordinate plane can be obtained, allowing to clearly visualise the mode distribution. However, for better comparison and visualisation, in this Subsection the normalised energy density  $u_{\text{norm}}$  defined as

$$u_{\text{norm}} = \frac{G(\theta, \ell, m)}{\max_{0 \leq \theta \leq \pi} \{G(\theta, \ell, m)\}} \frac{n^2 |F(kr)|^2}{\max_{0 \leq r < \infty} \{n^2 |F(kr)|^2\}} \quad (2.14)$$

is plotted in the various panels.

Figure 2.7 shows  $u_{\text{norm}}$  for two TE Whispering Gallery modes: the one associated with the triplet ( $n = 1$ ,  $\ell = 1790$ ,  $m = 1790$ ) in panel a and the one associated with ( $n = 2$ ,  $\ell = 1790$ ,  $m = 1787$ ) in panel b. The 2D distribution of the modes reflect the angular and radial behaviour discussed in the previous Subsections, with the number  $n$  and the difference  $|\ell - m|$  dictating the number of nodes in  $u_{\text{norm}}$  along the  $r$  direction and the  $\theta$  direction, respectively. In particular, the distribution in panel a arises from

the combination of the profiles shown in Figure 2.4a and 2.5a, while the distribution in panel b arises from those shown in Figure 2.4b and 2.5b.

The WGM of panel a is defined a *fundamental WGM* since it arises from the combination of a  $n = 1$  radial function and a  $|\ell - m| = 0$  angular function. As a consequence of this definition, the fundamental WGM has no nodes along the  $r$  direction nor the  $\theta$  direction, and therefore is concentrated in just one lobe. Also, since no condition is posed on  $\ell$ , many fundamental modes are possible: each associated with a different  $\ell$  value (e.g. panel a shows the  $\ell = 1790$  fundamental mode). For these modes the interpretation of a WGM as a ring of light running along the microbubble equator is particularly fitting, due to the single-lobe concentration and the  $\phi$  symmetry discussed in Subsection 2.4.1.

The mode in panel b, instead, arises from the combination of a  $n = 2$  radial function and a  $|\ell - m| = 3$  angular function, therefore having a single radial node and three angular nodes. As a consequence, this mode cannot be classified as fundamental and is made up of numerous lobes. By comparing this mode with the fundamental one, one notices that the distribution in several lobes lowers the maximum (0.61 vs. 1.0) and the maximum position is shifted inwards (147.7  $\mu\text{m}$  vs. 149.1  $\mu\text{m}$ ). Indeed, in this case, the idea of a ring of light is less fitting, since the mode is distributed among different parallels and different radial shells due to the angular nodes and the radial nodes respectively.

As discussed in Section 2.5 and Section 2.6, the geometrical features of the energy density distribution here discussed are key elements dictating the coupling between the WGMs and a waveguide as well as the volume of the WGMs themselves.

## 2.5 Waveguide coupling

This Section focuses on using the energy density distribution obtained in Subsection 2.4 to estimate the coupling between a microbubble WGM and a waveguide. This parameter, in fact, is of great interest in designing an experiment, since it allows to predict the WGMs that can be efficiently excited and brought into a critical coupling regime. In particular, the computation here presented is an initial step towards a full computation implementing the complex field distribution of both the WGM and the waveguide.

To simulate the tapered fibers used in the experiments of Chapter 3 and Chapter 4, the waveguide chosen for this Section is an optical fiber having a silica core ( $n_{\text{core}} = 1.45$ ), an air cladding ( $n_{\text{clad}} = 1$ ) and a 3  $\mu\text{m}$  diameter. Its energy distribution  $u_{\text{fib}}$  is derived following the theory of optical fibers described in [126]. In particular, since the index mismatch is high ( $n_{\text{core}} - n_{\text{clad}} = 0.45$ ), the weakly guiding approximation cannot be made and the complete characteristic equation has to be solved, implementing a numerical method similar to one described in Subsection 2.3. From this resolution, both the energy density distribution  $u_{\text{fib}}$  and the propagation constant  $\beta$  are found, imposing the WGM resonance wavelength  $\lambda_0$  as the guided wavelength of the fiber.

In terms of positioning, the fiber is placed in the MBR equatorial plane and in contact with the MBR walls, as shown in panel a of Figure 2.8. In analogy with Figure 2.1, this sketch shows a sagittal cut of both the MBR and the fiber, while using a a

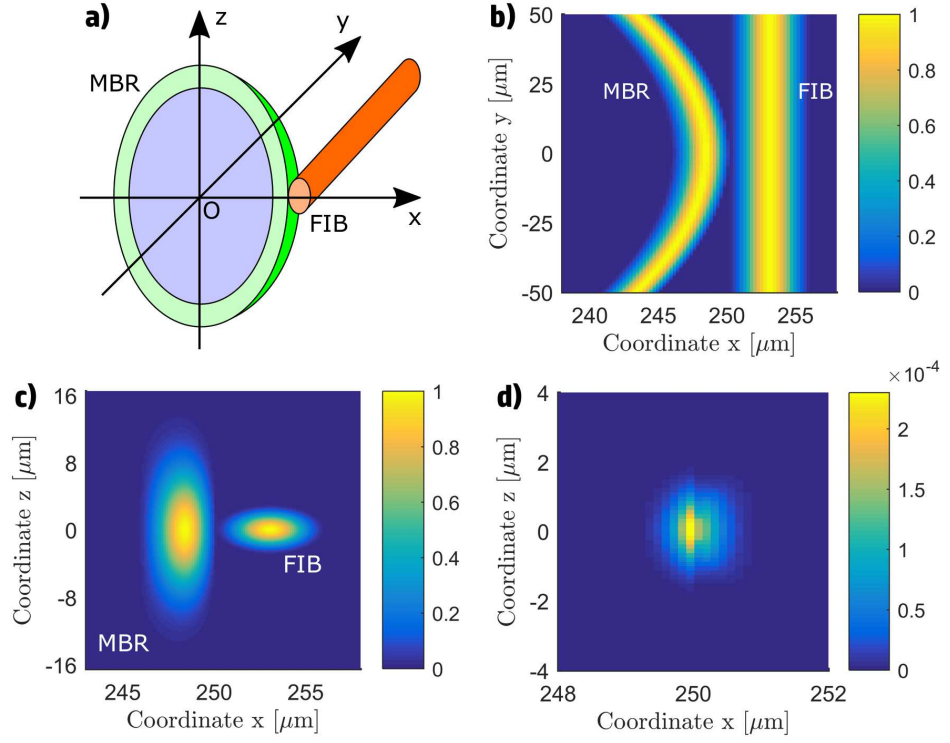


Figure 2.8: Panel a shows a sagittal cut of the MBR and the fiber to describe their relative positioning. Panel b and c support this sketch by showing the energy density distributions of both the microbubble WGM and the fiber mode, in the  $xy$  and  $xz$  plane respectively. Panel d shows the overlap of the two distributions, as deduced by the profiles shown in panel c.

3D prospective. This sketch is also aided by panels b and c, which show the WGM energy density  $u_{\text{mbr}}$  and the fiber energy density  $u_{\text{fib}}$  in the  $xy$  plane and the  $xz$  plane, respectively.

The dielectric structure of the MBR is the same of the previous Sections (i.e. water core, silica walls, air as surrounding medium) and also the walls thickness is kept to 4  $\mu\text{m}$ . Instead, the MBR external radius and the wavelength range are changed to better represent the experiments in Chapter 3 and Chapter 4. In particular, the MBR external radius  $R_e$  is set to 250  $\mu\text{m}$ , while the MBR spectrum is reconstructed around 1550 nm. The WGM selected for the computations of this Section is the fundamental one ( $n = 1$  and  $m = \ell$ ) and has a resonance wavelength  $\lambda_0 = 1549.824$  nm ( $\ell = 1448$ ). Its energy density  $u_{\text{mbr}}$  is deduced as in Section 2.4 and, as previously mentioned, it is shown in panel b and c of Figure 2.8 in both the  $xy$  and the  $xz$  planes.

The coupling  $\kappa$  between the MBR mode and the fiber mode is rigorously computed through coupled mode theory [127, 128] by performing an overlap integral between the two field distribution in the transversal plane  $xz$  and then an integration along the fiber

propagation direction  $y$ . In formulas, this is

$$\kappa_{\text{plane}}(y) = \frac{k_0^2}{2\beta} \int (n_{\text{mbr}}^2 - n_{\text{fib}}^2) \mathcal{E}_{\text{mbr}}(x, y, z) \mathcal{E}_{\text{fib}}^*(x, y, z) dx dz \quad (2.15)$$

$$\kappa = \int \kappa_{\text{plane}}(y) dy \quad (2.16)$$

where  $\mathcal{E}_{\text{mbr}}$  and  $\mathcal{E}_{\text{fib}}$  are the complex field distribution of the two modes. Here, however, a simplified approach is adopted to reduce the complexity of the calculation and introduce the real-valued energy densities  $u_{\text{mbr}}$  and  $u_{\text{fib}}$ . In particular, Equation (2.15) is modified into

$$\kappa_{\text{plane}}(y) = \frac{k_0^2}{2\beta} (n_w^2 - n_e^2) \frac{\int u_{\text{mbr}}(x, y, z) u_{\text{fib}}(x, y, z) dx dz}{\sqrt{\int u_{\text{mbr}}^2(x, y, z) dx dz} \sqrt{\int u_{\text{fib}}^2(x, y, z) dx dz}} \quad (2.17)$$

where the integrals at the denominator are inserted for normalization purposes and the index difference is simply  $n_w^2 - n_e^2$  since the MBR walls and the fiber are both made of silica and their surrounding environment is air. An important approximation introduced with this modification is the absence of a phase interference term, which is instead naturally present in Equation (2.15) through the use of the complex fields. As a consequence, this introduces a certain overestimation of  $\kappa_{\text{plane}}$ , since it implicitly assumes a perfect phase match between the modes.

As example, panel d of Figure 2.8 shows the overlap function  $u_{\text{mbr}} u_{\text{fib}}$  produced by the distributions shown in panel c. Since the two distributions superpose through their evanescent tails, the product  $u_{\text{mbr}} u_{\text{fib}}$  is orders of magnitude below the typical values of both  $u_{\text{mbr}}$  and  $u_{\text{fib}}$ , as shown by the different colormaps.

By a numerical integration of the distributions shown in panel c and panel d of Figure 2.8, it is possible to evaluate the integrals appearing in Equation (2.17) and obtain the value of  $\kappa_{\text{plane}}$  for the plane  $y = 0$ . Then, by shifting the integration plane along the  $y$  direction and repeating the numerical integration, it is possible to reconstruct the  $\kappa_{\text{plane}}$  function. For the fundamental WGM mode here considered, the  $\kappa_{\text{plane}}$  function is shown as a blue curve in Figure 2.9 and features a decreasing value for increasing  $y$ . This trend is explained with the curvature of the MBR, which reduces the spatial superposition of the two modes for increasing  $y$  (cfr. panel b of Figure 2.8), and shows that the coupling region extends up to 15  $\mu\text{m}$ . Due to the symmetry of the configuration, the function  $\kappa_{\text{plane}}$  is evaluated only for positive  $y$ , with the negative- $y$  side taking the same values of the positive- $y$  side.

Taking into account the function symmetry for the final integration of Equation (2.16), the overall coupling coefficient  $\kappa$  for the fundamental WGM is  $\kappa = 5.72 \cdot 10^{-4}$  and its square, which is the quantity dictating the efficiency of the WGM excitation, is  $|\kappa|^2 = 3.28 \cdot 10^{-7}$ . This value is comparable with the ones found experimentally through a cavity ring down analysis (cfr. Subsection 1.2 and [54, 55]) and shows that the presented approach is a good starting point for a complete complex-field computation.

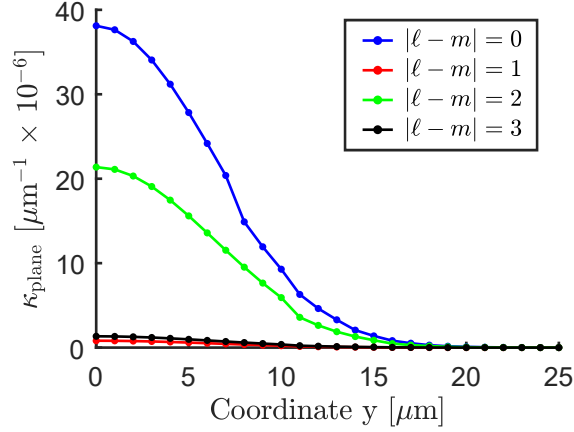


Figure 2.9: Function  $\kappa_{\text{plane}}$  resulting from Equation (2.17) for a series of WGMs differing in their  $m$  number. The dots represent the computed values, while the connecting lines are an aid to visualise the trend.

In particular, assuming a critical coupling regime (i.e intrinsic losses equal to coupling losses) the  $|\kappa|^2$  here computed leads to a resonance quality factor  $Q = 7.0 \cdot 10^9$ , which has the order of magnitude of the ones experimentally (cfr. Subsection 1.2 and [54, 55]).

Finally, the entire calculation is repeated for non-fundamental WGMs having  $|\ell - m| = \{1, 2, 3, 4\}$  to highlight the importance of the mode distribution along the polar direction. In particular, Figure 2.9 shows that the coupling is maximum in the  $|\ell - m| = 0$  case, it is reduced for the  $|\ell - m| = \{2, 4\}$  case and almost null for  $|\ell - m| = \{1, 3\}$ . This behaviour is a consequence of the angular function properties discussed in Subsection 2.4.1 and, in particular, of the increase of nodes in the equatorial plane for increasing  $|\ell - m|$  difference. In practice, as shown in Figure 2.4, odd  $|\ell - m|$  values produce a node in the equatorial plane and this severely reduce the value of the overlap integral in Equation (2.17). For an even  $|\ell - m|$ , instead, secondary peaks are present in the equatorial plane, lowering the overlap but not completely cancelling it. As a consequence, the value of  $|\kappa|^2$  computed from the integration in Equation (2.16) is affected, since  $|\kappa|^2 = \{1.56 \cdot 10^{-10}, 4.22 \cdot 10^{-10}\}$  for  $|\ell - m| = \{1, 3\}$  and  $|\kappa|^2 = \{1.07 \cdot 10^{-7}, 6.78 \cdot 10^{-8}\}$  for  $|\ell - m| = \{2, 4\}$ .

In the end, the coupling dependency on the  $m$  number limits the modes that can be efficiently coupled and therefore produces a reduction of the initial  $2\ell + 1$  mode degeneracy discussed in Section 2.3. In particular, the results of this Section show an effective degeneracy in the order of units, rather than thousands ( $2\ell + 1 = 2897$ ), which strongly influences the computation of the density of modes in a specific wavelength range (cfr. end of Section 2.3). Finally, it is important to highlight that the effective degeneracy here discussed ultimately depends on the waveguide field distribution and therefore strongly depends on the adopted experimental configuration.

## 2.6 Modal volume

From the results of Section 2.4, it is finally possible to compute the volume of the Whispering Gallery mode. As in Section 2.4, it is assumed that  $n$ ,  $\ell$  and  $\lambda_0^{(n,\ell)}$  are already known from the solution of the characteristic equation, while  $m$  is an assigned value in the  $[-\ell, \ell]$  range. Even in this case, different  $m$  values are considered to highlight the volume dependency on this number.

The volume  $\mathcal{V}$  of a WGM is defined in terms of its energy density as follows:

$$\mathcal{V} = \frac{\int u(r, \theta, \phi) dV}{\max_{(0 \leq r < \infty, 0 \leq \theta \leq \pi, 0 \leq \phi \leq 2\pi)} \{u(r, \theta, \phi)\}} \quad , \quad (2.18)$$

where the integral on the energy density  $u$  extends over the entire space. By inserting in this expression Eq. (2.9), or equivalently Eq. (2.10), one obtains

$$\mathcal{V} = \frac{\int_0^\infty n^2 |F(kr)|^2 r^2 dr \int |\mathbf{X}_{\ell,m}(\theta, \phi)|^2 d\Omega}{\max_{0 \leq r < \infty} \left\{ n^2 |F(kr)|^2 \right\} \max_{(0 \leq \theta \leq \pi, 0 \leq \phi \leq 2\pi)} \left\{ |\mathbf{X}_{\ell,m}(\theta, \phi)|^2 \right\}} \quad , \quad (2.19)$$

where the integral on  $|\mathbf{X}_{\ell,m}(\theta, \phi)|^2$  extends over the entire solid angle. This expression is the same for both TE and TM modes due to the analogy between Eq. (2.9) and Eq. (2.10) discussed in Section 2.4.

Equation 2.19 can be simplified taking into account the properties of  $\mathbf{X}_{\ell,m}(\theta, \phi)$ . First of all, the angular integral in the numerator is known and given by [129]

$$\int |\mathbf{X}_{\ell,m}(\theta, \phi)|^2 d\Omega = \ell(\ell + 1) \quad .$$

Then, recalling Eq. (2.13), one has  $|\mathbf{X}_{\ell,m}(\theta, \phi)|^2 = G(\theta, \ell, m)$  and therefore the computation of the maximum in the denominator becomes

$$\max_{(0 \leq \theta \leq \pi, 0 \leq \phi \leq 2\pi)} \left\{ |\mathbf{X}_{\ell,m}(\theta, \phi)|^2 \right\} = \max_{0 \leq \theta \leq \pi} \{G(\theta, \ell, m)\} \quad .$$

Finally, Equation (2.19) becomes

$$\mathcal{V} = \frac{\ell(\ell + 1) \int_0^\infty n^2 |F(kr)|^2 r^2 dr}{\max_{0 \leq r < \infty} \left\{ n^2 |F(kr)|^2 \right\} \max_{0 \leq \theta \leq \pi} \{G(\theta, \ell, m)\}} \quad . \quad (2.20)$$

Since the functions  $F(kr)$  and  $G(\theta, \ell, m)$  are known from the procedures described in Subsection 2.4.1 and Subsection 2.4.2, one can use numerical methods to evaluate the two maxima in the denominator and the integral at the numerator. These estimates are then inserted into Eq. 2.20 to finally compute the modal volume  $\mathcal{V}$ .

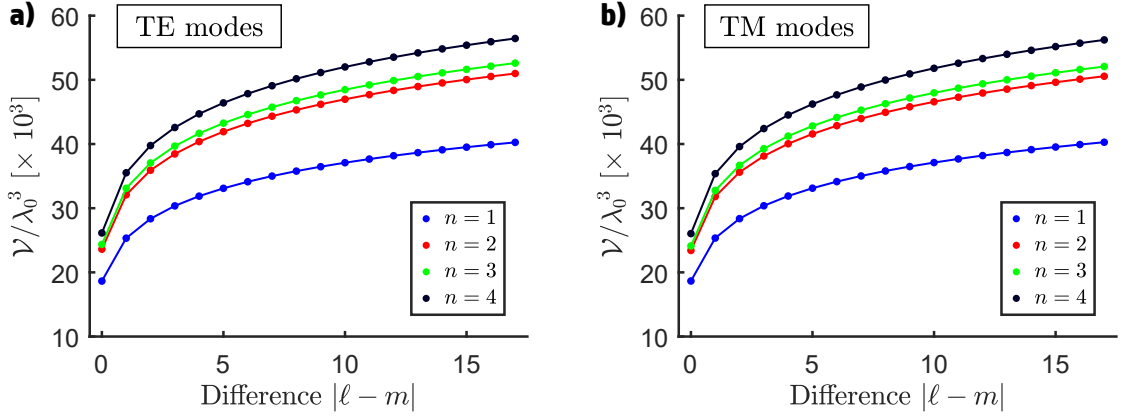


Figure 2.10: Normalized volume  $\mathcal{V}/\lambda_0^3$  for TE modes (panel a) and TM modes (panel b) having  $\ell = 1790$ , with the difference  $|\ell - m|$  and the  $n$  number taking values in the  $[0, 17]$  and  $[1, 4]$  ranges, respectively. The lines connecting the points associated with the same  $n$  values are guides to the eye.

Figure 2.10 shows the volume  $\mathcal{V}$ , normalized to the cube of the resonance wavelength  $\lambda_0^3$ , for a set of TE and TM modes. In analogy with Figure 2.4 and 2.5, the  $\ell$  number is set to 1790, while the difference  $|\ell - m|$  and the  $n$  number take values in the  $[0, 17]$  and  $[1, 4]$  ranges, respectively. Since the modal volume increases with increasing  $|\ell - m|$  and with increasing  $n$ , the fundamental mode ( $|\ell - m| = 0$ ,  $n = 1$ ) has minimal volume and therefore is the most promising for coupling with quantum emitters (see Chapter 5). Also, by comparing the two panels, one notices that TE and TM modes have almost identical volumes and the same trends, leading to an equivalence of the two mode families when modal volume is involved.

## 2.7 Conclusions

In this Chapter an analytical theory deriving the WGMs of a microbubble has been presented, extending the microsphere case to the multilayer case and filling a void in literature, where no similar dissertation was found. Using the results of the analytical derivation, a semi-analytical approach allowed to compute a series of quantities of interest, such as the mode profile and its spatial distribution. In particular, the discussion focused on evaluating the coupling between the microbubble WGMs and optical fiber, and on evaluating the WGMs modal volume. The results for the WGM-fiber coupling are within one order from the experimental ones and represent a good starting point for a more detailed theory. The modal volume results, instead, represent a starting point for the discussion of Chapter 5, where the control of single-photon sources through a microbubble mode is studied.

In prospective, the theory here presented can be further developed to account for some aspects that in this first iteration were simplified. For example, the material absorption from the dielectrics making up the resonator could be restored to deduce



not only the resonance wavelength the WGMs, but also their linewidth. Then, the coupling of the WGMs with an external waveguide could be revised to use the complex field distribution rather than the energy density distribution and restore in this way the phase matching contributions.

Finally, the theory could be specialised for quantities of interest outside of the context of this thesis work. For example, the Poynting vector could be worked out from the field expressions, allowing to estimate the intensity of the wave circulating in the WGM, and the radial function  $F(kr)$  could be used to compute the WGMs effective indexes. This quantities, in fact, are of interest for the onset of non-linear optical effects and could guide the implementation of a setup aimed at triggering such effects.



## Chapter 3

# Photoacoustic sensing

In this Chapter the detection of a photoacoustic (PA) wave is achieved through the perturbation induced in an microbubble (MBR) optical resonance, effectively demonstrating the implementation of the microbubble as optical photoacoustic transducer.

The Chapter starts with a description of the setup (Section 3.1), which featured the MBR in the double role of optical PA transducer and vial containing the contrast agent. The experimental configuration was designed to run a proof-of-concept experiment (Section 3.2) and then to simulate a flow cytometry experiment (Section 3.3). The first experiment demonstrated the feasibility of the measurement, verified the transducer readings through the characterisation of a known PA agent and allowed to gain insight on the transduction mechanism, which is strongly influenced by the mechanical properties of the MBR. The second experiment, instead, challenged the MBR transducer through the characterisation of a constantly flowing and more diluted PA agent, simulating the configuration of a flow cytometry experiment.

The Chapter retraces and extends the contents of three articles published during the PhD programme [51, 52, 130].

### 3.1 The experimental setup

Panel a of Figure 3.1 shows a sketch of the experimental setup used to demonstrate PA detection through the microbubble resonator. The setup can be conceptually divided into three subsystems: the microfluidic subsystem, used to load the PA contrast agent into the MBR; the pump subsystem, used to excite the contrast agent and trigger the PA emission; and the probe subsystem, used to sense the PA wave through the shift of a WGM resonance.

The microfluidic subsystem comprises the elements on the bottom right corner of this sketch and was aimed at filling the MBR with a solution containing the contrast agent. This was achieved by connecting the MBR to a flexible polymer tubing (Tygon R-3607, Saint-Gobain, La Défense, Courbevoie, France) and then using a peristaltic pump (Minipuls 3, Gilson, Middleton, WI, USA) to draw the solution from its reservoir.

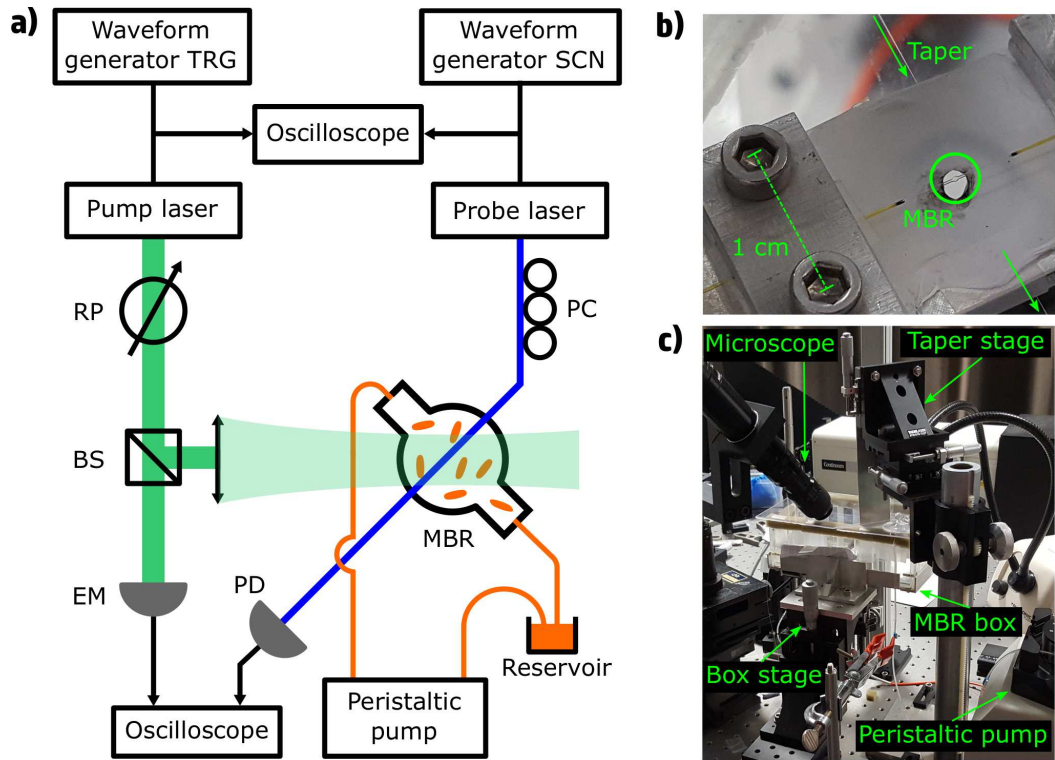


Figure 3.1: Sketch of the experimental setup used to demonstrate PA detection through a microbubble resonator (panel a), along with two pictures showing some of the elements making up the system (panel b and c). In particular, panel b shows the MBR positioned on its holder, while panel c shows the arrangement of the elements on the optical table.

The solution was a water-based colloidal suspension of gold nanorods (GNRs) synthesized by the seed-mediated approach [82, 69], PEGylated and concentrated to 4 mM Au. For this proof-of-concept experiment, GNRs appeared a natural benchmark contrast agent due to their long history and importance in PA applications [72, 71, 74, 69, 70, 73]. To match the emission of the pump laser (1064 nm), the GNRs were synthesized with an elongated aspect ratio, leading to a 70 nm length and a 10 nm diameter. A GNRs concentration of 13 nM was deduced from the particles geometry and the the Au concentration, assuming an FCC (face-centred cubic) structure for the crystal making up each nanorod.

Moving to the MBR, it had a 430  $\mu\text{m}$  diameter, a resulting capacity of 41 nl, and was fabricated with the arc discharge technique [20, 21, 131] (base fused silica capillary: Z-FSS-200280, Postnova Analytics GmbH, Landsberg, Germany). The MBR, mounted on an home-made metallic holder (panel b), was placed inside a glass-floor box (panel c), which shielded the MBR from air currents [132], while still allowing a laser beam to impinge on the MBR. The box was connected to a set of micrometric stages (panel c) in order to place the MBR in the waist of the laser beam exciting the GNRs. This

alignment was performed by acting on the micrometric stages while maximizing the light scattered from the MBR, which was observed through an handheld infrared camera.

The pump subsystem, instead, comprises the elements on the left side of the sketch and was aimed at triggering the PA emission from the GNRs contained in the MBR. The main element of this subsystem was a free-space pulsed Nd:YAG laser (Asclepion Laser Technologies, Jena, Germany) having an emission wavelength of 1064 nm (coinciding with the central wavelength of the GNRs plasmonic band), a pulse duration of 3.3 ns, a pulse energy of 40  $\mu$ J and a repetition rate of 10 Hz: this source is labelled as pump laser in panel a. A square wave provided by an electric waveform generator (Keysight 33210A, Agilent Technologies, Santa Clara, CA, USA; TRG in Figure 3.1a) was used to time the emission of this source and to trigger the acquisition of the oscilloscope (RTO1004, Rohde and Schwarz, Munich, Germany).

The beam produced by the pump laser source passed through a rotatable polariser (RP) and was divided into two branches by a beam splitter (BS). The first branch impinged on a pyroelectric energy meter (QE8SP, Gentec-EO, Quebec, QC, Canada; EM), while the second branch impinged on the MBR after being focused by a converging lens, allowing to expose the MBR uniformly (cfr. Subsection 3.1.1). Since the pulses impinged on the MBR following a vertical line, with a floor-to-ceiling direction, the second branch resembled the configuration of an inverted microscope. The polariser and the energy meter allowed to tune and monitor the fluence exciting the GNRs, which was an important aspect for the measurements, as discussed in Section 3.2 and Section 3.3.

Finally, the probe subsystem comprises the elements on the right side of the sketch and allowed the detection of the PA wave through the MBR. In this subsystem, an home-made tapered fiber [53] was used to couple the MBR with the emission of a CW infrared fiber laser (Koheras ADJUSTICK, NKT Photonics, Birkerød, Denmark; spectral range 1550-1551 nm; probe laser in panel a of Figure 3.1). The taper could be moved finely and put in contact with the MBR equator through a second set of micrometric stages and a long working-distance microscope (custom model, Navitar, Rochester, NY, USA), which are shown in panel c of Figure 3.1. A fiber polarization controller (PC) was used to select the polarisation of light injected into the MBR and the transmission of the coupled system was recorded through an InGaAs photodiode (PDA400, Thorlabs Newton, NJ, USA; bandwidth 10 MHz; PD). A second electric waveform generator (Keysight 33220A, Agilent Technologies, Santa Clara, CA, USA; SCN) was used to finely set the probing wavelength or perform a frequency scan up to 1 GHz (or equivalently a wavelength scan up to 8 pm).

### 3.1.1 Preliminary measurements on the pump laser subsystem

During the preparation of the experimental setup, a series of auxiliary measurements concerning the pump laser subsystem were performed.

First of all, a set of knife edge measurements [133] was performed to check the focusing produced by the converging lens: the results of this procedure are shown in Figure 3.2. Indeed, the chosen lens produced the right level of focusing for the purposes of the experiment, since the beam waist ( $w_0 = 220 \mu\text{m}$ , cfr. panel b) was very close to

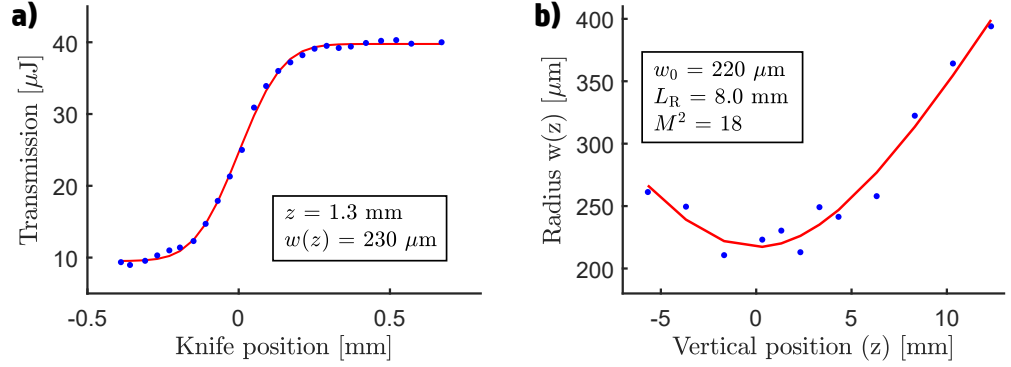


Figure 3.2: S-shaped transmission trend produced by the beam blockage in an knife edge measurement (panel a) along with the beam radius at different heights (panel b). In both panels blue dots represent the experimental data, while the red traces are fitting curves.

the MBR radius (215  $\mu\text{m}$ ). In addition, this level of focusing produced a rather long Rayleigh length ( $L_R = 8.0 \text{ mm}$ ), which made the vertical alignment of the MBR less critical during the preparation of the microfluidic subsystem.

The second set of auxiliary measurements, instead, was aimed at deducing the pump laser fluence at the beam waist from the signals recorded by the energy meter (EM in the sketch shown in panel a of Figure 3.1). To do this, a calibrated sensor was placed in proximity of the beam waist in order to measure the energy of the pump laser pulses. The readings of this calibrated sensor were recorded together with the signals from the energy meter and the procedure was repeated for different pulse energies by acting on the the rotatable polariser (RP). Panel a of Figure 3.3 shows some of the recorded signals as examples. For each EM signal, the average value in the [22  $\mu\text{s}$  - 25  $\mu\text{s}$ ] range was computed to quantify the signal intensity and, since the signals were practically flat in that range, this value is referred to as the plateau value. In panel b the plateau values are plotted against the pulse energies, finding a linear trend to a very good approximation. Starting from an assigned EM signal, the fitting line allowed to deduce the energy of the pulse that triggered the assigned signal. In fact, this could be done by computing the plateau value of the assigned signal and then interpolating the fitting line, finding the associated energy pulse  $E_{\text{pul}}$ . From this energy estimate it was then straightforward to compute the pump laser fluence as  $F = E_{\text{pul}}/A_{\text{spot}}$ , where the spot area  $A_{\text{spot}} = \pi w_0^2 = 0.15 \text{ mm}^2$  was known from the knife edge measurements previously discussed.

Finally, the last set of measurements was aimed at checking the generation of the PA wave from the GNRs hosted in the MBR. For this series of measurements, a test MBR was connected to the microfluidic circuit, placed inside the box on the beam waist and submerged with water, as shown in panel a of Figure 3.4. Then, an ultrasound transducer (Olympus Panametrics, Japan; sensor diameter 0.5 inch, frequency range from 1 to 10 MHz) was positioned so that the MBR was placed in its acoustic focus and the pump laser was enabled. The signal picked up by microphone (blue curve, panel

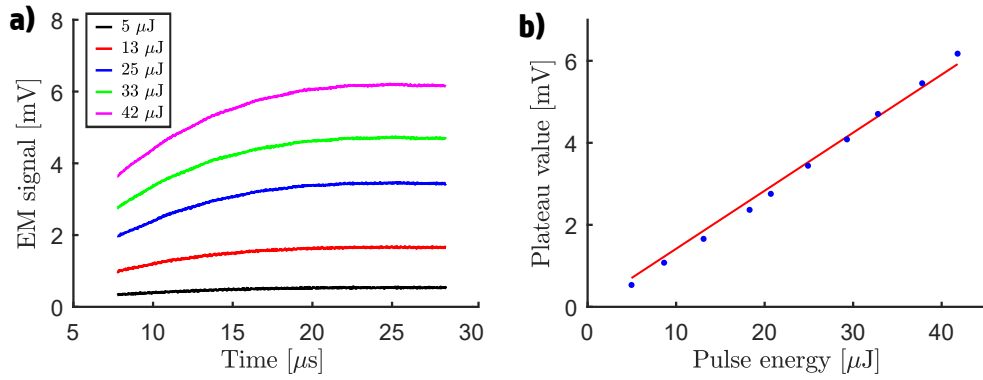


Figure 3.3: Panel a shows the EM signals generated by laser pulses of different energy. In panel b the plateau value computed from these traces is plotted against the pulse energy (blue dots): the line fitting the data is shown in red.

b), was in line with the reference signal (red curve, panel b), which was obtained by positioning an hydrated chitosan film imbued with GNRs, in place of the MBR. This chitosan film was used as a PA phantom in other works [80, 82] and represented a natural benchmark to verify PA emission from GNRs when preparing the setup. In addition, when illuminating the MBR, the microphone was slightly moved from its initial position to reconstruct a 2D map of the PA intensity, obtaining the results shown in panel c. This map confirms the GNRs as the source of the PA wave, since the extension of the high-signal area is compatible with the size of the test MBR (radius 210 μm).

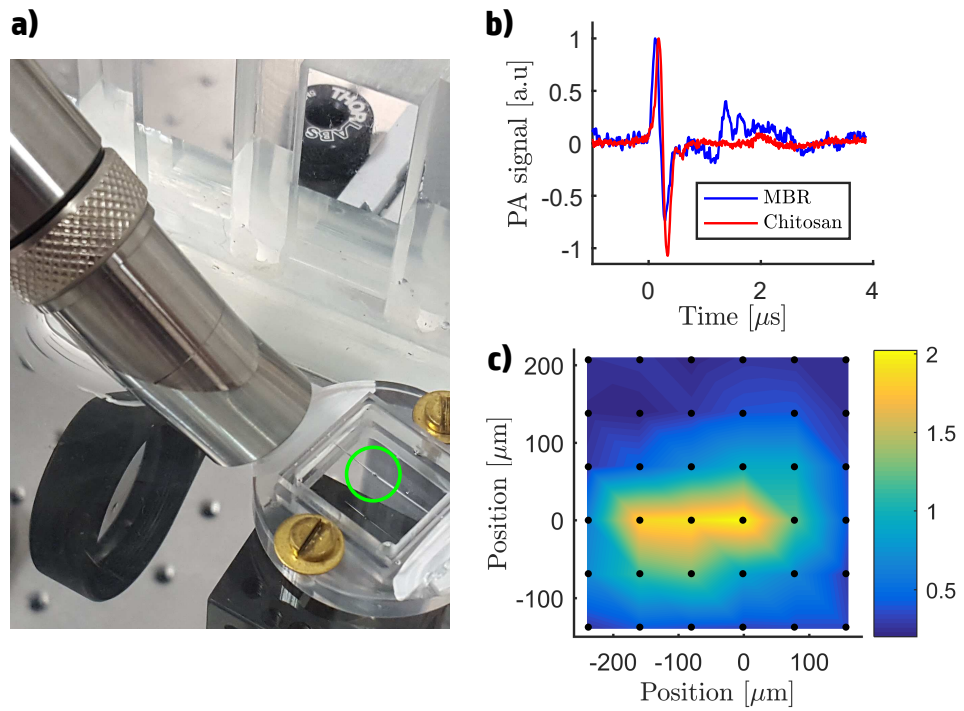


Figure 3.4: Panel a shows the configuration used to verify the PA generation from the GNRs inside the MBR using an ultrasound transducer. The MBR position is highlighted by the green circle. In panel b the PA signals for GNRs inside the MBR (blue curve) or imbued in a chitosan film (red curve) are compared. Finally, panel c is a 2D map of the PA intensity: the black dots represent the measurements, while the color map is an interpolation generated from these values.



## 3.2 Static contrast agent configuration

In this Section the proof-of-concept experiment demonstrating PA detection through the optical read-out of an MBR is presented. The Section focuses on a static configuration where the contrast agent contained in the microbubble is still. This configuration is the most adequate for a proof-of-concept experiment, since it removes the complexity associated with the flow of the contrast agent. This complexity is restored in Section 3.3, moving the system towards an application-like configuration.

### 3.2.1 Experiment description and read-out deduction

After the setup preparation described in Section 3.1, the first operation of the experiment was filling the MBR with the GNRs solution by enabling the peristaltic pump. After that, the peristaltic pump was disabled and kept off for the rest of the experiment to avoid mechanical perturbations on the MBR. A narrow resonance with an high contrast was then searched by scanning the probe laser wavelength and its contrast was further increased by acting on the polarisation controller. The resulting profile is shown in panel a of Figure 3.5, where  $s_{\text{opt}}$  is the normalised transmission of the photodiode detecting the MBR signal (PD, cfr. panel a of Figure 3.1) and  $\delta\nu = \nu - \nu_{\text{half}}$  is the detuning from the half-height point produced by the laser scan ( $\lambda_{\text{half}} = 1550.080$  nm,  $\nu_{\text{half}} = c/\lambda_{\text{half}}$ ).

After this optimization phase, the probe laser was set on the half-height point and the wavelength scan stopped, obtaining a flat trace (black curve in panel b), which represented the baseline of the experiment. The half-height point was the chosen work-point for the experiment to optimise the sensitivity of the detection, taking advantage of the high derivative in this point. After these preliminary operations, which prepared the probe subsystem for the PA detection, the pump laser was enabled. In correspondence of each pulse impinging on the MBR and triggering the PA emission, the MBR signal changed to a pattern featuring a major dipolar peak followed by decaying oscillations: the blue curve in panel b is an example of this kind of signals for a  $8 \text{ mJ/cm}^2$  fluence. In terms of the physical origin, this shape originates from the probe laser reading a different point of the resonance fringe as a consequence of the PA wave shifting the resonance position. These MBR signals were collected for various pump fluences, which were estimated by recording the energy meter signals and applying the procedure discussed in Subsection 3.1.1. It is important to highlight that the aforementioned procedure allowed to estimate the fluence produced by each single pulse.

Transmission patterns like the one in panel b of Figure 3.5 had to be converted into the optical shifts sustained by the WGM resonance in order to represent a measurement of the PA wave intensity. This was done by establishing a correspondence between the MBR transmission  $s_{\text{opt}}$  and the detuning from the half-height point  $\delta\nu$  using the unperturbed lineshape in panel a as reference. Initially, this correspondence was based on the WGM lineshape derived through the coupled mode theory presented in [134, 54, 55]. Indeed, this lineshape allowed a good reconstruction of the resonance on a wide detuning range (cfr. panel a), but it was less accurate in reconstructing the resonance fringe (cfr.

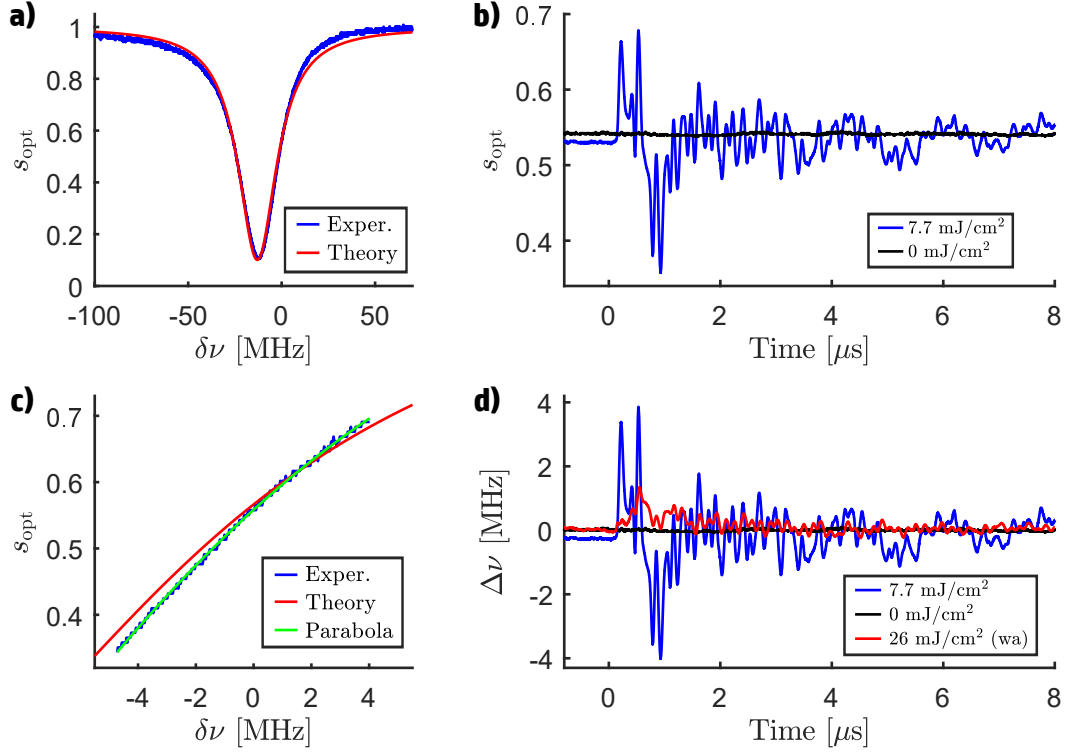


Figure 3.5: Series of panels resuming the raw signals recorded during the experiment and the conversion into resonance shifts. Panel a: WGM resonance selected for the experiment (blue curve) and fitting profile based on coupled mode theory (red curve). Panel b: transmission from the MBR when no PA generation is triggered (black curve) and when it is triggered by a 7.7 mJ/cm<sup>2</sup> fluence pulse (blue curve). Panel c: detail of the resonance fringe along with the different fitting curves used for its reconstruction. Panel d: resonance shifts associated with the signals shown in panel b, keeping the same color code. The red curve is the resonance shift produced by a 26 mJ/cm<sup>2</sup> fluence pulse for the MBR filled with plain water.

panel c). To improve on this key aspect, a parabolic function

$$s_{\text{opt}} = A(\delta\nu)^2 + B(\delta\nu) + C \quad (3.1)$$

was used in place of the theoretical lineshape and the fit range was limited to the fringe zone. Panel c shows the parabola resulting from this empirical approach and proves its effectiveness in reconstructing the experimental profile. Then, Equation 3.1 was inverted to set the correspondence between the transmission values  $s_{\text{opt}}$  and the detuning values  $\delta\nu$ , obtaining

$$\delta\nu = \frac{-B + \sqrt{B^2 - 4A(C - s_{\text{opt}})}}{2A} \quad (3.2)$$

In this formula, upon extracting the square root, only the + sign was used, since the detection of the PA wave was performed with the fringe on the blue-side of the resonance.

Additionally, the parameters ( $A$ ,  $B$ ,  $C$ ) are to be considered known since they have been estimated through the fringe fitting.

Finally, by inserting the transmission pattern produced by the PA perturbation into Equation (3.2) as the  $s_{\text{opt}}$  variable, the optical shift  $\Delta\nu$  induced in the WGM resonance could be retrieved. As an example, panel d of Figure 3.5 shows the  $\Delta\nu$  curve associated with the transmission pattern shown in panel b. The optical shifts  $\Delta\nu$  obtained with the procedure here presented are the read-out signals of the MBR transducer and their analysis allows to quantify the PA intensity and study the detection properties of the transducer.

Before moving to the signal analysis, a series of comments about the MBR read-out have to be made. First of all, the system showed good stability without an active locking mechanism (e.g. feedback on the wavelength of the probe laser) and the offset difference between the signals in panel d of Figure 3.5 is due to residual instabilities, producing small shifts. From a numerical point of view, these small shifts are particularly non-influential for the results of this Section, since the analysis is based on the computation of differential values and Fourier transforms.

Second, the MBR hit an optimal point in terms of sensitivity for the chosen GNRs concentration and fluence range. In fact, the PA wave produced resonance shifts close to the resonance width (half-width half-maximum  $\text{HWHM} = 12 \text{ MHz}$ ), causing the probe laser to read a considerable fraction of the fringe and therefore producing a raw transmission signal with a good visibility. The measurements would have been less effective with both a lower and an higher MBR sensitivity. In particular, a lower sensitivity would have produced a less visible oscillation, making more difficult to distinguish the signal from the noise; while, an higher sensitivity would have brought the probe wavelength in the out-of-resonance plateau, making the resonance shift not computable.

Finally, to verify the origin of the WGM perturbation, a test at full fluence ( $26 \text{ mJ/cm}^2$ ) with the MBR filled with plain water was made. The resulting signal (red curve, panel d Figure 3.5) shows that the water contribution is negligible if compared to the one of the GNRs when taking into account the great difference in fluence levels. In particular, as also shown in Subsection 3.2.2 through the Fourier analysis, the  $26 \text{ mJ/cm}^2$  water-only configuration produces a read-out that is comparable with the  $1 \text{ mJ/cm}^2$  GNRs configuration.

### 3.2.2 Read-out validation and Fourier analysis

During the experiment the GNRs were excited with different fluences in order to reconstruct their PA response curve, which served as a validation tool for the MBR transducer. This curve, in fact, was already studied in a previous article [80] for a GNRs batch produced with the same synthesis methods of the ones used in this experiment.

The PA response curve from the MBR data is shown in panel a of Figure 3.6 and it is a plot of the peak-to-peak value of the read-out signal  $\Delta\nu$  against the excitation fluence. The trend can be split into three parts and the red dashed line serves as a guide to the eye for a better visualisation. For fluences up to  $10 \text{ mJ/cm}^2$ , the excitation of the GNRs is stable and the PA response is linear with GNRs absorbance; for fluences between 10

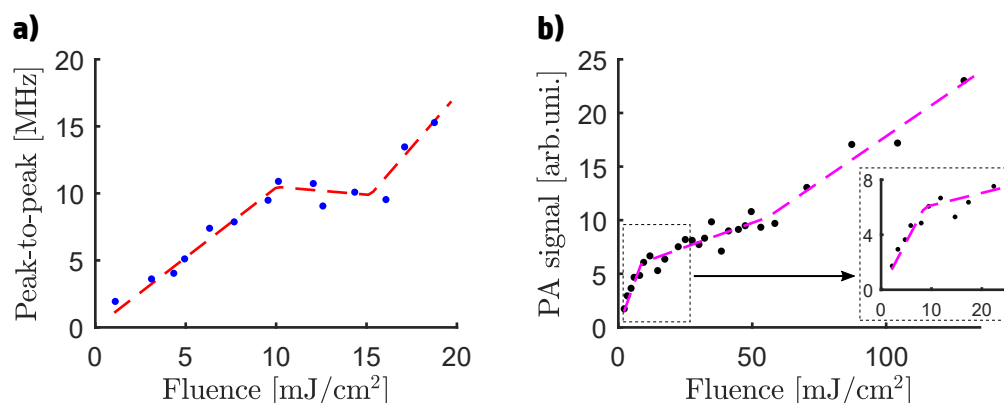


Figure 3.6: PA response trend measured through the MBR transducer (panel a) and an ultrasound transducer (panel b). Error bars are not shown in panel a, but the typical error is 0.22 MHz. Panel b is reproduced from the data in [80].

$\text{mJ/cm}^2$  and  $16 \text{ mJ/cm}^2$  the GNRs reshape into spheres and produce a sub-linear PA response; finally, for fluences above  $16 \text{ mJ/cm}^2$ , cavitation (evaporation of the water in proximity of the GNRs with consequent release of a vapour shockwave) onsets and PA response increases rapidly. For better visualisation, error bars are not shown in panel a, but the peak-to-peak values showed a good reproducibility, with each point having a standard deviation close to 0.22 MHz on a series of repeated acquisitions.

The PA response trend obtained with the MBR measurements agrees with the one of [80], which is reproduced in panel b of Figure 3.6 for a direct comparison. Even in this case the PA response can be split into three parts and the interpretation in terms of PA generation is the same of the previous paragraph. In particular, the reshaping threshold is the same for both experiment ( $10 \text{ mJ/cm}^2$ ), while the cavitation threshold differs ( $15 \text{ mJ/cm}^2$  vs.  $55 \text{ mJ/cm}^2$ ). This difference is attributed to the different environment hosting the GNRs: here, the GNRs were dispersed in water, while in [80] they were immobilized in a hydrated chitosan film. Despite the threshold difference, the two data sets produce the same PA emission regimes, validating the MBR system and proving its suitability for the characterisation of a PA contrast agent.

After this validation, the MBR dataset was studied in Fourier space to observe the frequency composition of the read-out signals and gain insight in the detection principle of the MBR transducer. Some of these Fourier spectra are reported in Figure 3.7 with the addition of the spectrum associated with the signal recorded when the MBR was filled with plain water (cfr. panel d of Figure 3.5). From these data, it is clear that the spectra are not flat and are, instead, concentrated in peaks at around 0.7 MHz, 3.7 MHz, 6.5 MHz and 9.55 MHz. Since the shift of the WGM resonance is ultimately generated by an elastic deformation of the MBR walls, a COMSOL Multiphysics<sup>®</sup> routine was used to reconstruct the mechanical eigenmodes of the MBR and it was found that the aforementioned frequencies are compatible with the MBR breathing modes.

This result shows that the mechanical modes of the microbubble have an important

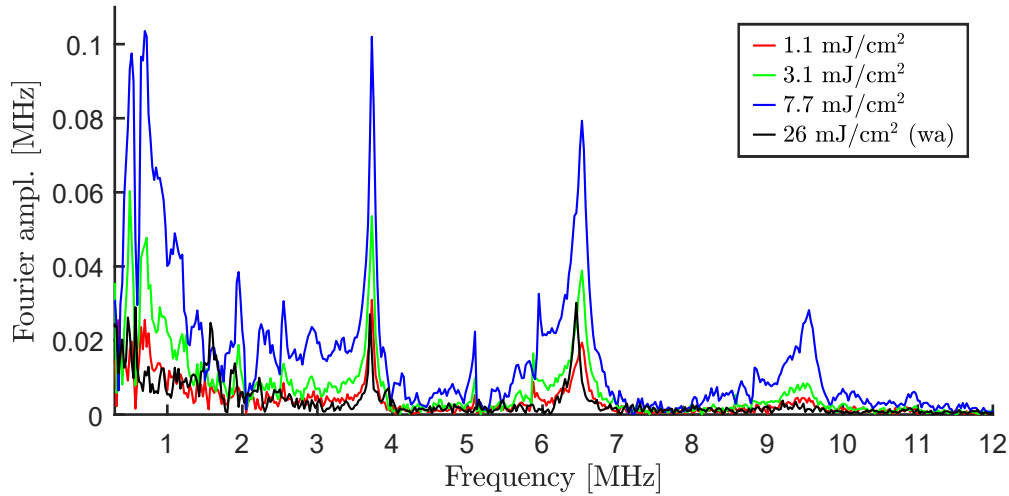


Figure 3.7: Fourier spectra of the MBR read-out signal  $\Delta\nu$  for different excitation fluences. The last spectrum (black curve) is obtained for an MBR filled with plain water.

role in the sensing mechanism, since they filter the mechanical action produced by the PA wave. In particular, the PA wave excites only a handful of the MBR mechanical modes, which dictate the deformation of the MBR walls through their superposition. This overall wall deformation is read through the WGM resonance, forcing only the frequencies associated with the excited mechanical modes to appear in the MBR read-out. This interpretation is reinforced by the behaviour of the spectra with respect to the excitation fluence: a change of fluence, in fact, produces an overall scaling of the spectra, but does not change the structure. In light of the previous interpretation, this means that the PA wave excites the same MBR mechanical modes, with PA intensity only dictating the overall mechanical energy loaded in the modes.

In agreement with the time domain signal discussed in panel d of Figure 3.5, the PA contribution of water is negligible with respect to the one of the GNRs, especially when considering the high fluence required to observe the water contribution. In particular, based on the comparison of the peaks height in Figure 3.7, a  $26 \text{ mJ/cm}^2$  fluence exposition on water produced a Fourier spectrum very close to the one produced by a  $1 \text{ mJ/cm}^2$  fluence exposition on the GNRs solution.

The presence of mechanical modes filtering the read-out of the PA signal represents a unique and promising feature for the MBR transducer. In fact, for example, the mechanical enhancement provided by these resonant modes could be exploited to lower the limit-of-detection of the transducer. Alternatively, the specific spectral fingerprint could be used to amplify the read-out signal through a lock-in technique or to differentiate a PA wave from environmental noise. In particular, the last possibility is demonstrated in Section 3.3, where the solution containing the contrast agent is flowing inside the MBR during the experiment. It is also important to highlight that the advantages of the MBR mechanical spectrum have to be framed in the context of a non-imaging PA application. In fact, a detector for PA imaging needs to have a flat frequency

response in order to reconstruct faithfully the frequencies making up the detected signal and, in turn, determine the size of the PA emitter. The MBR, for the aforementioned discussion, would not satisfy this requirement and, in fact, embedded microrings are a common solution for PA microscopes implementing a WGM transducer. In the case of microrings, the detection mechanism is based on a modulation of the refractive index, rather than a perturbation of the mechanical structure, and this produces the required flat frequency response [76, 77, 68, 60, 75].

### 3.2.3 FEM model and miniaturisation predictions

Finally, to further verify the PA detection of the MBR, a finite element method (FEM) model simulating the experimental setup was developed using COMSOL Multiphysics<sup>®</sup>. In this simulation the MBR was introduced as a bulge extending from a glass capillary, with its wall thickness deduced through a spherical approximation from a previous work [135]. The fillet connecting the MBR with the capillary was manually adjusted to give a reasonable profile. The capillary and the MBR were filled with a liquid simulating the GNRs suspension by having a  $5 \text{ cm}^{-1}$  optical density and the mechanical properties of water. The medium surrounding the MBR was a continuum of air. The pulse triggering the PA effect was represented as a Gaussian pulse illuminating uniformly the MBR.

In terms of computation, the simulation reproduced the cascade of thermal and mechanical phenomena triggered by the optical pulse to deduce, in the end, the deformation of the MBR walls and the shift of the WGM resonance [58, 78, 79]. The first phenomena to be accounted was the absorption of the optical pulse from the contrast agent and the conversion of the absorbed energy into heat (photo-thermal conversion). This was done by setting an uniform heat source  $Q_{\text{term}}$  [SI unit:  $\text{W}/\text{m}^3$ ] within the MBR core

$$Q_{\text{term}} = \mu_{\text{abs}} F , \quad (3.3)$$

where  $\mu_{\text{abs}}$  [ $\text{m}^{-1}$ ] is the absorption coefficient of the GNRs solution and  $F$  [ $\text{J}/\text{m}^2$ ] is the fluence of the laser pulse. Then, by taking advantage of the COMSOL modules *Heat Transfer in Fluids* and *Pressure Acoustics (Transient)*, it was possible to numerically solve the fluid dynamics Equations [58]

$$\left\{ \begin{array}{l} \rho C_p \frac{\partial T}{\partial t} = K \nabla^2 T + Q_{\text{term}} \\ \nabla^2 p - \frac{1}{v_s^2} \frac{\partial^2 p}{\partial t^2} = -\frac{\alpha}{v_s^2} \frac{\partial^2 T}{\partial t^2} , \end{array} \right. \quad (3.4)$$

$$(3.5)$$

obtaining the pressure perturbations  $p$  and temperature perturbations  $T$  produced by the heat source  $Q_{\text{term}}$  (thermo-elastic conversion), as well as and their propagation within the MBR core (acoustic propagation). In this Equations,  $\rho$  [ $\text{kg}/\text{m}^3$ ] is water density,  $C_p$  [ $\text{J}/(\text{Kg K})$ ] is water heat capacity at constant pressure,  $K$  [ $\text{W}/(\text{m K})$ ] is water heat conductivity,  $v_s^2$  [ $\text{m}^2/\text{s}^2$ ] is the speed of sound in water and finally  $\alpha = \partial P/\partial T$  [ $\text{Pa}/\text{K}$ ] is

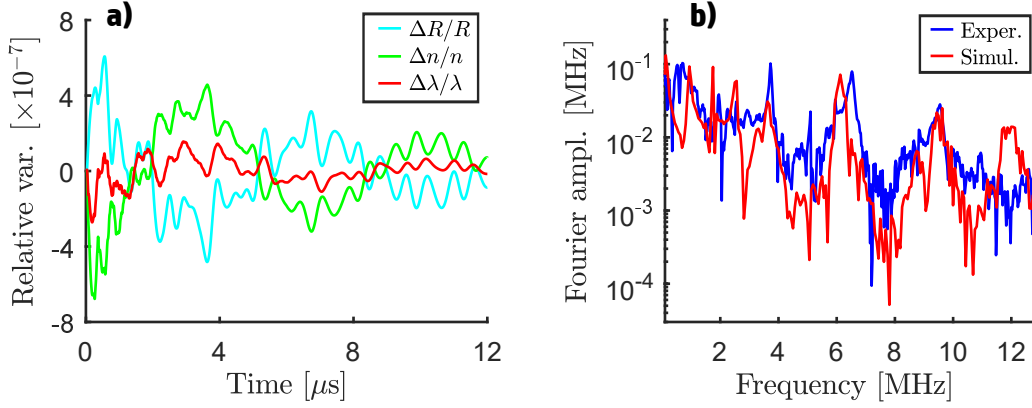


Figure 3.8: Results of the FEM simulation reproducing the PA generation and its detection through the MBR transducer. Panel a shows the relative variation of the MBR radius (cyan curve), of the walls refractive index (green curve) and of the resonance frequency (red curve). Panel b compares the Fourier spectrum of the simulated  $\Delta\lambda/\lambda$  (red curve, as in panel a) with the one found experimentally (blue curve, taken from Figure 3.7).

the pressure-temperature coupling parameter at constant volume for water. All previous parameters are referred to water since the GNRs are dispersed in this liquid. Finally, the module *Solid Mechanics* and the module *Acoustic-Structure Boundary* were used to compute the deformation of the MBR walls due to the pressure applied by the PA wave. Since the simulation accounted for the geometry of the MBR, it also intrinsically account for the mechanical modes of the microbubble, giving a faithful description of the walls vibration. From the walls deformation, it was then possible to compute the change of the MBR radius ( $R$ ) and the change of the walls refractive index ( $n$ ), allowing to estimate the WGM optical shift by assuming the approximate resonance condition

$$\lambda^{(\ell)} = \frac{2\pi R n}{\ell} \quad \left( \Rightarrow \quad \frac{\Delta\lambda}{\lambda} = \frac{\Delta R}{R} + \frac{\Delta n}{n} \right) , \quad (3.6)$$

where  $\lambda^{(\ell)}$  is the resonance wavelength and the positive integer  $\ell$  is the resonance order. This approximate resonance condition was preferred to the formal characteristic Equations (A.49) and (A.51) for its analytical simplicity and ease of computation.

In Figure 3.8 the results of the simulation are shown by plotting the relative shift  $\Delta\lambda/\lambda$  in panel a and its Fourier transform in panel b. The simulation produced a  $\Delta\lambda/\lambda$  compatible with the order of magnitude of the MBR signal, with the only imperfection being the reduced prominence of the initial dipolar peak. Since this prominent peak is present in the quantities  $\Delta R/R$  and  $\Delta n/n$  making up  $\Delta\lambda/\lambda$ , this cancellation is attributed to a series of geometrical and thermo-mechanical approximations made to simplify the construction of the model, which is described in detail in the Supplementary Material of [51]. In particular, since an expansion of the MBR produces a decrease in the density and viceversa, the  $\Delta R/R$  and  $\Delta n/n$  contributions tend to compensate and

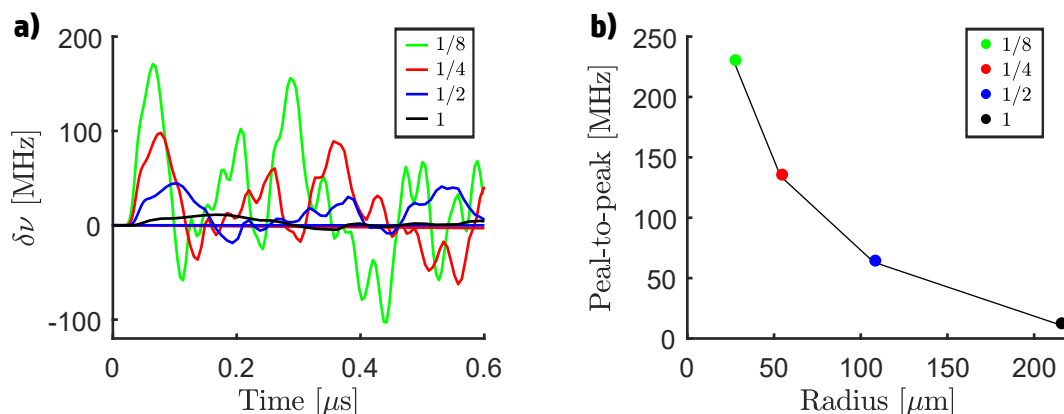


Figure 3.9: Prediction of the FEM simulation regarding the miniaturisation of the MBR transducer, assuming a uniform scaling of the system. Panel a shows the predicted MBR read-out signal, while panel b shows the peak-to-peak values against the MBR radius size. The color code, which is the same in both panels, is used to indicate the scaling factor.

therefore their comparison becomes critical. Despite this criticality, however, the factors here reported are reasonable and allow to gain insight in the physical process.

Moving to the spectral composition in panel b, instead, a remarkable agreement was found in the frequency range from 2 MHz up to 11 MHz, which is the bandwidth limit of the photodiode used in the experiment. Below 2 MHz, a certain mismatch was expected since the capillary length and the details of the transition fillet influenced this part of the spectrum. This dependency follows from the MBR mechanical modes, since fine structural details can modify the modes with the lowest frequencies [50]. In the end, by reproducing the physical processes leading to the resonance shift, the simulation confirmed the PA wave as the source of the oscillations seen in the experimental signal and confirmed the important role of the MBR mechanical modes in the sensing mechanism.

To predict the effects of miniaturisation on the system sensitivity, a series of simulations were run with different values for the MBR radius and the capillary diameter. Panel a of Figure 3.9 shows the predicted read-out signals for uniformly scaled replicas of the presented transducer, in particular for a 1/8, 1/4 and 1/2 scaling, assuming the same optical excitation. Since the response is higher for smaller transducers (panel b reports the peak-to-peak values for comparison), it is clear that the miniaturisation produces a better sensitivity, a characteristic which is at variance with standard ultrasound transducers [75]. To a first approximation, this feature can be explained by the reduction in mass produced by the miniaturisation; in fact, the same PA wave produces more deformation in a lighter MBR rather than an heavier one, therefore leading to an higher resonance shift and, consequently, to an higher sensitivity. In turn, this also means that smaller MBR are the most promising for lowering the limit of detection of the transducer. In practical terms, producing the scaling ratios associated with the simulations of Figure 3.9 requires a revision of the MBR fabrication method. In particular, the cap-



illary has to be tapered to the right diameter before inflating the microbubble in order to obtain the desired capillary-microbubble combination. In analogy with optical fibers, the tapering can be performed by heating the capillary to its softening temperature and then pulling its extremities: this procedure, however, is more critical for capillaries due to their allow structure. Indeed, developing a reliable tapering procedure, or a dedicated tapering system, represents a technological challenge for the miniaturisation of the MBR transducer and also represents an outlook for the presented activity.

### 3.3 Flowing contrast agent configuration

After the validation presented in the previous Section, the MBR transducer was challenged in a configuration simulating a flow cytometry experiment, with the GNRs running through the MBR during the measurements. As shown in the following, the constant flow produced a strong noise in the MBR transmission and therefore a different approach, based on Fourier transforms, was used to reconstruct the PA response trend and validate the MBR transducer. No change was made to the setup, except for the substitution of the MBR with one having a 540  $\mu\text{m}$  diameter (82 nl volume) and using a GNRs solution concentrated to 1 mM Au (GNRs: 3.2 nM) instead of 4 mM Au (GNRs: 13 nM). This dilution constituted an additional challenge for the system, since it reduced by the same amount the number of PA emitters inside the MBR.

#### 3.3.1 Experiment description

The system was preprepared for the measurements retracing the steps described in Section 3.2 for the static configuration. In particular, the peristaltic pump was enabled to fill the MBR with the GNRs solution and then left running to establish a constant flow inside the MBR. A narrow and deep WGM resonance was then searched, and its contrast was optimized through the polarization controller, obtaining the profile in panel a of Figure 3.10. Differently from the static configuration, the resonance slowly moved back and forth around a central position, producing an oscillation with a period of a few seconds. This oscillation was attributed to both the contrast agent moving inside the MBR and the tension applied on the capillary stem by the peristaltic pump through the connection tubings. After the contrast optimisation, the probe laser was set on the half-height point ( $\lambda_{\text{half}} = 1550.214 \text{ nm}$ ) and the wavelength scan stopped, obtaining the baseline of the experiment (black curve, panel b). At variance with Section 3.2, the work-point did not stay indefinitely on the half-height point, but moved to different positions along the fringe due to the slow back-and-forth of the resonance. Additionally, the baseline trace was not flat and featured noise oscillations. As for the slow back-and-forth, this noise originated from the flow of the contrast agent within the MBR, but developed on a very different time scale: microseconds rather than seconds.

After this preparation steps, the data acquisition proceeded as in Section 3.2: the pump laser was enabled, the MBR signal  $s_{\text{opt}}$  was recorded for each pulse impinging on the MBR and the acquisition was repeated for different fluences. The blue curve in panel

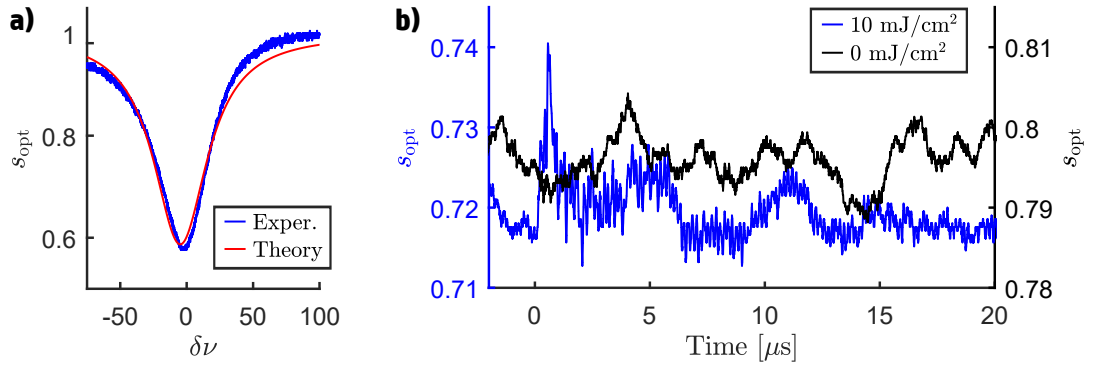


Figure 3.10: Panel a shows the WGM resonance resonance used for the PA sensing. Panel b, instead, shows the baseline of the experiment (black curve) and the oscillations in MBR transmission produced by a PA wave (blue curve).

b of Figure 3.10, obtained for a  $10 \text{ mJ/cm}^2$  fluence, is an example of the recorded signals. Using the resonance in panel a as reference and applying the empirical method discussed in the previous Section, the raw transmission traces were converted into the optical shifts  $\Delta\nu$  sustained by the WGM resonance. Since the work-point moved along the resonance fringe from acquisition to acquisition, the parabolic fit was recentred and repeated each time. This resulted in optical shifts easier to compare since they are centred on the  $\Delta\nu = 0$  line. Panel a of Figure 3.11 shows as examples the results associated with the raw transmission signals from panel b of Figure 3.5, keeping the same color code. The MBR read-out signals  $\Delta\nu$  in flow configuration differ from the ones in static configuration (cfr. panel d, Figure 3.5) since the initial bipolar peak is substituted with a single-side peak and the secondary oscillations have a reduced prominence. One can also notice that the frequency of the secondary oscillations is not present on the baseline trace. This last evidence, as well as a not-easy to define peak-to-peak value, moved the analysis towards the Fourier components, in analogy with Figure 3.7.

### 3.3.2 Detection through Fourier spectrum

As shown in panel b of Figure 3.11, the transform of the baseline (black curve) is mostly flat, with the exception being the zone below 2 MHz, where a decay can be noticed. Instead, the PA read-out transforms (blue and red curves) are concentrated in a couple of major peaks at 3.25 MHz and 5.75 MHz, and a couple of minor peaks at 4.75 MHz and 8.5 MHz. As discussed in the previous Section, these frequencies are associated with the mechanical modes of the MBR, in particular its breathing modes. Since the the transform of the baseline is practically null for any frequency above 2 MHz, it was possible to use the aforementioned peaks as detection flags for the PA emission. As consequence, the PA intensity was measured through the amplitude of one of the Fourier peaks: in particular the 5.75 MHz peak, due to its prominence. In terms of signal-to-noise ratio (SNR), this approach led to a value of 17 ( $67 \cdot 10^{-3}$  vs  $3.9 \cdot 10^{-3}$ ) for the  $10 \text{ mJ/cm}^2$  case and 14 ( $53 \cdot 10^{-3}$  vs  $3.9 \cdot 10^{-3}$ ) for the  $5 \text{ mJ/cm}^2$  case. Both values

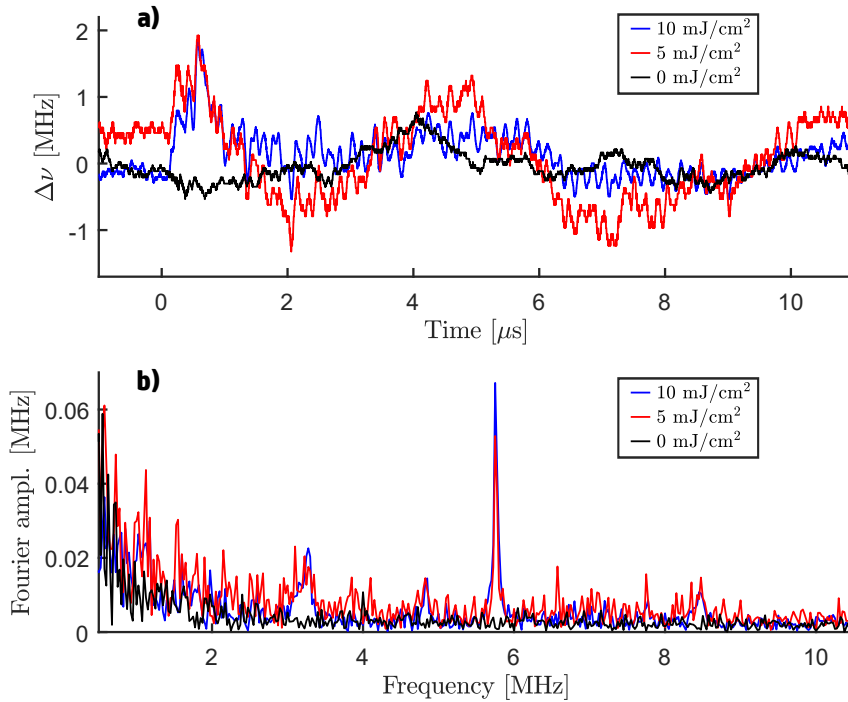


Figure 3.11: Resonance shifts  $\Delta\nu$  produced by the PA wave (panel a) and their Fourier transforms (panel b).

are significantly higher than the ones obtained directly from the time-domain signals using, for example, the height of the initial peak: 2.9 (2.0 vs 0.70) for the 10 mJ/cm<sup>2</sup> case and 2.1 (1.5 vs 0.70) for the 5 mJ/cm<sup>2</sup> case.

The effectiveness of this Fourier-based detection method is a consequence of the mechanical spectrum of the MBR and the different modes involved during the background and the signal acquisitions. In the first case, in fact, the pressure applied by the liquid flow excites low-frequency modes (cfr. black curve in Figure 3.11b), while in the second case the PA wave excites high-frequency modes (cfr. red and blue curves in Figure 3.11b). This clear difference in frequency allows to decouple the noise contribution from the PA wave contribution, producing an almost background-free PA detection through the modes above 4 MHz and, therefore, leading to an high SNR measurement. Indeed, this Fourier-based detection proves the utility of the MBR mechanical spectrum in environments with high mechanical noise, as in a flow cytometry experiment.

As for the static configuration, the read-out of the MBR transducer was validated by the reconstruction of the PA response against the excitation fluence. In this case, the PA response was quantified through the height of the 5.75 MHz Fourier peak, obtaining the plot in Figure 3.12. This trend is consistent with the one found in the previous Section as well as the reference trend in [1]: the GNRs undergo a stable excitation up to 5 mJ/cm<sup>2</sup>, a reshaping regime from 5 mJ/cm<sup>2</sup> to 10 mJ/cm<sup>2</sup> and then a cavitation regime above 10 mJ/cm<sup>2</sup> (black curve as guide to the eye). With respect to the static configuration

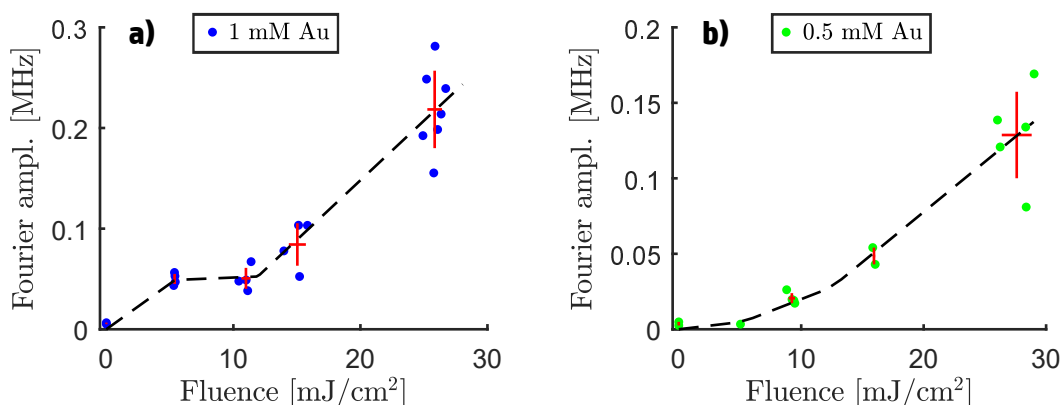


Figure 3.12: PA response trend measured through the MBR transducer for two GNRs colloidal solution, having a 1 mM Au concentration (panel a) and a 0.5 mM concentration (panel b) respectively. In both panels the red crosses mark the average and the standard deviation of the measurements groups.

(cfr. panel a of Figure 3.6), the data points are more spread and the fluence thresholds are shifted by roughly 5 mJ/cm<sup>2</sup>.

As a final challenge, the PA response trend was also measured for a 0.5 mM Au solution, proving sensitivity of the MBR transducer towards the concentration of the contrast agent, and also suggesting 0.5 mM Au (GNRs: 1.6 nM) as the limit concentration for the implemented experimental configuration. At variance with the previous concentration, in fact, a non-zero amplitude is produced only for fluences above 5 mJ/cm<sup>2</sup> and the trend is more akin to a simple line, not distinguishing between the PA generation regimes.

### 3.4 Conclusions

In this Chapter the implementation of a microbubble resonator as an all-optical PA transducer for the characterisation of a PA contrast agent has been described. The presented configuration exploited the MBR in the double role of sensor and vial containing the contrast agent under analysis. This led to an ultra-compact configuration that was able to test a liquid sample below 100 nl and did not use any acoustic matching medium, representing a strong reduction in volume if compared with configurations implementing standard ultrasound transducers (cfr. Figure 3.4).

The system was initially studied in a static configuration and its optical PA read-out was validated by reconstructing the PA response curve of an aqueous solution of GNRs, obtaining the trend found in literature. In addition, a FEM model was used to simulate the long chain of physical phenomena making up the PA effect and to predict the resonance shift, finding particular good agreement between the experimental and the simulated Fourier composition. By inspection of the Fourier spectrum, it was revealed that the MBR sensing mechanism is based on the filtering of the PA wave through the

discrete mechanical modes of the MBR.

The system was then challenged with a second experiment simulating a flow cytometry configuration, with the contrast agent continuously flowing within the MBR. Since the liquid flow caused an increased noise level in the time-domain read-out trace, the analysis moved to Fourier space exploiting the filtering action of the MBR mechanical modes. With this approach SNR was greatly increased and the the height of the most prominent peak was used as the measurement of the PA intensity. As in the first experiment, the PA response trend of the contrast agent was reconstructed and the limit of detection for the presented system was estimated to be a 1 nM GNRs concentration.

The experiments discussed in this Chapter open the possibility of implementing the MBR transducer in non-imaging PA applications, taking advantage of its extreme compactness and its mechanical features. In particular, the MBR little size is promising for on-chip implementations and portable devices, especially in contexts where the sampled material is limited or must be kept to a minimum. For example, the MBR could be implemented for the measurement of blood oxygenation through the PA response of the heme group, while allowing an extremely little blood draw.

The FEM model allowed to predict the performance of the MBR transducer with respect to miniaturisation, finding that scaling down the system increases its sensitivity towards the PA perturbation. This feature is at variance with piezoelectric ultrasound transducers and represents a strong motivation towards the improvement of the MBR fabrication technique.

Another important and unique feature of the MBR transducer is its mechanical spectrum and its possible exploitation to increase the performance of the device. For example, positive interference could be used to increase the PA response and lower the limit-of-detection, or the spectral fingerprint could be used to amplify the read-out signal through a lock-in technique. Alternatively, the mechanical spectrum can be exploited as a filter to reduce the environmental noise, as demonstrated with the simulated flow-cytometry experiment. In this regard, the noise decoupling and the consequent increase in SNR are promising for various in-vivo flow-cytometry applications, such as the measurement of blood cells oxygenation, the detection of venous thrombi and/or circulating tumor cells. In all these cases, in fact, the noise decoupling could reduce the effects of physiological noise (e.g. heart beat and/or respiration) and the increased SNR could lower the excitation fluences and/or the contrast agents concentration used by practitioners. In addition, the extremely small volume, the direct implementation and the absence of an acoustic impedance-matching material are promising elements for wearable appliances and/or an endoscope.

Finally, the applicability range of the MBR transducer extends beyond the medical area: in particular, applications in biology, material science and chemistry could benefit from its features. For example, the transducer could be used as a compact biosensor or as a gauge for development of new contrast agents. Additionally, the MBR would allow to interrogate the hosted material with an high repetition rate, ultimately limited by the decay time of the MBR mechanical modes. For the system here presented this limit is close to 40 kHz and would allow, for example, to track the evolution of a chemical

reaction with a 25  $\mu\text{s}$  time step by measuring the PA response of one reagent (e.g., growth of GNR, oxidation of the heme group).

# Chapter 4

## Absorption sensing

In this Chapter the absorption spectrum of nanoparticles is measured through the temperature variation they induced in a microbubble resonator (MBR), proving the possibility for the microbubble to reconstruct the nanoparticle absorption spectrum without relying on a light extinction measurement.

The Chapter starts with a description of the experimental setup (Section 4.1), where the MBR takes the double role of micro-vial containing the nanoparticles and optical thermometric sensor. Then, the experiment demonstrating the absorption measurement is described (Section 4.2), starting with a demonstration of the MBR thermal sensitivity (Subsection 4.2.1) and ending with the estimate of the nanoparticles absorption coefficient (Subsection 4.2.2).

### 4.1 The experimental setup

Panel a of Figure 4.1 shows the setup used to demonstrate the measurement of the nanoparticle absorption spectrum. This setup is analogous to the one used in Chapter 3) for the photoacoustic (PA) sensing and is divided into three subsystems aimed at specific tasks.

The microfluidic subsystem comprises the elements on the bottom-right corner of the setup sketch and was used to load the solution containing the nanoparticles into the MBR. Even in this case, the MBR was connected to a flexible polymer tubing (Tygon R-3607, Saint-Gobain, La Défense, Courbevoie, France) and a peristaltic pump (Minipuls 3, Gilson, Middleton, WI, USA) was used to draw the solution from a reservoir. As in Chapter 3, the nanoparticles chosen for the experiment were gold nanorods (GNRs), which represented again a natural benchmark due to their applications history [72, 71, 74, 69, 70, 73]. and their tunability in terms of absorption spectrum. In particular, the GNRs of this experiment were synthesised to have their plasmonic resonance centred at 750 nm, and were then PEGylated and concentrated to 3 mM Au. Even in this case, the synthesis was performed with the seed-mediated approach and the GNRs were dispersed in water [82, 69].

The MBR was mounted on a metallic holder connected to a micrometric stage and

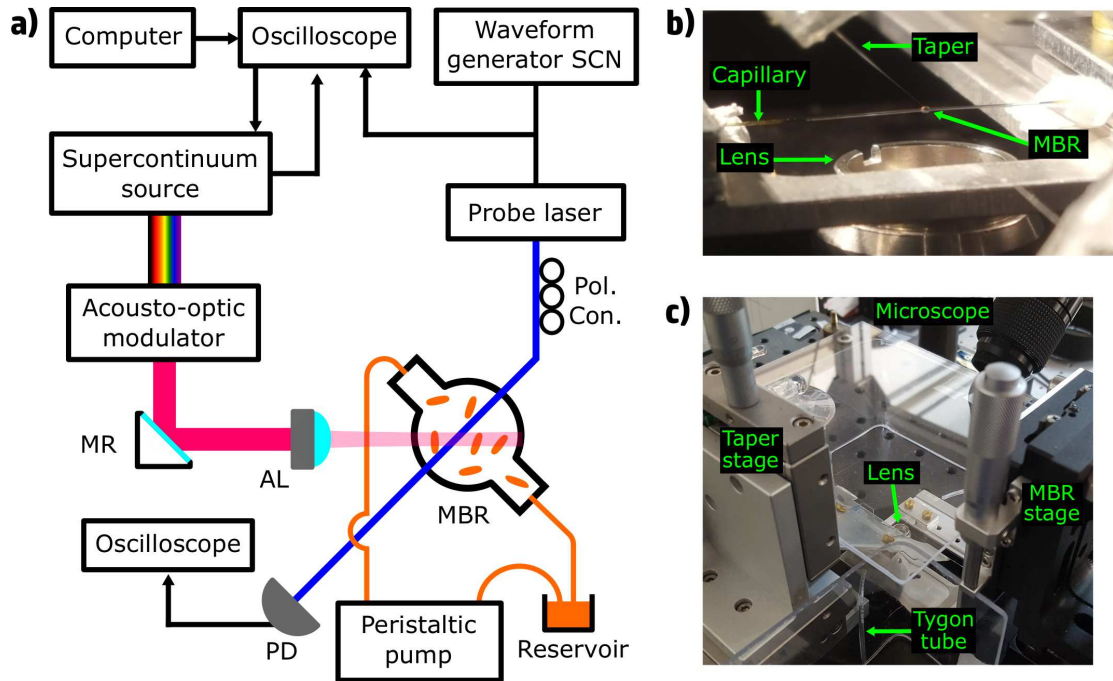


Figure 4.1: Panel a: sketch of the experimental setup used to measure the absorption spectrum of nanoparticles through an MBR. Panel b: MBR coupled to the tapered fiber and positioned in the focus of the aspherical lens. Panel c: overview picture showing the micrometric stages, the microscope and the PMMA walls enclosing the MBR area.

was positioned in the focus point of an aspherical lens (cfr. panel b of Figure 4.1). The area around of the MBR was shielded with transparent PMMA walls to avoid air currents on the microbubble (cfr. panel c). The MBR was fabricated using the arc discharge technique [20, 21, 131] (base capillary: Z-FSS-100-165, Postnova Analytics GmbH, Landsberg, Germany).

The pump subsystem, instead, comprises the elements on the left side of the sketch and was aimed at illuminating the GNRs contained in the MBR with different wavelengths. This was done by filtering the emission of a collimated free-space supercontinuum source (SuperK COMPACT, NKT Photonics, Birkerød, Denmark; spectral range 400-2400 nm; repetition rate up to 20 kHz) with an acousto-optic modulator (SuperK SELECT, NKT Photonics, Birkerød, Denmark; spectral range 680-1100 nm) and focusing the resulting beam on the MBR with an aspherical lens (C110TME-B, Thorlabs, Newton, NJ, USA; focal distance 2.4 mm; labelled AL in the sketch). The 45-degree mirror (MR) was used to achieve an inverted microscope configuration, which allowed to prepare the setup more easily. At variance with Chapter 3, the beam here was strongly focused by the aspherical lens and produced a beam waist of 36  $\mu\text{m}$ , which was one order of magnitude below the MBR radius (details in Subsection 4.1.1).

A computer was used to interface with the supercontinuum source and with the acousto-optic modulator to set a series of emission parameters, such as the repetition



rate, the emission trigger and the pass-through wavelength. In particular, for the purposes of this experiment, the repetition rate was set at 20 kHz, the laser operated in a gated configuration and various lines between 680 nm and 1100 nm were used to excite the nanoparticles and reconstruct their absorption spectrum. Laser emission was enabled through a square pulse provided by the built-in generator of the oscilloscope (MDO4000C, Tektronix, Beaverton, OR, USA) and an on-emission feedback signal from the laser was used to time the oscilloscope acquisition. Because of this closed-loop communication between the two instruments, it was possible to run the experiment programmatically through a script controlling the oscilloscope. The programmatic control allowed to minimize the experiment dead times, avoid user errors from repetitive tasks and automatize file indexing for better book-keeping. In practical terms, it was implemented through a MATLAB<sup>®</sup> script interfacing with the oscilloscope through the VISA protocol.

Finally, the probe subsystem comprises the elements on the right side of the sketch and was used to measure the shift induced in a microbubble Whispering Gallery Mode (WGM) resonance by the nanoparticle absorption. In particular, the optical shift measured the temperature increase of the MBR walls, which was caused by the nanoparticles absorbing the impinging beam from the supercontinuum source and heating the host solution. By acquiring these temperature shifts for different impinging wavelengths and applying the analysis described in Section 4.2, it was possible to finally reconstruct the nanoparticle absorption spectrum.

In practical terms, the probe subsystem featured the same elements used in the setup of Chapter 3. In particular, even in this case an home-made tapered fiber [53] was used to couple the MBR with a CW infrared fiber laser (Koheras ADJUSTICK, NKT Photonics, Birkerød, Denmark; spectral range 1550-1551 nm; labelled as probe laser in the setup sketch). The fiber was placed in contact with the MBR equator through a set of micrometric stages with the aid of a long working-distance microscope (custom model, Navitar, Rochester, NY, USA), as shown through panels b and c of Figure 4.1. A polarization controller (Pol.Con.) was used to optimise the MBR-taper coupling by selecting the correct light polarisation and the system transmission was recorded through an InGaAs photodiode (PDA400, Thorlabs Newton, NJ, USA; bandwidth 10 MHz; PD). A waveform generator (Keysight 33220A, Agilent Technologies, Santa Clara, CA, USA; SCN) allowed to finely set the probe laser wavelength and perform a 1 GHz frequency scan. In addition to coupling the probe laser with the MBR, the tapered fiber was also used to position the MBR in the aspherical lens focus. During the setup preparation, in fact, the beam focus was located by passing the fiber in front of the lens and simultaneously observing through the microscope the red light it scattered. Once the maximum scattering point was found (i.e the focus), the fiber was risen by one MBR radius and the MBR placed beneath it.

#### 4.1.1 Auxiliary measurements

During the preparation of the setup a series of auxiliary measurements were performed to characterise the illumination of the GNRs.

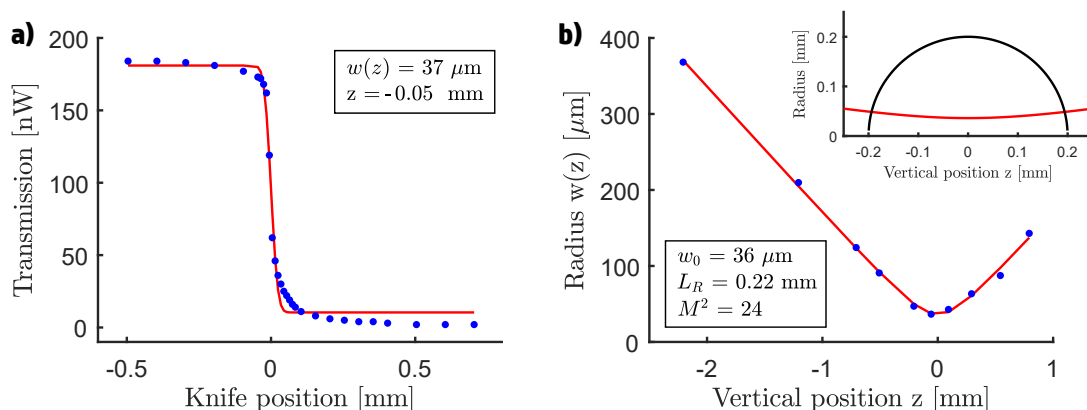


Figure 4.2: Results of the knife edge measurements. Panel a shows the S-shaped transmission produced by the beam blockage, while panel b shows the beam radius for different heights. In both panels the blue dots represent the experimental data, while the red curves represent fitting functions. The inset of panel b shows the beam radius function (red curve) against the profile of a 200  $\mu\text{m}$  radius MBR (black curve).

First of all, knife edge measurements were performed to check the focusing produced by the aspherical lens. The results of these measurements are reported in Figure 4.2 and show a strong focusing of the beam, leading, in particular, to a 36  $\mu\text{m}$  beam waist ( $w_0 = 36 \mu\text{m}$ ) and a 0.22 mm Rayleigh length ( $L_R = 0.22 \text{ mm}$ ). In practice, this level of focusing produced an optical coring of the MBR, with only the GNRs at the center of the MBR to be illuminated. The inset of panel b shows this aspect more clearly by comparing the beam radius  $w(z)$  against the profile of an MBR having a 200  $\mu\text{m}$  radius, and using the same scale for both the vertical and the horizontal axis. As previously described, this strong focusing required a careful positioning of the MBR, but it also assured that all the energy from the beam was channelled on the MBR to excite the nanoparticles.

After the knife edge measurements, the emission lines of the acousto-optic modulator were analysed through a spectrometer (SPM-002-XT64, Photon Control, Burnaby, B.C., Canada) to characterise the excitation of the GNRs. In practical terms, this was achieved by positioning a collection fiber in place of the MBR and sending the collected light to the spectrometer. Additionally, to protect the spectrometer CCD, an OD 3 neutral filter was placed before the aspherical lens for the duration of the measurements. Figure 4.3 shows 42 emission lines covering the 680 nm - 1100 nm wavelength range with a 10 nm step. Since the acousto-optic modulator was set to launch one line at a time, each line shown in Figure 4.3 was independently measured and the plot itself is a superposition of the 42 measurements. Additionally, since the modulator was able to produce a line centred on any user-defined wavelength in the 680 nm - 1100 nm range, the lines here shown are to be considered as an arbitrary selection made to represent the modulator emission.

From Figure 4.3 one can notice an average linewidth of 5 nm and a decrease in peak

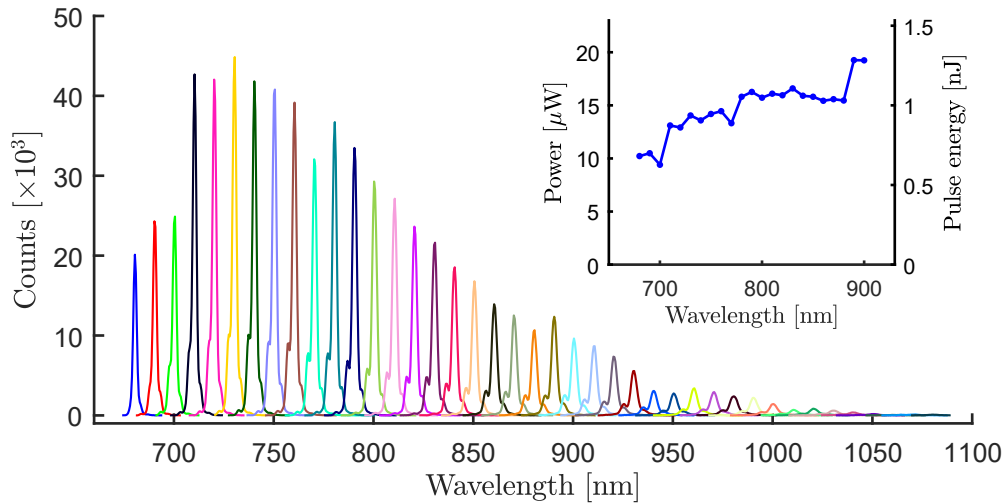


Figure 4.3: Collection of 42 emission lines from the acousto-optic modulator as measured by the spectrometer: each line was independently recorded and this plot is a superposition of the 42 acquisitions. The inset in the top-right corner shows the optical power and the pulse energy associated with each line.

height for increasing wavelength, particularly between 780 nm and 900 nm. This decrease, however, is apparent and caused by a combination of the CCD quantum efficiency (silicon) and the transmission of the OD 3 filter. Once that these aspects are taken into account, the lines have a similar amplitude and their optical power is almost constant, as shown in the inset in the top-right corner. Regarding this last point, the optical power of each line was computed by integrating its spectrometer counts along the wavelength axis and then converting the overall sum from counts to a power value. The last operation was done with the aid of a calibrated power meter (Ophir PD300, MKS Instruments, Andover, MA, USA), which allowed to establish a counts-power correspondence based on the reading of the 680 nm line. Additionally, by dividing the optical powers for the repetition rate (15 kHz in this case), it was possible to estimate the pulse energies, obtaining a value close to 1 nJ for each line (vertical axis on the right side of the inset). This energy value leads to a  $24 \mu\text{J}/\text{cm}^2$  excitation fluence, which is three orders below the fluence of Chapter 3 and therefore allows to observe the heating of the nanoparticle without triggering any noticeable PA wave.

## 4.2 Experiment description

In this Section the experiment aimed at measuring the nanoparticles absorption spectrum through the MBR resonator is described. The Section starts by demonstrating the MBR sensitivity towards the thermal perturbation induced by the nanoparticles absorption (Subsection 4.2.1) and then continues with the measurement of the nanoparticles absorption coefficient through the temperature shift sensed by the MBR (Subsection

4.2.2).

### 4.2.1 Demonstration of thermal sensitivity

After the preparation described in Section 4.1, the system was set up for the measurements in analogy with Chapter 3. First of all, the MBR resonator (radius: 210  $\mu\text{m}$ , base capillary: Z-FSS-100-165, Postnova Analytics GmbH, Landsberg, Germany) was filled with the water-based solution containing the GNRs by enabling the peristaltic pump, which was then turned off after the filling. Then, while keeping the supercontinuum emission disabled, a WGM resonance with an high contrast was searched by scanning the probe laser and its contrast was optimised by acting on the polarisation controller. This resonance, shown as the black curve in panel a of Figure 4.4, represented the unperturbed reference profile of the experiment. As in Chapter 3, the variable  $s_{\text{opt}}$  in Figure 4.4 is the normalised transmission of the photodiode reading the MBR signal (PD, cfr. panel a of Figure 4.1), while the variable  $\delta\nu = \nu - \nu_{\text{half}}$  is the detuning from the half-height point produced by the probe wavelength scan ( $\lambda_{\text{half}} = 1550.024 \text{ nm}$ ,  $\nu_{\text{half}} = c/\lambda_{\text{half}}$ ).

After this preparation, the supercontinuum laser was enabled and the resonance began to shift towards lower optical frequencies. The presence of such a shift was the proof of the MBR sensitivity towards the thermal perturbation produced by the GNRs heating. While the resonance was shifting, the oscilloscope acquisition was triggered after a set exposure time, performing an on-the-fly recording of the resonance position. This procedure was repeated for different exposure times and different excitation lines, with both the unperturbed and the shifted resonances recorded for each combination. As example, panel a shows in blue the shifted resonance associated with a two seconds exposure while illuminating the MBR with the 760 nm line. At variance with the PA measurements of Chapter 3, here the scan of the probe wavelength was not stopped and allowed to constantly observe the resonance and its position.

To evaluate the optical shift induced by the GNRs heating, the detuning distance  $\Delta\nu$  between the half-height point of the unperturbed resonance and of the shifted resonance was computed. In practise, this was done by fitting with a parabolic function the fringes of both resonances, computing the detuning associated with the half-height points using Equation (3.2) and then subtracting these values to obtain  $\Delta\nu$ . Panel b exemplifies this calculation for the case shown in panel a, with the two half-height points being at detuning 0 MHz and - 90 MHz, respectively, and therefore giving an optical shift  $\Delta\nu = -90 - 0 = -90 \text{ MHz}$ . Since the heating moves the resonance towards negative detuning,  $\Delta\nu$  is a negative quantity; however, in the following of the Chapter, its absolute value is used for the graphics, to more easily quantify the effects of the GNRs heating.

The optical shifts  $\Delta\nu$  obtained for the tested wavelength-exposure combinations are shown in panel a of Figure 4.5. The seven curves in panel a, which connect the shifts sharing the same exposure time, show a peak at 780 nm that is compatible with the GNRs plasmonic resonance. One could consider these curves as a measurement of the GNRs absorption spectrum, but this interpretation is hindered by the rather long exposure times, which ranged from 0.5 s to 3.5 seconds. For long exposures, in fact, the heat

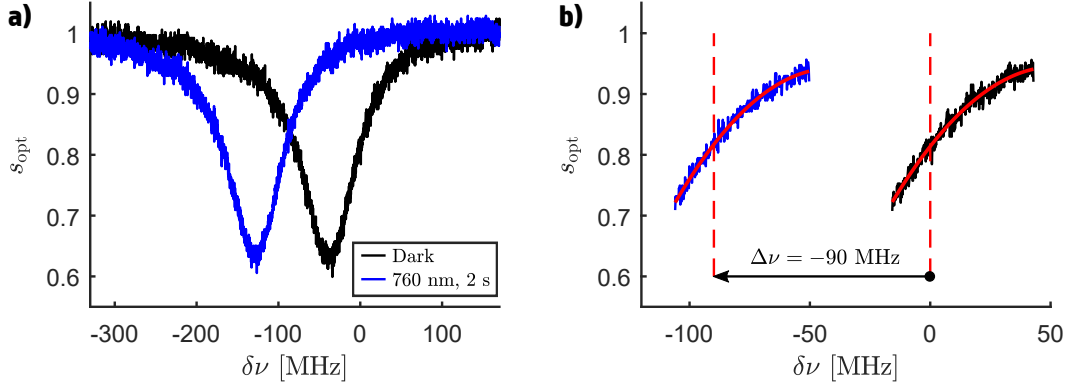


Figure 4.4: Panel a: position of the WGM resonance when the GNRs are not illuminated (black curve) and when they are for two seconds using the 760 nm line (blue curve). Panel b: plot of the resonance fringes (same color code of panel a) along with the parabolic fit (red curves) used to compute the optical shift  $\Delta\nu$ .

dissipation of the system towards the surrounding environment plays an important role in the thermal dynamics, and any data analysis or interpretation must take this aspect into account. This is particularly evident with the 3 s and 3.5 s expositions, where the system reached thermal equilibrium, with heat dissipation balancing heat generation from GNRs absorption. Measurements with shorter exposures, which are discussed in the following Subsection 4.2.2, allowed a more faithful reconstruction of the nanoparticles spectrum, since it was possible to neglect heat dissipation to a first approximation.

Using the fused silica thermo-optical coefficient  $\alpha = 12 \cdot 10^{-6} \text{ K}^{-1}$  [136], the optical shifts  $\Delta\nu$  were converted into temperature shifts  $\Delta T$  using the approximate resonance condition given by Equation (3.6). In particular, since Equation (3.6) implies the equivalence of the relative variations, one can write

$$\frac{\Delta\nu}{\nu} = \frac{\Delta n}{n} = \frac{\alpha \Delta T}{n} \quad \Rightarrow \quad \Delta T = \frac{n}{\alpha} \frac{\lambda}{c} \Delta\nu \quad (4.1)$$

where, on the right side,  $n$  represents the unperturbed refractive index of silica (1.44) and  $\lambda$  represents the unperturbed resonance wavelength, which can be approximated to  $\lambda_{\text{half}}$ . At variance with the PA modelling discussed in Subsection 3.2.3 and Equation (3.6), here only the refractive index variation was considered, since no mechanical perturbation acted on the MBR walls. The temperature shifts  $\Delta T$  are shown through the vertical axis on the right side of panel a and prove the sensitivity of the MBR to thermal perturbation in the order of tens of millikelvin.

For comparison purposes, the entire acquisition process and analysis was repeated for an MBR filled with plain water. In this case the optical shifts were smaller and produced a flat wavelength profile rather than a peak, as shown in panel b of Figure 4.5. These results are interpreted as a residual absorption of water in the 680 - 1100 nm spectral window [137] and show that water contribution is significantly below the one of the GNRs suspension ( $\mu_{\text{GNR}} \approx 5 \text{ cm}^{-1}$  vs.  $\mu \approx 0.1 \text{ cm}^{-1}$ ).

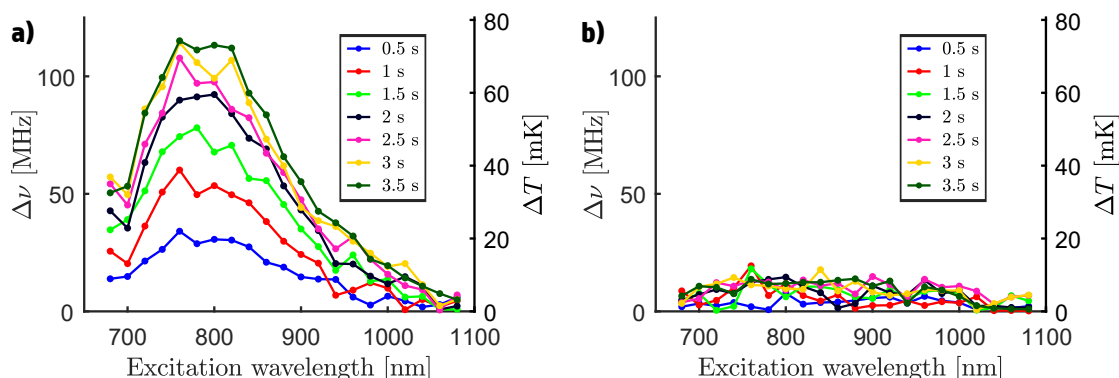


Figure 4.5: Resonance shifts induced by illuminating the MBR with different excitation wavelengths and different exposure times when the MBR was filled with the GNRs colloidal solution (panel a) or plain water (panel b). The right vertical axis shows the associated temperature shift deduced from Equation (4.1).

#### 4.2.2 Measurement of the absorption spectrum

After the demonstration of thermal sensitivity described in Subsection 4.2.1, a different acquisition procedure was used to quantify the thermal shifts for shorter exposure times. This alternative approach consisted in an acquisition procedure analogous to the one implemented for the PA experiment, with the probe wavelength scan disabled during the acquisitions. No changes were made to the experimental setup, except for the substitution and re-alignment of the MBR (radius: 200  $\mu\text{m}$ , base capillary: Z-FSS-100-165, Postnova Analytics GmbH, Landsberg, Germany).

In analogy with the PA experiment, the probe laser wavelength was scanned to find a resonance with a good contrast (panel a of Figure 4.6), then the probe wavelength was set on the half-height point ( $\lambda_{\text{half}} = 1549.888 \text{ nm}$ ) and the scan stopped, obtaining a flat trace representing the experiment baseline. After this preparation, the supercontinuum source was enabled and, at variance with the acquisition procedure of Subsection 4.2.1, the evolution of the MBR signal was followed in real-time by the oscilloscope, without the necessity of a on-the-fly measurement. In particular, to rule out the presence of any dynamics other than the thermal one, the MBR signal was reconstructed through six different acquisitions, with each of them spanning a 200 ms time interval with a 20  $\mu\text{s}$  time resolution. Panel b of Figure 4.6 exemplifies this reconstruction when illuminating the GNRs with the 760 nm line, highlighting each acquisition with a different color. On each of these acquisitions the detuning-transmission conversion based on the resonance fringe fitting was applied (cfr. Equation (3.1)) and therefore the data shown in panel already represent the optical shift induced in the WGM resonance. For comparison, panel b also shows the baselines recorded before enabling the supercontinuum source, keeping the same color code. As in Subsection 4.2.1, different excitation lines were used during the experiment and, in particular, the 680 nm - 1100 nm range was covered with a 20 nm step. For each excitation line, the acquisition followed the procedure exemplified in panel b for the 760 nm line: the time evolution of the MBR signal was

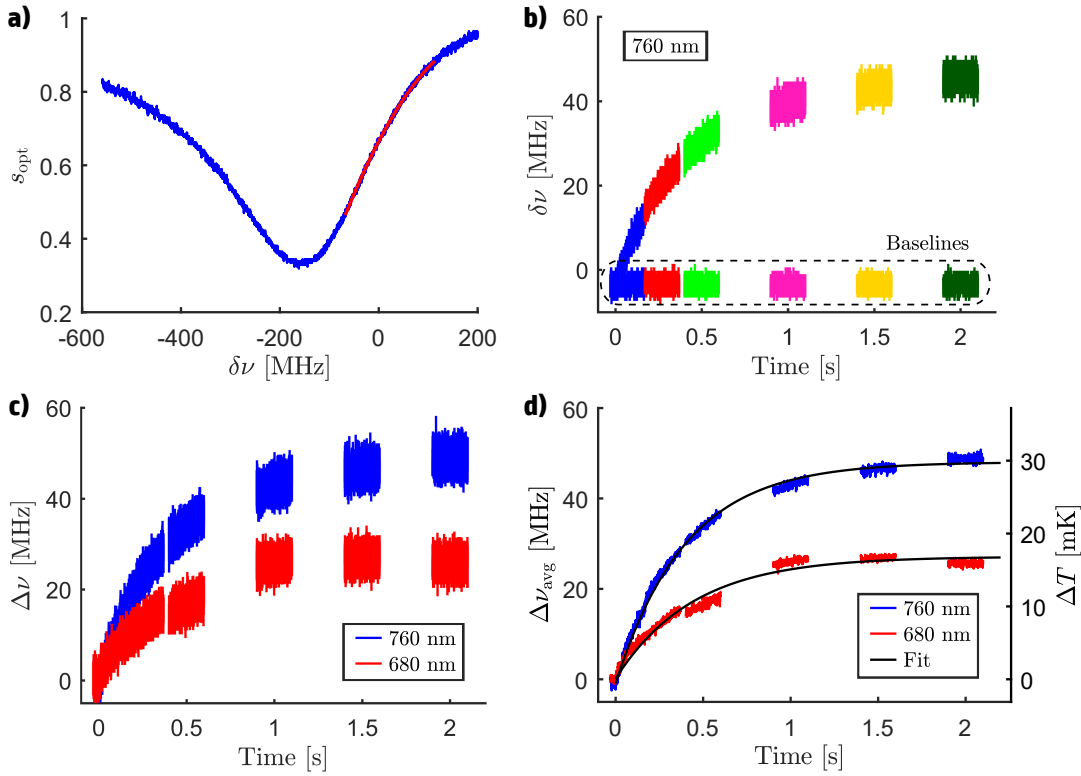


Figure 4.6: Series of panel resuming the signal recorded during the experiment and the data analysis. Panel a: WGM resonance used for sensing the thermal perturbation induced by the nanoparticles absorption (blue curve) along with parabolic fit of the resonance fringe (red curve). Panel b: series of acquisitions reconstructing the evolution of the MBR signal caused by the GNRs heating (top) along with reference baselines (bottom). Panel c: optical shifts caused by the GNRs heating when using the 760 nm excitation line (blue curve) and the 680 nm one (red curve). Panel d: optical shifts after the averaging procedure (red and blue curves, same color code of panel c) and exponential fit based on Equation (4.2) (black curve).

reconstructed with 6 different acquisitions, with baselines recorded each time before enabling the supercontinuum source.

By subtracting the baselines, it was possible to compute the optical shift  $\Delta\nu$  induced by the GNRs absorption for each excitation wavelength and panel c of Figure 4.6 shows as examples the results obtained for the 760 nm line and the 680 nm line. The electric noise from the detector (PD, cfr. panel a of Figure 4.1) and the quantisation of the oscilloscope ADC introduced a significant noise level in these curves, but this could be mitigated by exploiting the time resolution of the acquisition. As previously mentioned, the 20  $\mu$ s resolution was set to check the presence of dynamics in addition to the thermal one and, since no one was present, it ultimately produced an oversampling of the MBR signal. This oversampling allowed to lower noise contribution by grouping data points into 0.5

ms intervals ( $0.5 \text{ ms}/20 \text{ } \mu\text{s} = 25$  points per interval) and averaging them, effectively collapsing 25 data points into one average value. This method produced a significant decrease in the noise level and much smoother profiles ( $\Delta\nu_{\text{avg}}$ ), as shown in panel d of Figure 4.6, which shows the same data set of panel c after the averaging process. The time window employed for the averaging (0.5 ms) was chosen below the evolution time scale of the  $\Delta\nu$  curves ( $\approx 400$  ms) to ensure that the “averaged” and the originals curves had the same trend.

Through Equation (4.1), the optical shifts  $\Delta\nu_{\text{avg}}$  were converted into thermal shifts  $\Delta T$ . For the curves in panel d of Figure 4.6, the results of this conversion are shown through the vertical axis on the right side of the panel. In analogy with the results of Subsection 4.2.1, the order of magnitude of the temperature shifts  $\Delta T$  is tens of millikelvin, but here the time evolution of the temperature is clearly visible. In particular, an exponential function given by

$$\Delta T(t) = \Delta T_{\infty} (1 - \exp(-t/\tau_{\text{thr}})) \quad (4.2)$$

reconstructed faithfully the temperature trend for all the excitation wavelengths used in the experiment: two examples are shown in panel d as black curves. In Equation (4.2) the parameter  $\Delta T_{\infty}$  is the thermal equilibrium temperature or, in other words, the temperature reached when the heat dissipation of the system balances the heat generation from the GNRs absorption. The parameter  $\tau_{\text{thr}}$ , instead, is the time constant defining the transition to thermal equilibrium. By repeating the fitting procedure on the entire dataset, both  $\Delta T_{\infty}$  and  $\tau_{\text{thr}}$  were obtained for each excitation wavelength used in the experiment.

At variance with Chapter 3, no particular frequency composition is expected for the  $\Delta T(t)$  signal, due to the different perturbations produced by the different laser sources. In Chapter 3, in fact, a high-energy laser pulse excites the GNRs and the MBR walls vibrate as a consequence of the PA wave hitting them. Here, instead, the source can be approximated to a CW laser (since it emits low-energy pulses with a high repetition rate) and therefore the MBR walls are uniformly deformed and heated, rather than put into motion. This interpretation is confirmed by the different dynamic of the signals, with the first ones evolving on a microsecond time scale and the second ones evolving on a seconds time scale.

The temperature trend  $\Delta T(t)$  here reported confirms that the preliminary spectra obtained in Subsection 4.2.1 are influenced by heat dissipation. In fact, those measurements were performed using exposure times above 0.5 s: a time window where heat dissipation becomes more and more important and ultimately leads to thermal equilibrium, as shown in panel d of Figure 4.6. The acquisition procedure here described, instead, overcomes this limit by allowing a detailed description of the temperature trend up to time zero, where heat dissipation can be neglected to a first approximation. In particular, as shown in the following, it was possible to deduce the GNRs absorption spectrum from the temperature rate  $R_{\text{trm}}$ , defined as the derivative of  $\Delta T(t)$  at time zero.

Using the definition of  $\Delta T(t)$  given in Equation (4.2), the temperature rate  $R_{\text{trm}}$  is



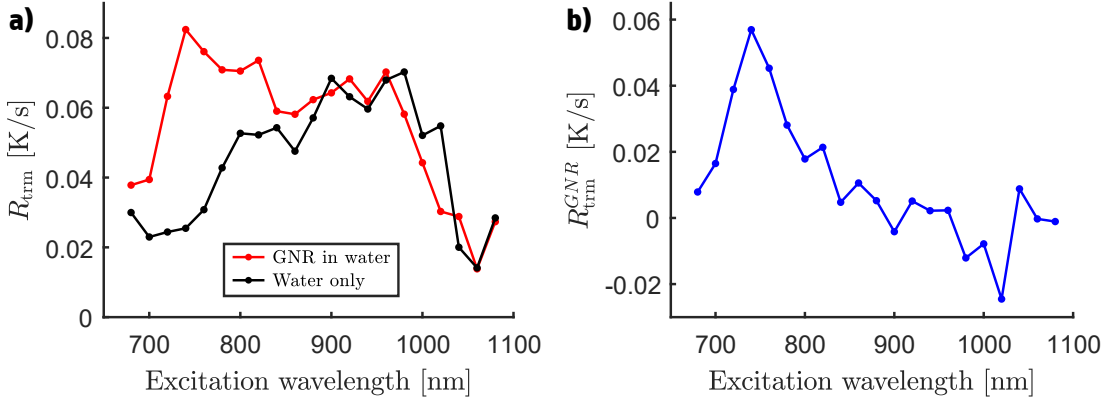


Figure 4.7: Panel a shows the temperature rate  $R_{\text{trm}}$  measured when the MBR was filled with the GNRs colloidal solution (red curve) and when it was filled with plain water (black curve). The difference of these curves is shown in panel b (blue curve).

formally given by

$$R_{\text{trm}} = \left. \frac{d\Delta T}{dt} \right|_{t=0} = \frac{\Delta T_{\infty}}{\tau_{\text{thr}}} \quad (4.3)$$

and could be computed through the  $\Delta T_{\infty}$  and  $\tau_{\text{thr}}$  estimates deduced from the temperature trend fitting. Panel a of Figure 4.7 shows as the red curve the  $R_{\text{trm}}$  resulting from the dataset discussed up to this point, obtained with the MBR filled with the GNRs colloidal solution. In addition, panel a also shows as the black curve the  $R_{\text{trm}}$  obtained with the MBR filled with plain water. The two curves differ significantly below 900 nm, but become almost indistinguishable above this wavelength. This difference can be explained by considering the increase of water absorption for increasing wavelength in the visible and infrared regions [137]. In practice, below the 900 nm threshold, water is sufficiently transparent to contribute residually to the temperature increase of the system and therefore the temperature trend is guided almost entirely by the GNRs absorption. Above 900 nm, instead, water absorption increases and this makes the system totally driven by water absorption rather than GNRs absorption. By subtracting the temperature rates  $R_{\text{trm}}$  obtained in the two configurations, it was then possible to obtain the GNRs contribution to the system temperature increase

$$R_{\text{trm}}^{\text{GNR}} = \left( \frac{\Delta T_{\infty}}{\tau_{\text{thr}}} \right)_{\text{solu}} - \left( \frac{\Delta T_{\infty}}{\tau_{\text{thr}}} \right)_{\text{host}} \quad (4.4)$$

which is shown in panel b of Figure 4.7.

Finally, the nanoparticles absorption coefficient  $\mu$  could be computed from the thermal rate  $R_{\text{trm}}^{\text{GNR}}$  by implementing a simple thermal model here described. Considering an infinitesimal time interval  $\delta t$  immediately after laser emission, the energy impinging on the MBR is given by  $\delta E_{\text{opt}} = P_{\text{opt}} \delta t$ , with  $P_{\text{opt}}$  being the optical power of the beam focused on the MBR. Only a fraction of the impinging energy is absorbed by the nanoparticles and, through the nanoparticles absorption coefficient  $\mu$ , this energy can

be quantified as

$$\delta E_{\text{abs}} = \delta E_{\text{opt}} \int_0^{2R} \mu \exp(-\mu z) dz = P_{\text{opt}} (1 - e^{-2\mu R}) \delta t \quad , \quad (4.5)$$

where  $R$  is the MBR radius. By introducing the system heat capacity  $\mathcal{C}$ ,  $\delta E_{\text{abs}}$  allows to compute the temperature increase  $\delta T$ . In particular, since the nanoparticles represent a tiny fraction of the solution volume and the micro-metric MBR walls have a minute mass with respect to the solution mass, the heat capacity of the system  $\mathcal{C}$  can be approximated to the one of a water. With this approximations, the expression for  $\delta T$  becomes

$$\delta T = \frac{\delta E_{\text{abs}}}{\mathcal{C}} = \frac{P_{\text{opt}} (1 - e^{-2\mu R})}{c_{\text{wat}} \rho_{\text{wat}} V_{\text{MBR}}} \delta t \quad (4.6)$$

where  $c_{\text{wat}}$  is water specific heat capacity,  $\rho_{\text{wat}}$  is water mass density,  $V_{\text{MBR}} = 4/3 \pi R^3$  is the MBR volume and the expression for  $\delta E_{\text{abs}}$  is taken from Equation (4.5). By dividing both sides of Equation (4.6) for  $\delta t$ , the temperature rate  $\delta T/\delta t$  is introduced explicitly in the model

$$\frac{\delta T}{\delta t} = \frac{P_{\text{opt}} (1 - e^{-2\mu R})}{c_{\text{wat}} \rho_{\text{wat}} V_{\text{MBR}}} \quad (4.7)$$

and, using standard analytical passages, Equation (4.7) can be inverted to obtain the expression for the the absorption coefficient  $\mu$

$$\mu = - \frac{\ln \left( 1 - \frac{\delta T}{\delta t} \frac{c_{\text{wat}} \rho_{\text{wat}} V_{\text{MBR}}}{P_{\text{opt}}} \right)}{2R} \quad . \quad (4.8)$$

In this model heat dissipation is neglected since the description focuses on the first instants after laser emission, where, to a first approximation, evolution is only driven by absorption.

Since the impinging optical power  $P_{\text{opt}}$  was measured during the setup preparation (cfr. inset of Figure 4.3), the thermal rate  $\delta T/\delta t$  was estimated through  $R_{\text{trm}}^{\text{GNR}}$  and the remaining quantities could be evaluated from the MBR radius (200  $\mu\text{m}$ ) or represented tabulated coefficients, it was possible to compute the absorption coefficient  $\mu$  from Equation (4.8). Regarding this computation, it is important to highlight that only the values of  $R_{\text{trm}}^{\text{GNR}}$  up to 900 nm were considered to avoid water absorption superseding nanoparticles absorption.

The resulting absorption coefficient  $\mu$  is shown as a blue curve in Figure 4.8 after the rescaling to a base 10 logarithm through  $\mu_{[10]} = \log_{10} e \cdot \mu_{[e]}$ . In this curve, the dots represent the computed values, while the straight lines connecting them are a guide to the eye. Since each point corresponds to an excitation wavelength, the sampling of this curve can be increased by testing more excitation wavelengths during the experiment. For comparison, Figure 4.8 also shows as a pink curve the absorption coefficient (in base 10) measured by a spectrophotometer using a solution with a 0.4 mM Au concentration.

Despite some differences, the two curves share the same general trend, proving that the MBR allows a qualitative measurement of the nanoparticles absorption spectrum.

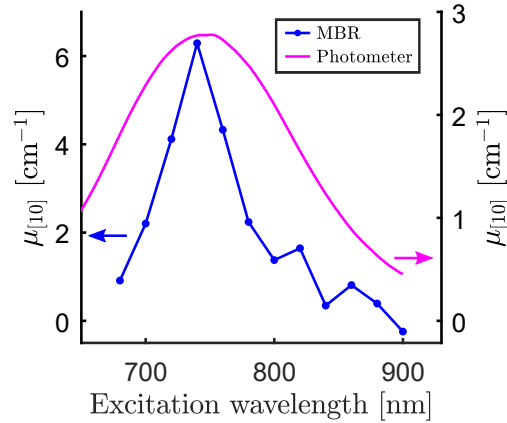


Figure 4.8: Comparison of the nanoparticles absorption coefficient as measured through the MBR (blue curve) and through a spectrophotometer (pink curve). For this plot the  $\mu$  coefficient obtained from Equation (4.8) is scaled to a base 10 logarithm in analogy with the values given by spectrophotometer.

At the moment, these differences, which concern the full-width half-maximum of the curves (60 nm vs. 170 nm) and their peak value ( $6.3 \text{ cm}^{-1}$  vs.  $2.8 \text{ cm}^{-1}$ ), are attributed to inhomogeneities in particles batches and the different Au concentrations. Indeed, further investigation is necessary to test this interpretation (for example, by repeating the experiment with a series of more and more diluted solutions) and the system needs refinement before being implemented for an application. However, the results of this initial proof-of-concept experiment point in the right direction and are promising for further development.

In prospective, an MBR system would allow to measure nanoparticles absorption without relying on optical extinction, but rather through a thermal process. This possibility is advantageous since the light extinction spectrum is a combination of both the absorption spectrum and the scattering spectrum, while a thermal process, such as the temperature increase, is only dictated by the first. In the case of small nanoparticles in a clear host environment, a light extinction measurement is indeed a good estimate for particles absorption, due to the small scattering contribution. However, this same measurement would become difficult in the case of big particles (i.e. particles with scattering cross section close to absorption cross section) or opaque host environments, since scattering contribution could overtake and hide the absorption contribution. An MBR system, instead, would not suffer from these problems due to its temperature-based measurement, which is sensitive only towards absorption and totally insensitive towards scattering, both from the particles and the environment. Since biological fluids can both be opaque and host highly-scattering particles, the MBR appears interesting for their absorption analysis.

### 4.3 Conclusions

In this Chapter the absorption spectrum of nanoparticles was deduced through the temperature shift induced in an MBR, effectively implementing the resonator as a thermo-optical sensor. In analogy with the PA study presented in Chapter 3, the MBR took the double role of sensor and vial, allowing to interrogate an extremely small sample (below 40 nl), to perform the optical detection of the temperature shift and achieve an all-optical configuration. The absorption spectrum resulting from the MBR measurements was compared with the one obtained with a spectrophotometer, finding a compatible trend.

The differences between the two spectra, however, are noteworthy and will be the subject of further studies. A first example in this direction, could be the revision of the simple thermal modelling linking the measurable quantities to the absorption coefficient  $\mu$  through the development of a detailed thermal simulation of the system, in analogy with FEM model of Subsection 3.2.3. Indeed, to obtain a quantitative and robust estimate of the nanoparticles absorption spectrum, refinements have to be made, but this proof-of-concept experiment represents a good starting point. In prospective, the MBR system represents a promising device for the measurement of the absorption spectrum of opaque biological samples or high-scattering nanoparticles suspensions.

## Chapter 5

# Light collection from single-photon sources

This Chapter presents a feasibility study about the implementation of a microbubble resonator (MBR) as a micro-cavity for the collection of light generated by single-photon sources (SPS). At variance with Chapter 3 and 4, this Chapter is of theoretical/computational nature and represents a preliminary benchmark before the actual implementation of the system. The goal of the Chapter is to quantify the potential of the MBR by computing a series of figures-of-merit, using the results of Chapter 2 as foundations. The single-photon sources selected for this study are dibenzoterrylene (DBT) molecules, which are known to be efficient quantum emitters that are already under study for the implementation in photonic devices.

The Chapter starts with a brief resume of the properties the DBT molecules (Section 5.1), moves to the description of the envisaged experimental configuration (Section 5.2) and then describes the computation of the figures-of-merit (Section 5.3).

### 5.1 Dibenzoterrylene molecules

The single-photon sources chosen for the MBR implementation here presented are dibenzoterrylene (DBT) molecules embedded in an anthracene (Ac) matrix. These molecules, which belong to the family of polycyclic aromatic hydrocarbons (PAH), are known and reliable quantum emitters, and are promising sources for the implementation into photonics structures [121, 106, 101, 138].

The promising features of this SPS rely on both the intrinsic properties of the DBT molecule, which is the actual chromophore, and its seamless integration into the anthracene matrix, which follows from the analogies between the chemical structure of the two molecules. In particular, DBT molecules in anthracene (DBT:Ac) feature an almost unitary quantum efficiency, do not present multi-photon emission and are very stable under continuous illumination, since the Ac matrix negates photochemical reactions between DBTs and oxygen. In terms of crystallography, the DBTs insert in a specific spot of the anthracene crystal and this produces an high reproducibility of the SPS. In

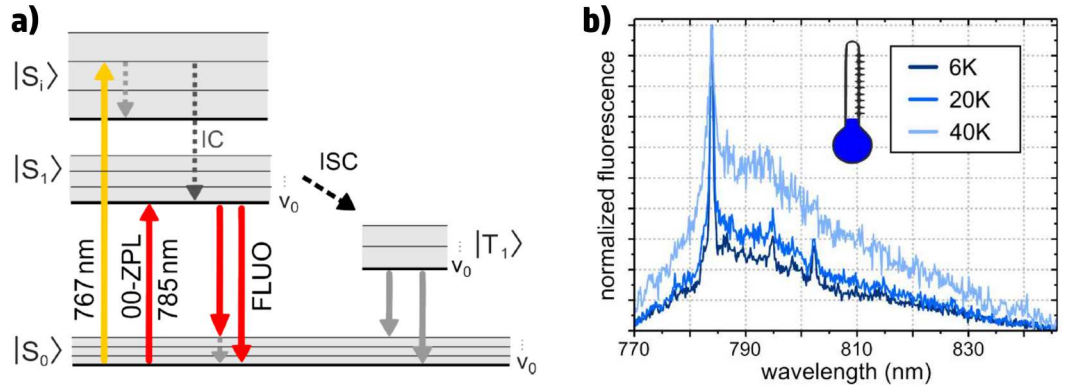


Figure 5.1: Panel a: level scheme (or Jablonski diagram) of DBT molecules embedded in anthracene matrix highlighting with ascending arrows the two transitions used to pump the system, and with descending arrows the de-excitation transitions associated with the targeted fluorescence (adapted from [138]). Panel b: fluorescence spectrum of the DBTs for different cryogenic temperatures (adapted from [138]).

addition, this positioning produces a specific orientation of the DBT emission dipole, allowing to design photonic structure optimized for this orientation. Finally, the production of the DBT:Ac sources can be implemented using standard chemical equipment and it is cost-effective: an interesting combination when compared with other SPS which need dedicated systems for their production and handling (e.g. optical traps for atoms and ions, semiconductor epitaxy systems for quantum dots).

Panel a of Figure 5.1 shows the level scheme (or Jablonski diagram) of the DBT molecules embedded in the Ac matrix, focusing on the first electronic levels ( $|S_0\rangle$ ,  $|S_1\rangle$ ,  $|T_1\rangle$ ) and their associated vibrational levels (shown as grey bands). In this Figure, the ascending arrows highlight the two transitions used to pump the system (767 nm for room temperature experiments and 785 nm for cryogenic experiments), while the descending arrows highlight the de-excitation transitions associated with the targeted fluorescence. In particular, the targeted fluorescence is the one associated with the transition between the ground vibrational level of  $|S_1\rangle$  with the ground vibrational level of  $|S_0\rangle$ . The fluorescence spectrum of this transition (called zero-phonon line, ZPL) is shown in panel b of Figure 5.1 for a series of cryogenic temperatures. The ZPL is centred at 785 nm ( $\lambda_{zpl} = 785$  nm), has a width  $\gamma = 50$  MHz and a lifetime  $T_1 = 1/\gamma = 20$  ns. The secondary peaks at longer wavelengths, instead, are associated with transition towards the excited vibrational levels in the  $|S_0\rangle$ .

At cryogenic temperatures, the Ac crystal does not show significant phononic vibrations, but this condition changes rapidly with increasing temperature and affects the emission of the DBTs. In particular, at room temperature, the photons wavepackets produced by the ZPL are influenced by the matrix phonons and therefore show less indistinguishability. This effect is called dephasing and can be quantified with the pure dephasing rate  $\gamma^*$  or equivalently with the pure dephasing time  $T_2^* = 1/\gamma^*$ . Both quantities take the “pure” adjective to avoid misunderstanding with the overall dephasing

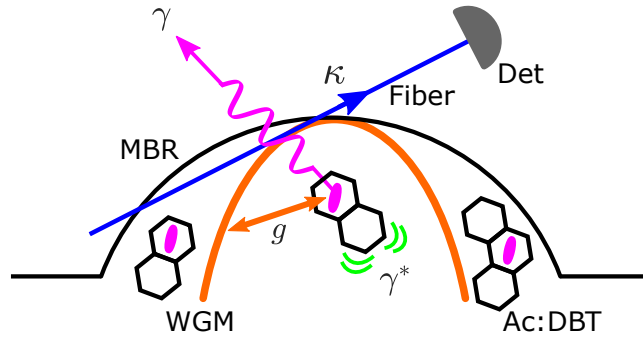


Figure 5.2: Sketch of the experiment aimed at the collection of light from single-photon sources through a microbubble resonator. An MBR is coupled to a tapered fiber (in blue) and is filled with an anthracene matrix (hexagons) containing DBT molecules (purple dots). The WGM coupled to the fiber is highlighted in orange and is also coupled to the DBT molecules. The decay rate  $\gamma$ , the pure dephasing rate  $\gamma^*$ , the cavity loss rate  $\kappa$  and the cavity-emitter coupling rate  $g$  are conceptually visualised with straight or weavy lines.

rate  $\gamma_{\text{deph}} = \gamma/2 + \gamma^*$ , which is defined in analogy with nuclear magnetic resonance. For room temperature configurations,  $\gamma^*$  exceeds  $\gamma$  by orders of magnitudes and therefore dictates the value of  $\gamma_{\text{deph}}$ . For cryogenic configurations, instead, the reverse is true since  $\gamma^*$  is approximately null.

## 5.2 The microbubble implementation

The envisaged MBR implementation for the collection of light from the DBT molecules in the anthracene matrix is shown in Figure 5.2. In this configuration an MBR is filled with an anthracene matrix (represented by hexagons in Figure 5.2) containing the DBT molecules (purple dots) and is coupled to a tapered fiber as in Chapters 3 and 4. The WGM coupled to the fiber is highlighted with an orange ring in this sketch and, due to the uniform distribution of the DBTs in the MBR volume, some molecules are bound to be located within its internal evanescent tail. This causes the WGM to be coupled to both the fiber and the DBT molecules, leading to a configuration analogous to one of quantum emitters in a photonic crystal micro-cavity [28, 115, 117, 114, 113, 111]. In analogy with such cavities, the WGM acts as the cavity mode to enhance the source emission and the light matter-interaction, while the fiber mode acts as the leakage mode that allows light extraction. In particular, since the fiber mode is a guiding mode this configuration is optimal for the detection of the emitted photon or its injection in another optical system (e.g. Hong-Ou-Mandel interferometer). To simplify the discussion and the computations of this Chapter, only one DBT molecule is assumed to be coupled to the WGM. However, by adjusting the DBTs concentration in the Ac matrix, it is possible for more molecules to interact with the same WGM, therefore making the MBR an interesting platform for the study of multiple-emitters effects.

As shown conceptually in Figure 5.2, the experimental configuration is described by four parameters. The first two parameters  $\gamma$  and  $\gamma^*$  have the same meaning of Section 5.1, and therefore represent the decay rate from the excited state  $|S_1\rangle$  and the pure dephasing rate, respectively. Since the only the transition here considered is the ZPL, the decay rate  $\gamma$  can be regarded as a fixed constant:  $\gamma = 50$  MHz. The dephasing rate  $\gamma^*$ , instead, takes values over a wide range, since the computations in Section 5.3 aim to simulate a room temperature regime. The third parameter describing the experimental setup is the cavity loss rate  $\kappa$  accounting for the photon probability to escape the WGM and move into the fiber mode. Since the escape probability per round-trip is given by the square of the fiber-WGM coupling coefficient, the cavity loss rate  $\kappa$  can be computed as [54, 54]

$$\kappa = |\kappa_{\text{ovrl}}|^2 \cdot \text{FSR} = |\kappa_{\text{ovrl}}|^2 \cdot \frac{c}{2\pi R_e n_e} \quad (5.1)$$

where  $\kappa_{\text{ovrl}}$  is the fiber-WGM coupling coefficient estimated by the overlap between the two modes (cfr. Section 2.5) and FSR is the MBR free spectral range. As shown in the following, this parameter influences strongly the value of  $\beta$ . Finally, the cavity-emitter coupling rate  $g$  represents the strength of the interaction between the WGM and the DBT molecule. This parameter follows from the Jaynes-Cummings model [139, 97, 140, 141] describing the light-matter interaction in an optical cavity using a quantisation scheme for both matter and field. The results of Chapter 2 are fundamental to compute this quantity, since  $g$  depends both on the cavity modal volume (Section 2.6) and the energy density distribution (Section 2.4.3). A detailed discussion on the computation of  $g$  is given in Subsection 5.3.1.

To assess the performance of the MBR configurations in terms of light collection, the main parameters here analysed are the photon indistinguishability  $I$  and the fiber mode collection efficiency  $\beta$ . In addition, to compare the performance of the MBR configuration with the no-cavity (i.e. free-space) configuration, a funnelling ratio  $\mathcal{F}$  combining both indistinguishability  $I$  and efficiency  $\beta$  is considered. As shown in [142], which considers a general case of cavity-emitter interactions, the indistinguishability  $I$  and the efficiency  $\beta$  can be computed using the second quantisation formalism and, in the case of high-quality cavities (i.e. good cavity regime), both figures-of-merit have a closed analytical expression. In particular, these expressions are deduced for a regime of high dephasing (i.e.  $\gamma^* \gg \gamma$ ), which allows to deduce the performance of the system for a room temperature regime. In the end, these expressions are [142]:

$$R = \frac{4g_0^2}{\kappa + \gamma + \gamma^*} \quad (5.2)$$

$$I = \frac{\gamma + \frac{\kappa R}{\kappa + R}}{\gamma + \kappa + 2R} \quad (5.3)$$

$$\beta = \frac{\kappa R}{\kappa R + \gamma(\kappa + R)} \quad (5.4)$$

$$\mathcal{F} = \frac{\gamma^*}{\gamma} \beta I \quad (5.5)$$



and depend from the experiment parameters previously introduced. The auxiliary parameter  $R$  in Equation (5.2) allows to have more compact expressions and can be interpreted as the photon reabsorption rate between the DBT molecule and the WGM.

In the following Section, the performance of the MBR system are assessed by computing these figures-of-merit while scanning the experiment parameters and using the results of Chapter 2 to evaluate the coupling between the DBT molecule and the WGM.

### 5.3 Evaluating system performance

This Section begins with the computation of the coupling parameter  $g$  based on the results of Chapter 2 (Subsection 5.3.1), then moves to the computation of the figures-of-merit shown in Equations (5.3)-(5.5) to assess the system performance (Subsection 5.3.2).

#### 5.3.1 Coupling to a DBT molecule

The general expression for the coupling parameter  $g(\mathbf{r})$  between an optical cavity mode and a quantum emitter is given by the Jaynes-Cummings model discussed in [139, 97, 140, 141, 143]:

$$g(\mathbf{r}) = \sqrt{\frac{\pi c}{\hbar \epsilon_0} \frac{\mu^2}{\lambda_{\text{tr}} \mathcal{V}}} U(\mathbf{r}) = g_0 U(\mathbf{r}). \quad (5.6)$$

In this general expression  $\lambda_{\text{tr}}$  is the vacuum wavelength of the transition under study,  $\mu$  is its associated dipole moment,  $\mathcal{V}$  is the volume of the cavity mode and  $U(\mathbf{r})$  is the normalized cavity mode distribution. For the system here considered, the transition under study is the ZPL, therefore  $\mu = 8.03$  Debye and  $\lambda_{\text{tr}} = 785$  nm, while  $\mathcal{V}$  and  $U(\mathbf{r})$  have to be deduced from the MBR mode coupled to the DBT molecules through the methods of Section 2.4 and Section 2.6.

To mimic the experimental configuration of Figure 5.2, the MBR considered for these computations has an anthracene core ( $n_c = 1.6$ ), silica walls ( $n_w = 1.45$ ) and air as the external medium ( $n_e = 1$ ). However, this dielectric configuration produced rounding errors in the evaluation of Equations (A.53)-(A.55), due to the high value of the Bessel functions produced by the anthracene index and the typical MBR radii (around 200  $\mu\text{m}$ ). As a consequence, the  $F(kr)$  did not follow the boundary conditions at the dielectric interfaces. This computational problem was avoided by switching to a microsphere configuration (anthracene sphere in silica environment) and simplifying Equations (A.53)-(A.55) in analogy with [124, 123]. As shown in the following, the microsphere configuration represents a good approximations of the experimental configuration since the WGM has little leakage in the surrounding medium due to the high value of the anthracene index.

To consider the easiest geometry, the WGM assumed to be coupled to the DBT molecule is the fundamental one ( $n = 1$ ,  $m = \ell$ ) having its resonance wavelength  $\lambda_0$  closest to the ZPL. In panel a of Figure 5.3, the volume of this mode (computed as

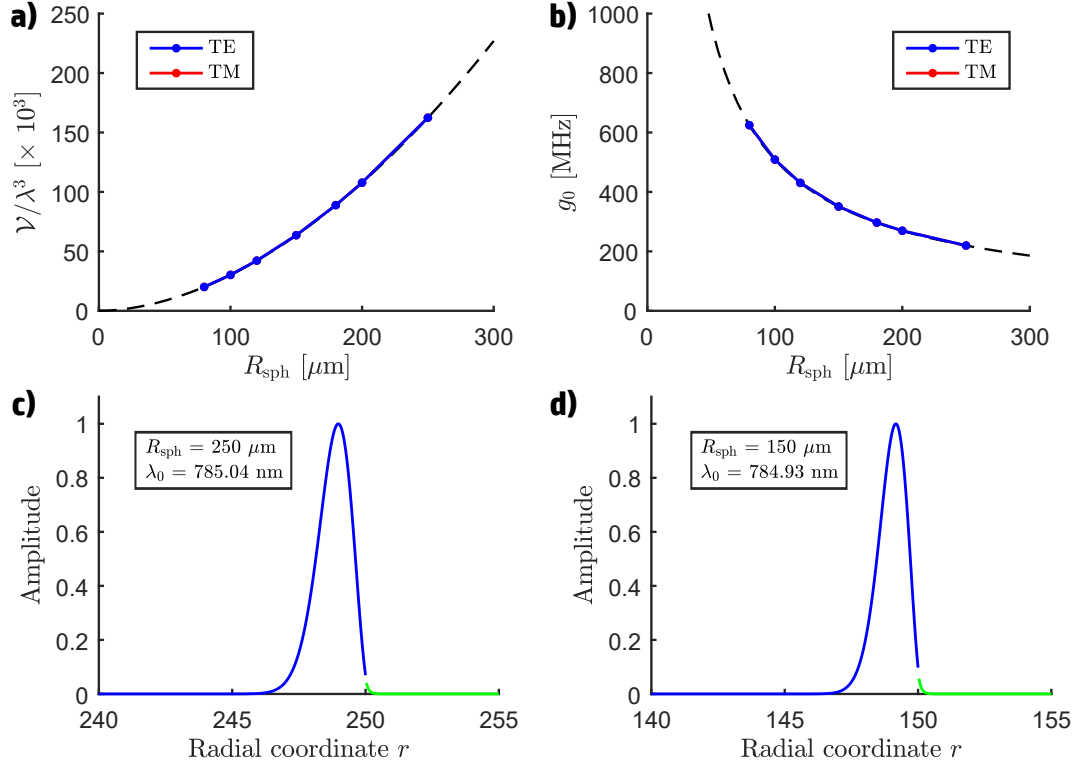


Figure 5.3: Series of panels resuming the computation of the WGM-DBT coupling. Panel a) shows the modal volume of the fundamental WGM coupled to the DBT molecule for different choices of the anthracene microsphere radius. Panel b) shows the associated  $g_0$  values, while panel c) and d) show the  $U(\mathbf{r})$  function for the  $R_{\text{sph}} = 250 \mu\text{m}$  case and the  $R_{\text{sph}} = 150 \mu\text{m}$  case respectively.

in Section 2.6) is reported for different anthracene microspheres (radius:  $R_{\text{sph}}$ ) to reconstruct the  $\mathcal{V}$  trend against the resonator size. In particular, the values of  $\mathcal{V}$  shown in the plot are normalized to the cube of the anthracene wavelength  $\lambda_{\text{mat}} = \lambda_0/n_c$ , in analogy with the conventions in use for the photonic crystal micro-cavities, and the  $R_{\text{sph}}$  values are chosen to represent possible MBR radii. Both TE and TM possibilities are considered and their equivalence is confirmed by the superposition of the two curves, in analogy with Figure 2.10.

As expected, the modal volume increases with increasing size of the resonator, but no straightforward functional trend can be recognized. As a preliminary analysis, the curve is fitted with a power-law (black dashed line,  $\mathcal{V} = V_0 (R_{\text{sph}})^\alpha$ ,  $\alpha = 6.44$ ) finding good agreement.

Using the  $\mathcal{V}$  values shown in panel a) of Figure 5.3, it is then possible to compute the WGM-DBT coupling coefficient  $g_0$  by applying directly Equation (5.6). The resulting  $g_0$  values are shown in panel b) and represent a promising prospective for the experiment. In fact, since the  $g_0$  values are significantly higher than the decay rate  $\gamma$  of the ZPL ( $\gamma = 50 \text{ MHz}$ ) and of the cavity loss rates  $\kappa$  (assuming  $|\kappa_{\text{ovrl}}|^2 = 10^{-6}$ ,  $\kappa$  falls between

10 kHz and 40 kHz for the considered geometries), they allow a strong coupling regime between the WGM and the DBT molecule in a cryogenic configuration. As discussed in Subsection 5.3.2, these values are also promising for a high dephasing regime (i.e. room temperature) since they lead to a high photon indistinguishability even in this case.

Finally, panel c and d show the profile of the  $U(\mathbf{r})$  function appearing in Equation (5.6) in the  $R_{\text{sph}} = 250 \mu\text{m}$  case and the  $R_{\text{sph}} = 150 \mu\text{m}$  case respectively. This profile is directly given by the normalized energy density  $u_{\text{norm}}$  of Section 2.4.3, which is here plotted assuming  $\theta = \pi/2$  (i.e. equator plane) and leaving  $r$  as the running variable. The function shows a strong localisation of the WGM in the anthracene sphere, with little evanescent tails in the silica environment. As previously mentioned, this justifies the microsphere approximation used for the computation of the modal volume, since an even lesser leakage is expected in the air layer of the MBR. In addition, the  $U(r)$  profiles also show that the optimal spot for the DBT molecule is one micrometer away from the MBR wall surface (with a  $\pm 0.6 \mu\text{m}$  tolerance given by the profile FWHM) and that the MBR silica walls should have a thickness below one micrometer to achieve an efficient fiber coupling.

### 5.3.2 Light collection figures-of-merit

From the results of the previous Subsection, it is finally possible to predict the performance of the system by computing the figures-of-merit indistinguishability  $I$ , efficiency  $\beta$  and funnelling ratio  $\mathcal{F}$  shown Equations (5.3)-(5.5) for different experimental configurations.

A first series of plots reporting the  $I$ ,  $\beta$  and  $\mathcal{F}$  trends against the normalized dephasing rate  $\gamma^*/\gamma$  is shown in panels a-c of Figure 5.4. In each of these panels, multiple curves are reported to compare the trends produced by resonators of different sizes, in analogy with panel a and b of Figure 5.3. For these plots the cavity loss  $\kappa$  is computed through Equation (5.1) assuming  $|\kappa_{\text{ovrl}}|^2 = 10^{-6}$ , in analogy with the experimental values given by cavity ringdown spectroscopy (cfr. Subsection 1.2, [54, 55]), and the FSR is adjusted for each curve to account for the different resonator size. For the cases here considered, the resulting  $\kappa$  values fall between 10 kHz and 40 kHz.

Starting from panel a, one notices that the indistinguishability  $I$  rapidly reaches values close to 1, with resonator size only slightly influencing this trend. From an experimental point of view, this suggests that high dephasing do not hinder the single-photon emission of the system, therefore allowing a room temperature operability. Following the interpretation in [142], this response follows from the relationships between the various rates. In particular, since both the cavity loss rate and reabsorption rate  $R$  are below the decay rate ( $\kappa < \gamma$ ,  $R < \gamma$ ), the photon can stay for long time in the cavity without being recombined with the emitter and therefore avoiding the dephasing effect.

Moving to panel b, one finds a substantially flat efficiency  $\beta$ , with a more important effect of the resonator size due to the direct correlation between the cavity loss  $\kappa$  and the resonator FSR (cfr. Equation (5.1)). In particular, the flat trend can be explained by the low  $\kappa$  value, which strongly reduces the effects of  $\gamma^*$  in Equation (5.4), but also lowers  $\beta$  in the  $10^{-3}$  order. As shown in the following (cfr. panel e), the efficiency  $\beta$

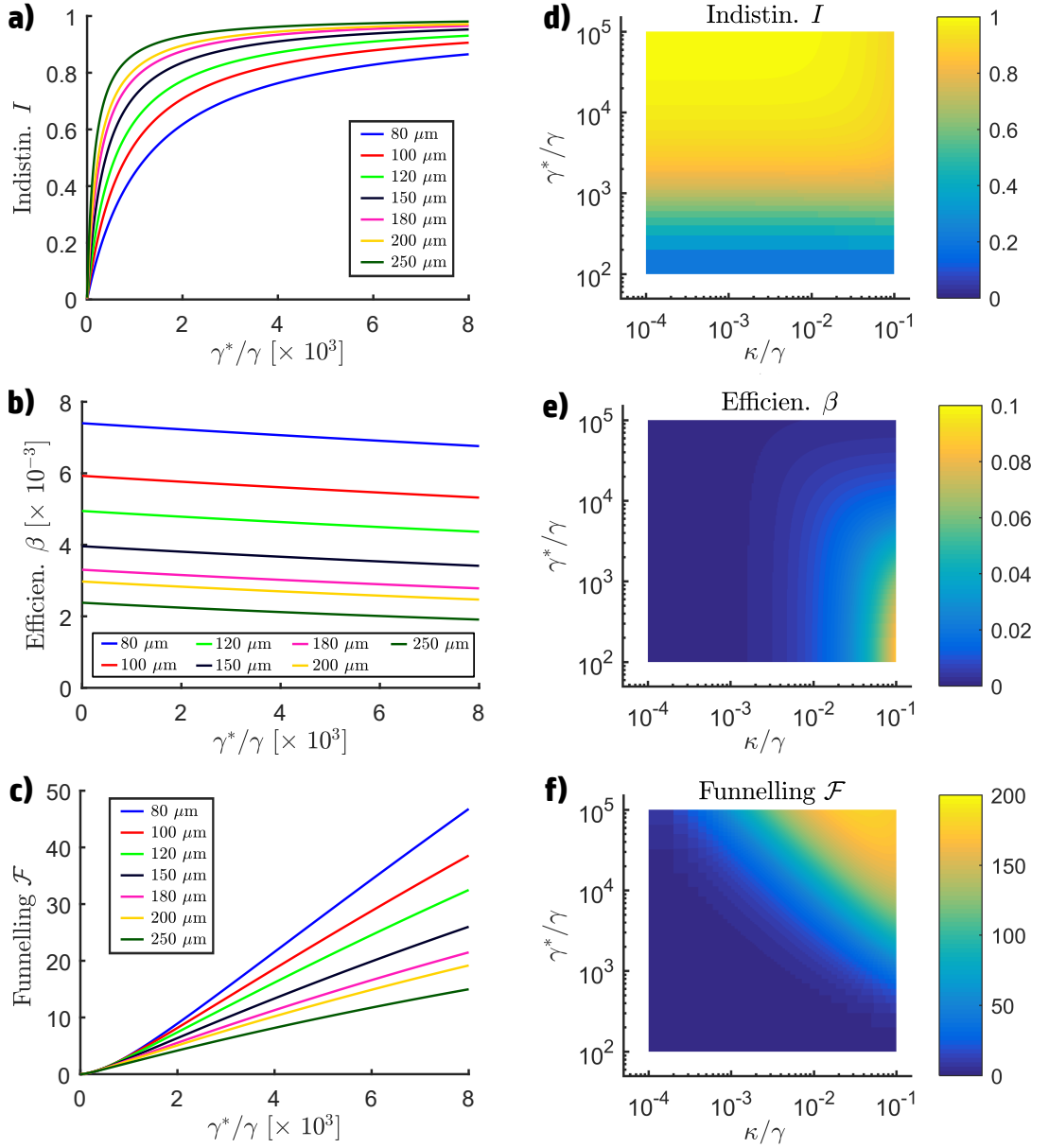


Figure 5.4: Series of plot showing the single-photon emission figures of merit indistinguishability  $I$ , efficiency  $\beta$  and funnelling ratio  $\mathcal{F}$ . The panels on the left side (a-c) features different curves to highlight the differences between resonators of different size. The panels on the right side (d-f), instead, show highlight the dependency on the cavity loss rate  $\kappa$ .

shows a significant dependency on the cavity loss  $\kappa$  and the experiment would benefit from increased  $\kappa$  (i.e. increased fiber coupling losses).

Finally, panel c shows the trend of the funnelling ratio  $\mathcal{F}$ , which quantifies the improvement produced by the cavity presence considering both the indistinguishability  $I$  and the efficiency  $\beta$ . These curves clearly shows the effectiveness of the WGM-DBT coupling due to their value well above 1 (i.e equivalence threshold between the cavity and the free-space cases) and their rising trend, which predicts higher improvements for higher dephasing. This results is also robust with respect to the resonator size, since the different curves in panel c are weakly affected by this parameter.

In addition, to also test the effects of different cavity loss rates  $\kappa$ , a second series of plots is reported in panels d-f of Figure 5.4. For these plots both the  $\gamma^*$  and the  $\kappa$  variables are scanned (y-axis and x-axis, respectively), while the microsphere radius is fixed to the  $R_{\text{sph}} = 150 \text{ }\mu\text{m}$  case. The scan on these parameters covers some order of magnitude to simulate a wide range of experimental conditions.

Starting from panel d, one notices that indistinguishability  $I$  is almost independent from the cavity loss rate  $\kappa$ , with a slight increase for lesser  $\kappa$  only noticeable at top-left corner of the panel. Regarding the dephasing  $\gamma^*$ , instead, one finds the same trend of panel a, with a quick rise to values close to 1.

Moving to panel e and considering the efficiency  $\beta$ , the dependency on the cavity loss  $\kappa$  becomes apparent. In particular, the  $\beta$  value closely mimics the  $\kappa/\gamma$  value in the bottom part of the plot, as shown by a close inspection of the colorbar. When moving towards higher dephasing rate, however, the  $\beta$  value suffers a steady decrease, in analogy with panel b. From a mathematical point of view, this trend is expected given the  $\beta$  expression in Equation (5.4), but it also follows from a simple physical consideration: the cavity loss  $\kappa$  sets the photon probability to escape the WGM and move to the fiber mode, which ultimately leads to the photon collection.

Finally, panel f shows that even the funnelling ratio  $\mathcal{F}$  depends on the cavity loss rate  $\kappa$ , with an increasing  $\mathcal{F}$  value for increasing  $\kappa$ . When combining this trend with the one shown in panel c for the dephasing rate  $\gamma^*$ , one obtains a steady increase of  $\mathcal{F}$  when moving along the diagonal moving from bottom-left to top-right. In particular, this trend confirms that the system is capable of high dephasing operability (as also shown in panel c) and that an increase in cavity leakage would benefit the overall performance.

In conclusion, the computations performed in this Subsection show that the proposed experimental configuration (cfr. Figure 5.2) is promising for the control of the DBT molecule emission and the generation of indistinguishable single-photons even in a high dephasing condition (i.e. room temperature). In particular, the system is predicted to be robust against variations in the MBR size, represents a strong improvement with respect to free-space configuration and would benefit from an increased coupling with the collection fiber [117].

## 5.4 Conclusions

In this Chapter, a feasibility study on the implementation of an MBR as a micro-cavity for the collection of light from single-photon source has been presented. The quantum emitters considered for this study are DBT molecules embedded in an anthracene matrix (DBT:Ac), which are known and efficient quantum emitters under investigation for the implementation into photonic devices. At variance with the previous ones, this Chapter has a theoretical/computational approach and evaluates the performance of the proposed configurations through a series of figures-of-merit.

The results of these computations indicate that the MBR offers the possibility to reach a strong coupling regime in a cryogenic configuration, but also that the room temperature operability is interesting. In particular, the photon indistinguishability  $I$  remains high even in this regime and the cavity represents a strong improvement from the bare (i.e. free-space) configuration, as shown with the high funnelling ratio  $\mathcal{F}$ . The computations also show that the system is predicted to be robust against variations in the MBR size and would benefit from an increased coupling between the WGM and fiber to increase the collection efficiency  $\beta$ .

In the end, this study represents a preliminary benchmark for the MBR system, which gives a promising outlook on the realisation of this experiment.

## Chapter 6

# Conclusions and outlook

In this thesis work a Whispering Gallery mode (WGM) MicroBubble Resonator (MBR) has been investigated as an optical sensor for the characterisation of a photoacoustic (PA) contrast agents and as a micro-cavity for the collections of light from single-photon sources (SPS).

Regarding the first matter of investigation, the thesis focused on two proof-of-concept experiments implementing the MBR as an optical sensor for the characterisation of PA contrast agents. In the first experiment, the MBR was implemented as an ultra-compact all-optical PA transducer capable of reconstructing the contrast agent photostability. In the presented configuration the MBR played the double role of sensor and vial containing the contrast agent, producing a setup much smaller than the one used with standard ultrasound detector, and allowing to test liquid samples below 100 nl. The performance of the system were tested in a static configuration and in a flow-cytometry configuration, proving in both cases the feasibility of the measurement. The MBR mechanical modes proved to be key in the sensing mechanism and, in particular, they allowed to increase significantly the signal-to-noise ratio in the flow-cytometry configuration by reducing environmental noise. In prospective, the miniaturisation of the MBR is expected to increase its sensitivity and the mechanical spectrum could be exploited to further increase sensitivity through positive interference or lock-in amplification. In terms of possible applications, in addition to the development of new PA contrast agents, the system could be implemented in portable or on-chip devices aimed at the analysis of flowing samples (e.g. the measurement of blood cells oxygenation or the detection of venous thrombi and/or circulating tumour cells through a minimal blood draw).

In the second experiment, the MBR was implemented as an opto-thermal sensor and the contrast agent absorption spectrum was reconstruct through the temperature shift generated by optical absorption. In analogy with the previous implementation, the MBR allowed an ultra-compact all-optical configuration, capable of interrogate samples below 40 nl. Since the MBR uses a thermal shift to estimate particles absorption, the measurement is insensitive to light scattering, making the system promising in the case of opaque biological samples or high-scattering contrast agents. Additionally, due to the analogies between the two setups, it is possible to envisage a combination of the two

system, allowing to perform the two characterisation measurements in rapid succession.

Finally, regarding the light collection from single-photon sources, the investigation was theoretical/computational and has shown that the MBR system represents an interesting possibility for the dibenzoterrylene (DBT) molecules. The results of the computations, in fact, indicate strong coupling for a cryogenic configuration, but also good performance at room temperature. In particular, the photon indistinguishability remains high even in this challenging regime, and the presence of the cavity is an improvement with respect to the free-space configuration. These results represent a promising outlook for the realisation of the envisaged configuration.

To support this theoretical study, an analytical theory of the MBR modes extending the microsphere case to the microbubble case was developed, since no similar dissertation was found in literature. The theory has been developed with a formal approach and allowed to compute key quantities such as the modal volume of the WGMs and their spatial distribution. In addition, the theory also allows for finalisations outside of the scope of this thesis work, such as the computation of non linearities thresholds or the coupling of the MBR with other photonic structures.



# Appendix A

## Details on derivation of the microbubble WGMs

This Appendix derives in detail the key expressions used in Chapter 2 to deduce the Whispering Gallery modes of an MBR.

### A.1 Wave equation in a homogeneous medium

In absence of free charges  $\rho$  and free currents  $\mathbf{J}$ , Maxwell's Equations for an homogeneous dielectric medium are

$$\left\{ \begin{array}{l} \nabla \cdot \mathbf{D}(\mathbf{r}, t) = 0 \\ \nabla \cdot \mathbf{B}(\mathbf{r}, t) = 0 \\ \nabla \wedge \mathbf{E}(\mathbf{r}, t) = -\frac{\partial \mathbf{B}(\mathbf{r}, t)}{\partial t} \\ \nabla \wedge \mathbf{H}(\mathbf{r}, t) = \frac{\partial \mathbf{D}(\mathbf{r}, t)}{\partial t} \end{array} \right. \quad (\text{A.1})$$

where, adopting standard notations,  $\mathbf{E}$  is the electric field,  $\mathbf{D}$  is the electric induction field,  $\mathbf{H}$  is the magnetic field and  $\mathbf{B}$  is the magnetic induction field. For each field the dependence on time  $t$  and position  $\mathbf{r}$  is explicitly reported.

In addition to homogeneity, one can assume the dielectric to be non-magnetic and non-birefringent, leading to the following constitutive relationships

$$\left\{ \begin{array}{l} \mathbf{D}(\mathbf{r}, t) = \epsilon_0 \epsilon_r \mathbf{E}(\mathbf{r}, t) \\ \mathbf{B}(\mathbf{r}, t) = \mu_0 \mu_r \mathbf{H}(\mathbf{r}, t) = \mu_0 \mathbf{H}(\mathbf{r}, t) \\ n = \sqrt{\epsilon_r \mu_r} = \sqrt{\epsilon_r} \end{array} \right. \quad (\mu_r = 1) \quad (\text{A.2}) \quad (\text{A.3}) \quad (\text{A.4})$$

which allow to describe the properties of the medium using only one parameter: the refractive index  $n$ . Adopting standard notations,  $\epsilon_r$  and  $\mu_r$  are the relative dielectric

and magnetic constants of the medium, while  $\epsilon_0$  and  $\mu_0$  are the dielectric and magnetic constants of the vacuum. In the previous Equations, the non-magnetic hypothesis is readily used, setting  $\mu_r = 1$ .

Through Equations (A.2) and (A.3) Maxwell's Equations can be written using only  $\mathbf{E}$  and  $\mathbf{H}$ , which are the main fields for the theory here presented:

$$\left\{ \begin{array}{l} \nabla \cdot \mathbf{E}(\mathbf{r}, t) = 0 \\ \nabla \cdot \mathbf{H}(\mathbf{r}, t) = 0 \\ \nabla \wedge \mathbf{E}(\mathbf{r}, t) = -\mu_0 \frac{\partial \mathbf{H}(\mathbf{r}, t)}{\partial t} \\ \nabla \wedge \mathbf{H}(\mathbf{r}, t) = \epsilon_0 \epsilon_r \frac{\partial \mathbf{E}(\mathbf{r}, t)}{\partial t} \end{array} \right. . \quad (\text{A.5})$$

The time dependence and the position dependence appearing in both  $\mathbf{E}$  and  $\mathbf{H}$  can be separated by assuming the fields to be monochromatic with frequency  $\nu$  and introducing the complex fields  $\mathcal{E}(\mathbf{r})$  and  $\mathcal{H}(\mathbf{r})$ :

$$\left\{ \begin{array}{l} \mathbf{E}(\mathbf{r}, t) = \frac{1}{2} (\mathcal{E}(\mathbf{r}) e^{i\omega t} + \mathcal{E}^*(\mathbf{r}) e^{-i\omega t}) \\ \mathbf{H}(\mathbf{r}, t) = \frac{1}{2} (\mathcal{H}(\mathbf{r}) e^{i\omega t} + \mathcal{H}^*(\mathbf{r}) e^{-i\omega t}) \end{array} \right. \quad (\text{A.6})$$

with  $\omega = 2\pi\nu$  being the angular frequency. These definitions ensure that the physical fields  $\mathbf{E}$  and  $\mathbf{H}$  are real-valued for any choice of the complex fields  $\mathcal{E}$  and  $\mathcal{H}$ . By inserting the definitions (A.6) into the Maxwell's Equations (A.5), one obtains the following relationships between the complex fields

$$\left\{ \begin{array}{l} \nabla \cdot \mathcal{E}(\mathbf{r}) = 0 \\ \nabla \cdot \mathcal{H}(\mathbf{r}) = 0 \\ \nabla \wedge \mathcal{E}(\mathbf{r}) = -i\omega \mu_0 \mathcal{H}(\mathbf{r}) \\ \nabla \wedge \mathcal{H}(\mathbf{r}) = i\omega \epsilon_0 \epsilon_r \mathcal{E}(\mathbf{r}) \end{array} \right. . \quad (\text{A.7})$$

$$\nabla \cdot \mathcal{H}(\mathbf{r}) = 0 \quad (\text{A.8})$$

$$\nabla \wedge \mathcal{E}(\mathbf{r}) = -i\omega \mu_0 \mathcal{H}(\mathbf{r}) \quad (\text{A.9})$$

$$\nabla \wedge \mathcal{H}(\mathbf{r}) = i\omega \epsilon_0 \epsilon_r \mathcal{E}(\mathbf{r}) \quad (\text{A.10})$$

From these Equations it is possible to deduce the wave equation for both the  $\mathcal{E}$  field and  $\mathcal{H}$  the field. For example, focusing on  $\mathcal{E}$ , one has to apply the rotor operator to Eq. (A.9), introduce Eq. (A.10) and finally use Eq. (A.7) to arrive at

$$\nabla^2 \mathcal{E}(\mathbf{r}) + k^2 \mathcal{E}(\mathbf{r}) = \mathbf{0} \quad , \quad (\text{A.11})$$

where the conventional expressions for the light speed  $c$ , the vacuum wavenumber  $k_0$ , the vacuum wavelength  $\lambda_0$ , the wavenumber in the medium  $k$  and the wavelength in the

medium  $\lambda$  are used:

$$\begin{cases} c = \frac{1}{\sqrt{\epsilon_0 \mu_0}} & \lambda_0 = \frac{c}{\nu} & k_0 = \frac{2\pi}{\lambda_0} \end{cases} \quad (\text{A.12})$$

$$\begin{cases} k = k_0 \sqrt{\epsilon_r} = k_0 n \end{cases} \quad (\text{A.13})$$

$$\begin{cases} \lambda = \frac{2\pi}{k} = \frac{\lambda_0}{n} \end{cases} \quad (\text{A.14})$$

An analogous wave equation for  $\mathcal{H}$  can be deduced applying the same procedure. However, without losing in generality, one can work just with Eq. (A.11), since the two fields are connected through Equations (A.7)-(A.10). In particular, once  $\mathcal{E}$  is found,  $\mathcal{H}$  can be computed directly through Eq. (A.9):

$$\mathcal{H}(\mathbf{r}) = \frac{i}{\omega \mu_0} (\nabla \wedge \mathcal{E}(\mathbf{r})) \quad . \quad (\text{A.15})$$

To obtain a field satisfying Eq. (A.11), it is possible to use the Hansen method [144, 145], which derives the complex vectorial field  $\mathcal{E}$  from the function  $\psi(r, \theta, \phi)$  satisfying the *scalar* wave equation:

$$\nabla^2 \psi(r, \theta, \phi) + k^2 \psi(r, \theta, \phi) = 0 \quad . \quad (\text{A.16})$$

In particular, the Hansen method provides three different kind of vectorial solutions

$$\begin{cases} \mathbf{L} = \nabla \psi \\ \mathbf{M} = \nabla \psi \wedge \mathbf{r} = \mathbf{L} \wedge \mathbf{r} \\ \mathbf{N} = \frac{1}{k} (\nabla \wedge \mathbf{M}) \end{cases} \quad , \quad (\text{A.17})$$

which are discussed in the following of this Section: at this stage, the goal is to find the explicit form of the function  $\psi(r, \theta, \phi)$ .

To do this, the angular and the radial dependencies of  $\psi(r, \theta, \phi)$  are separated by the use of the spherical harmonic  $Y_{\ell, m}(\theta, \phi)$  and the introduction of a radial function  $f(r)$ . In this way  $\psi(r, \theta, \phi)$  assumes the form

$$\psi(r, \theta, \phi) = f(r) Y_{\ell, m}(\theta, \phi) \quad , \quad (\text{A.18})$$

which can be inserted into Eq. (A.16) to give [129]

$$r^2 f''(r) + 2r f'(r) + (k^2 r^2 - \ell(\ell + 1)) f(r) = 0 \quad .$$

To solve this differential equation, it is useful to apply the change of variable  $x = kr$  and recast Eq. (A.1) as

$$F''(x) + \frac{2}{x} F'(x) + \left(1 - \frac{\ell(\ell + 1)}{x^2}\right) F(x) = 0 \quad , \quad (\text{A.19})$$

where  $F(x)$  is the function  $f(r)$  evaluated with the new variable:  $F(x) = f(r)$ . Equation (A.19) is a modified Bessel equation and its solutions are [146]

$$F_1(x) = \frac{J_s(x)}{\sqrt{x}} \quad \text{or} \quad F_2(x) = \frac{Y_s(x)}{\sqrt{x}} \quad (s = \ell + 1/2)$$

where  $J_s(x)$  and  $Y_s(x)$  are the conventional Bessel functions of the first and second kind, respectively; and  $s = \ell + 1/2$  is the order of the functions. A superposition of  $F_1(x)$  and  $F_2(x)$  is the most general solution of Eq. (A.19) and therefore one can set

$$F(x) = A_1 \frac{J_s(x)}{\sqrt{x}} + A_2 \frac{Y_s(x)}{\sqrt{x}} \quad (s = \ell + 1/2) \quad (\text{A.20})$$

where  $A_1$  and  $A_2$  are the combination coefficients.

Recalling that  $f(r) = F(kr)$  and using the solution given in Eq. (A.20), one finally writes the function  $\psi(r, \theta, \phi)$ , solution of the scalar wave equation, as follows

$$\begin{cases} \psi(r, \theta, \phi) = F(kr) Y_{\ell, m}(\theta, \phi) \\ F(kr) = A_1 \frac{J_s(kr)}{\sqrt{kr}} + A_2 \frac{Y_s(kr)}{\sqrt{kr}} \end{cases} \quad (s = \ell + 1/2) \quad (\text{A.21})$$

This form shows explicitly the  $r$  and the  $k$  dependence of the radial function, which is useful for Section A.2, where boundary conditions for the  $\mathcal{E}$  and  $\mathcal{H}$  fields are deduced.

Solved the scalar problem, one can use Equations (A.17), to compute the vectorial solutions  $\mathbf{L}$ ,  $\mathbf{M}$  and  $\mathbf{N}$ . The expressions of these vectorial solutions are better visualised by introducing the auxiliary vectors  $\mathbf{X}_{\ell, m}$ ,  $\mathbf{Y}_{\ell, m}$  and  $\mathbf{Z}_{\ell, m}$ , which are derived from the spherical harmonic  $Y_{\ell, m}(\theta, \phi)$  as follows:

$$\begin{cases} \mathbf{X}_{\ell, m} = \nabla Y_{\ell, m} \wedge \mathbf{r} = 0 \hat{\mathbf{r}} + \frac{1}{\sin \theta} \frac{\partial}{\partial \phi} Y_{\ell, m} \hat{\boldsymbol{\theta}} - \frac{\partial}{\partial \theta} Y_{\ell, m} \hat{\boldsymbol{\phi}} & (\text{A.22}) \\ \mathbf{Y}_{\ell, m} = r \nabla Y_{\ell, m} = 0 \hat{\mathbf{r}} + \frac{\partial}{\partial \theta} Y_{\ell, m} \hat{\boldsymbol{\theta}} + \frac{1}{\sin \theta} \frac{\partial}{\partial \phi} Y_{\ell, m} \hat{\boldsymbol{\phi}} & (\text{A.23}) \\ \mathbf{Z}_{\ell, m} = Y_{\ell, m} \hat{\mathbf{r}} \quad . & (\text{A.24}) \end{cases}$$

In these expressions  $\hat{\mathbf{r}}$ ,  $\hat{\boldsymbol{\theta}}$  and  $\hat{\boldsymbol{\phi}}$  are the basis vectors in spherical coordinates and the explicit  $(\theta, \phi)$  dependence in  $Y_{\ell, m}(\theta, \phi)$  was not listed to have more compact expressions. With the aid of these auxiliary vectors,  $\mathbf{L}$ ,  $\mathbf{M}$  and  $\mathbf{N}$  can be written as

$$\begin{cases} \mathbf{L} = \frac{dF(kr)}{dr} \mathbf{Z}_{\ell, m} + \frac{F(kr)}{r} \mathbf{Y}_{\ell, m} & (\text{A.25}) \end{cases}$$

$$\begin{cases} \mathbf{M} = F(kr) \mathbf{X}_{\ell, m} & (\text{A.26}) \end{cases}$$

$$\begin{cases} \mathbf{N} = \frac{\ell(\ell+1)}{kr} F(kr) \mathbf{Z}_{\ell, m} + \frac{1}{kr} \frac{d}{dr} (rF(kr)) \mathbf{Y}_{\ell, m} & (\text{A.27}) \end{cases}$$

From these expressions, or directly from the definitions (A.17) in combination with the scalar wave equation (A.16), it is possible to verify that

$$\begin{cases} \nabla \cdot \mathbf{L} = -k^2 \psi \\ \nabla \cdot \mathbf{M} = 0 \\ \nabla \cdot \mathbf{N} = 0 \end{cases} .$$

These properties imply that only  $\mathbf{M}$  and  $\mathbf{N}$  are acceptable solutions for  $\mathcal{E}$ , since Eq. (A.7) requires null divergence for this field. In addition, by applying the rotor operator to the  $\mathbf{N}$  definition given in (A.17) and using  $\nabla \cdot \mathbf{M} = 0$ , one obtains an alternative formula for  $\mathbf{M}$ :

$$\mathbf{M} = \frac{1}{k} (\nabla \wedge \mathbf{N}) \quad , \quad (\text{A.28})$$

which is a convenient recasting for the next paragraph.

Assigning the  $\mathbf{M}$  solution or the  $\mathbf{N}$  solution to the field  $\mathcal{E}$  leads to transverse electric (TE) or transverse magnetic (TM) modes, respectively. Starting from the TE case, which assumes  $\mathcal{E} = \mathbf{M}$ , one can write the following expressions for both  $\mathcal{E}$  and  $\mathcal{H}$ :

$$\text{TE mode} \begin{cases} \mathcal{E} = \mathbf{M} = F(kr) \mathbf{X}_{\ell,m} & (\text{A.29}) \\ \mathcal{H} \stackrel{(\text{A.15})}{=} \frac{i}{\omega \mu_0} (\nabla \wedge \mathcal{E}) = \frac{i}{\omega \mu_0} (\nabla \wedge \mathbf{M}) \stackrel{(\text{A.17})}{=} \frac{ik}{\omega \mu_0} \mathbf{N} = \\ = \frac{i}{\omega \mu_0} \left[ \frac{\ell(\ell+1)}{r} F(kr) \mathbf{Z}_{\ell,m} + \frac{1}{r} \frac{d}{dr} (rF(kr)) \mathbf{Y}_{\ell,m} \right] & (\text{A.30}) \end{cases}$$

where the numbers above the equal signs mark the Equation used for that step and the expressions for  $\mathbf{N}$  and  $\mathbf{M}$  are taken directly from Equations (A.26) and (A.27). In terms of spatial direction, the electric field  $\mathcal{E}$  is parallel to  $\mathbf{X}_{\ell,m}$ , which is defined through a combination of the tangential vectors  $\hat{\boldsymbol{\theta}}$  and  $\hat{\boldsymbol{\phi}}$  in Eq. (A.22). Therefore  $\mathcal{E}$  is orthogonal to the radial direction  $\hat{\mathbf{r}}$  and for this reason the mode is named *transverse electric*. The magnetic field  $\mathcal{H}$ , instead, has a tangential component, associated with the vector  $\mathbf{Y}_{\ell,m}$ , and a radial component, associated with the vector  $\mathbf{Z}_{\ell,m}$ .

Moving to the TM case, one sets  $\mathcal{E} = \mathbf{N}$  and repeats the previous substitutions to obtain:

$$\text{TM mode} \begin{cases} \mathcal{E} = \mathbf{N} = \frac{\ell(\ell+1)}{kr} F(kr) \mathbf{Z}_{\ell,m} + \frac{1}{kr} \frac{d}{dr} (rF(kr)) \mathbf{Y}_{\ell,m} & (\text{A.31}) \\ \mathcal{H} \stackrel{(\text{A.15})}{=} \frac{i}{\omega \mu_0} (\nabla \wedge \mathcal{E}) = \frac{i}{\omega \mu_0} (\nabla \wedge \mathbf{N}) \stackrel{(\text{A.28})}{=} \frac{ik}{\omega \mu_0} \mathbf{M} = \\ = \frac{ik}{\omega \mu_0} F(kr) \mathbf{X}_{\ell,m} \quad . & (\text{A.32}) \end{cases}$$

At variance with the previous case, now it is the magnetic field  $\mathcal{H}$  to be aligned with  $\mathbf{X}_{\ell,m}$  and orthogonal to  $\hat{\mathbf{r}}$ , therefore justifying the name *transverse magnetic* for these

modes. The electric field  $\mathcal{E}$ , instead, has both a radial and a tangential component, due to the presence of  $\mathbf{Y}_{\ell,m}$  and  $\mathbf{Z}_{\ell,m}$  in Eq. (A.31).

In the next Section the fields expressions reported in Equations (A.29)- (A.32) are used to impose boundary conditions at the dielectric interfaces and deduce the characteristic equations leading to the microbubble Whispering Gallery modes.

## A.2 Field matching and characteristic equation

The modelling introduced in Section 2.1 divides the microbubble resonator into three sectors: the core, the wall and the external medium surrounding the microbubble (cf. Figure 2.1). Each sector is a homogeneous dielectric medium and therefore, for each sector, it is possible to write Equations (A.29)-(A.32). Due to the abrupt change of index at the core-wall interface in  $r = R_c$  and at the wall-external interface in  $r = R_e$ , it is necessary to impose boundary conditions on the electric and magnetic fields. From these conditions the characteristic equations for the TE mode and the TM modes arise, limiting the possible values for the wavelength  $\lambda$  and therefore defining the spectrum of the microbubble Whispering Gallery modes. For brevity, only the procedure leading to the TE characteristic equation is reported in detail: the procedure for the TM equation is identical and only the main result is here reported.

The first step of the procedure consists in reviewing the number of combination coefficients that are necessary to define the function  $F(kr)$ . In general, recalling Eq. (A.21), it is possible to write

$$F(kr) = \begin{cases} A_1^c \frac{J_s(k_c r)}{\sqrt{k_c r}} + A_2^c \frac{Y_s(k_c r)}{\sqrt{k_c r}} & r < R_c \text{ (core)} \\ A_1^w \frac{J_s(k_w r)}{\sqrt{k_w r}} + A_2^w \frac{Y_s(k_w r)}{\sqrt{k_w r}} & R_c < r < R_e \text{ (wall)} \\ A_1^e \frac{J_s(k_e r)}{\sqrt{k_e r}} + A_2^e \frac{Y_s(k_e r)}{\sqrt{k_e r}} & r > R_e \text{ (external)} \end{cases}, \quad (\text{A.33})$$

which resumes the definition of  $F(kr)$  in the three sectors. As in Eq. (A.21), the index  $s = \ell + 1/2$  is the order of the Bessel functions, while  $k_c$ ,  $k_w$  and  $k_e$  are the wavenumbers in the different media (cf. Eq. (A.13)). Indeed, Eq. (A.33) features six combination coefficients, but  $A_2^c$  and  $A_1^e$  need to be zero in order to have a physically acceptable function. In fact the Bessel functions  $Y_p(x)$  have a divergence in  $x = 0$  for any order  $p$  and therefore are not suitable to be used in the core sector, implying  $A_2^c = 0$ . The Bessel functions  $J_p(x)$ , instead, features slowly decaying oscillations in the limit of high  $x$  and therefore are not suitable to describe the evanescent tail of a Whispering Gallery mode

in the external sector, implying  $A_1^e = 0$ . In conclusion,  $F(kr)$  becomes

$$F(kr) = \begin{cases} A^c \frac{J_s(k_c r)}{\sqrt{k_c r}} & r < R_c \text{ (core)} \\ A_1^w \frac{J_s(k_w r)}{\sqrt{k_w r}} + A_2^w \frac{Y_s(k_w r)}{\sqrt{k_w r}} & R_c < r < R_e \text{ (wall)} \\ A^e \frac{Y_s(k_e r)}{\sqrt{k_e r}} & r > R_e \text{ (external)} \end{cases}, \quad (\text{A.34})$$

which only has four combination coefficients.

The next step is to require the continuity of the *tangential* component of the  $\mathbf{E}$  and  $\mathbf{H}$  fields at the core-wall interface ( $r = R_c$ ) and at the wall-external interface ( $r = R_e = R_c + W$ ) for both TE and TM modes. This requirement can be equivalently fulfilled by shifting the condition on the complex fields  $\mathcal{E}$  and  $\mathcal{H}$ , defining a set of mathematical conditions through the analytical expressions in Equations (A.29)-(A.32). In practise, recalling that the tangential components are associated with the auxiliary vectors  $\mathbf{X}_{\ell,m}$  and  $\mathbf{Y}_{\ell,m}$ , one requires the continuity of the following quantities at the two interfaces

$$\text{TE mode} \begin{cases} F(kr) & \text{for the } \mathcal{E} \text{ field} \\ \frac{1}{r} \frac{d}{dr} (rF(kr)) & \text{for the } \mathcal{H} \text{ field} \end{cases} \quad (\text{A.35})$$

$$\quad (\text{A.36})$$

$$\text{TM mode} \begin{cases} \frac{1}{kr} \frac{d}{dr} (rF(kr)) & \text{for the } \mathcal{E} \text{ field} \\ k F(kr) & \text{for the } \mathcal{H} \text{ field} \end{cases} \quad (\text{A.37})$$

$$\quad (\text{A.38})$$

Additionally, it is important to highlight that these conditions also have consequences on the radial components of the fields. In particular, the continuity of  $F(kr)$  for TE modes (Eq. (A.35)) also implies the continuity of the radial component of  $\mathcal{H}$  (cfr. Eq. (A.30)), while the continuity of  $k F(kr)$  for TM modes (Eq. (A.38)) implies a discontinuity of the radial component of  $\mathcal{E}$  (cfr. Eq. (A.31)).

As anticipated at the beginning of the Section, the discussion now focuses on TE modes to give a detailed description of the procedure leading to the characteristic equation. This procedure begins with translating the continuity requirements into a set of conditions on the combination coefficients ( $A^c$ ,  $A_1^w$ ,  $A_2^w$ ,  $A^e$ ) through Eq. (A.34).

For the core-wall interface at  $r = R_c$ , Equations (A.35) and (A.36) imply, respectively:

$$A^c \frac{J_s(k_c R_c)}{\sqrt{k_c R_c}} = A_1^w \frac{J_s(k_w R_c)}{\sqrt{k_w R_c}} + A_2^w \frac{Y_s(k_w R_c)}{\sqrt{k_w R_c}} \quad (\text{A.39})$$

$$\left. \frac{A^c}{R_c} \frac{d}{dr} \left( r \frac{J_s(k_c r)}{\sqrt{k_c r}} \right) \right|_{r=R_c} = \left. \frac{A_1^w}{R_c} \frac{d}{dr} \left( r \frac{J_s(k_w r)}{\sqrt{k_w r}} \right) \right|_{r=R_c} + \left. \frac{A_2^w}{R_c} \frac{d}{dr} \left( r \frac{Y_s(k_w r)}{\sqrt{k_w r}} \right) \right|_{r=R_c} \quad (\text{A.40})$$

The simplification of Eq. (A.39) is straightforward when recalling that each wavevector is proportional to the vacuum wavevector  $k_0$  (cf. Eq. (A.3)). For Eq. (A.40), instead, the simplification takes more steps due to the presence of the derivatives. In particular, it is convenient to write the Bessel functions derivatives using the properties

$$J'_n(x) = J_{n-1}(x) - \frac{n}{x} J_n(x) \quad \text{and} \quad Y'_n(x) = Y_{n-1}(x) - \frac{n}{x} Y_n(x) \quad ,$$

which is a convenient choice also in terms of numerical computation, since the Bessel function derivative is substituted with a difference between two Bessel functions. At the end of the simplifications, Equations (A.39) and (A.40) become

$$\left\{ \begin{array}{l} A^c \frac{J_s(k_c R_c)}{\sqrt{n_c}} = A_1^w \frac{J_s(k_w R_c)}{\sqrt{n_w}} + A_2^w \frac{Y_s(k_w R_c)}{\sqrt{n_w}} \end{array} \right. \quad (\text{A.41})$$

$$\left\{ \begin{array}{l} A^c \frac{P_s(k_c R_c)}{\sqrt{n_c}} = A_1^w \frac{P_s(k_w R_c)}{\sqrt{n_w}} + A_2^w \frac{V_s(k_w R_c)}{\sqrt{n_w}} \end{array} \right. \quad , \quad (\text{A.42})$$

where the auxiliary functions  $P_s(x)$  and  $V_s(x)$  are defined as

$$P_s(x) = x J_{s-1}(x) - \ell J_s(x) \quad (\text{A.43})$$

$$V_s(x) = x Y_{s-1}(x) - \ell Y_s(x) \quad . \quad (\text{A.44})$$

Repeating the same passages for the wall-external interface at  $r = R_e$  leads to

$$\left\{ \begin{array}{l} A_1^w \frac{J_s(k_w R_e)}{\sqrt{n_w}} + A_2^w \frac{Y_s(k_w R_e)}{\sqrt{n_w}} = A^e \frac{Y_s(k_e R_e)}{\sqrt{n_e}} \end{array} \right. \quad (\text{A.45})$$

$$\left\{ \begin{array}{l} A_1^w \frac{P_s(k_w R_e)}{\sqrt{n_w}} + A_2^w \frac{V_s(k_w R_e)}{\sqrt{n_w}} = A^e \frac{V_s(k_e R_e)}{\sqrt{n_e}} \end{array} \right. \quad (\text{A.46})$$

with the same definition for  $P_s(x)$  and  $V_s(x)$ . For compactness and better handling, Equations (A.41)-(A.42) and (A.45)-(A.46) are grouped into a system, which is here reported using the matrix formalism:

$$\underbrace{\begin{pmatrix} \frac{J_s(k_c R_c)}{\sqrt{n_c}} & -\frac{J_s(k_w R_c)}{\sqrt{n_w}} & -\frac{Y_s(k_w R_c)}{\sqrt{n_w}} & 0 \\ \frac{P_s(k_c R_c)}{\sqrt{n_c}} & -\frac{P_s(k_w R_c)}{\sqrt{n_w}} & -\frac{V_s(k_w R_c)}{\sqrt{n_w}} & 0 \\ 0 & -\frac{J_s(k_w R_e)}{\sqrt{n_w}} & -\frac{Y_s(k_w R_e)}{\sqrt{n_w}} & \frac{Y_s(k_e R_e)}{\sqrt{n_e}} \\ 0 & -\frac{P_s(k_w R_e)}{\sqrt{n_w}} & -\frac{V_s(k_w R_e)}{\sqrt{n_w}} & \frac{V_s(k_e R_e)}{\sqrt{n_e}} \end{pmatrix}}_{\mathcal{M}_{\text{TE}}} \underbrace{\begin{pmatrix} A^c \\ A_1^w \\ A_2^w \\ A^e \end{pmatrix}}_{\mathcal{A}} = \begin{pmatrix} 0 \\ 0 \\ 0 \\ 0 \end{pmatrix} \quad . \quad (\text{A.47})$$



---

## Appendix A. Details on derivation of the microbubble WGMs

Indeed, setting all combination coefficients to zero ( $\mathcal{A} = \mathbf{0}$ ) would satisfy Eq. (A.47), but it would also lead to null fields, which are not physically acceptable. To have non-zero coefficients satisfying Eq. (A.47), the matrix  $\mathcal{M}_{\text{TE}}$  must have a null determinant:

$$\det[\mathcal{M}_{\text{TE}}] = 0 \quad . \quad (\text{A.48})$$

Before moving to the TM case, it is important to review the parameters appearing in  $\mathcal{M}_{\text{TE}}$ . Since the aim of the theory here presented is to deduce the spectrum of an *assigned* microbubble resonator, both its geometry and its composition are to be considered fixed and therefore the indexes and radii appearing in Eq. (A.47) have to be regarded as fixed constants. From Eq. (A.13), one notices that all three wavenumbers appearing  $\mathcal{M}_{\text{TE}}$  are proportional to the vacuum wavenumber  $k_0$ , since  $k_x = k_0 n_x = 2\pi n_x / \lambda_0$  for any  $x = \{c, w, e\}$ . This implies that the matrix  $\mathcal{M}_{\text{TE}}$  depends only on  $k_0$ , or equivalently on the vacuum wavelength  $\lambda_0$ , and not on the three wavenumbers separately. Finally, a dependency on the  $\ell$  number (degree of the spherical harmonic  $Y_{\ell, m}$ ) is present due to  $s = \ell + 1/2$ , which is the order of the Bessel functions and of the auxiliary functions  $P_s(x)$  and  $V_s(x)$ . In conclusion,  $\mathcal{M}_{\text{TE}}$  depends explicitly only on  $\lambda_0$  and  $\ell$ , and therefore Eq. (A.48) can be recasted as

$$\det[\mathcal{M}_{\text{TE}}(\lambda_0, \ell)] = 0 \quad . \quad (\text{A.49})$$

This condition can be satisfied only by specific  $(\lambda_0, \ell)$  combinations, with each combination defining the resonance wavelengths of the WGMs and their field distribution. For these reasons, Eq. (A.49) is the *characteristic equation for the TE modes* and its resolution is discussed in Section 2.3 to show the features of of the WGM spectrum.

As mentioned at the beginning of the Section, the process leading to the TM characteristic equation is the same as the one here presented for the TE modes. In the TM case the system resulting from the boundary conditions is

$$\underbrace{\begin{pmatrix} \frac{P_s(k_c R_c)}{n_c^{3/2}} & -\frac{P_s(k_w R_c)}{n_w^{3/2}} & -\frac{V_s(k_w R_c)}{n_w^{3/2}} & 0 \\ \sqrt{n_c} J_s(k_c R_c) & -\sqrt{n_w} J_s(k_w R_c) & -\sqrt{n_w} Y_s(k_w R_c) & 0 \\ 0 & -\frac{P_s(k_w R_e)}{n_w^{3/2}} & -\frac{V_s(k_w R_e)}{n_w^{3/2}} & \frac{V_s(k_e R_e)}{n_e^{3/2}} \\ 0 & -\sqrt{n_w} J_s(k_w R_e) & -\sqrt{n_w} Y_s(k_w R_e) & \sqrt{n_e} Y_s(k_e R_e) \end{pmatrix}}_{\mathcal{M}_{\text{TM}}} \underbrace{\begin{pmatrix} A^c \\ A_1^w \\ A_2^w \\ A^e \end{pmatrix}}_{\mathcal{A}} = \begin{pmatrix} 0 \\ 0 \\ 0 \\ 0 \end{pmatrix}, \quad (\text{A.50})$$

which is the counterpart of Eq. (A.47). Just as  $\mathcal{M}_{\text{TE}}$ , even  $\mathcal{M}_{\text{TM}}$  depends only on  $(\lambda_0, \ell)$  and must have null determinant, leading to

$$\det[\mathcal{M}_{\text{TM}}(\lambda_0, \ell)] = 0 \quad (\text{A.51})$$

which is the *characteristic equation for the TM modes*.

### A.3 Computation of the radial function $F$

Recalling its definition from Eq. (A.34), the elements required for the computation of  $F(kr)$  are the three wavenumbers ( $k_c$ ,  $k_w$ ,  $k_e$ ) and the four combination coefficients ( $A^c$ ,  $A_1^w$ ,  $A_2^w$ ,  $A^e$ ). Since the resonance wavelength  $\lambda_0^{(n,\ell)}$  is assumed to be already known from the numerical solution of the characteristic equation, the three wavenumbers are readily computed through Eq. (A.13) and can be regarded as fixed constants. The combination coefficients, instead, are deduced in the following of this Section. For the sake of brevity, the details of the resolution method are reported only for the TE case.

Recalling the characteristic equation (A.49), the TE resonance wavelengths  $\lambda_0^{(n,\ell)}$  are defined as the wavelengths producing a vanishing determinant for the matrix  $\mathcal{M}_{\text{TE}}$ . This, in turn, implies that three combination parameters can be written as a function of the fourth, which remains free (cf. Eq. (A.47)). This freedom has a physical meaning, since the independent parameter fixes the amount of energy stored in the mode. Assuming to use  $A^c$  as the free parameter, the first two equations from system (A.47) can be extracted and the terms with  $A^c$  moved the right side to obtain

$$\begin{pmatrix} \frac{J_s(k_w R_c)}{\sqrt{n_w}} & \frac{Y_s(k_w R_c)}{\sqrt{n_w}} \\ \frac{P_s(k_w R_c)}{\sqrt{n_w}} & \frac{V_s(k_w R_c)}{\sqrt{n_w}} \end{pmatrix} \begin{pmatrix} A_1^w \\ A_2^w \end{pmatrix} = \begin{pmatrix} \frac{J_s(k_c R_c)}{\sqrt{n_c}} A^c \\ \frac{P_s(k_c R_c)}{\sqrt{n_c}} A^c \end{pmatrix}. \quad (\text{A.52})$$

In this system  $A^c$  has to be regarded as a fixed constant (e.g.  $A^c = 1$  V/m) with  $A_1^w$  and  $A_2^w$  being the unknown variables. These variables can be deduced by applying Cramer's rule to system (A.52), obtaining

$$A_1^w = \sqrt{\frac{n_w}{n_c}} \frac{J_s(k_c R_c) V_s(k_w R_c) - Y_s(k_w R_c) P_s(k_c R_c)}{J_s(k_w R_c) V_s(k_w R_c) - Y_s(k_w R_c) P_s(k_w R_c)} A^c \quad (\text{A.53})$$

$$A_2^w = \sqrt{\frac{n_w}{n_c}} \frac{J_s(k_w R_c) P_s(k_c R_c) - J_s(k_c R_c) P_s(k_w R_c)}{J_s(k_w R_c) V_s(k_w R_c) - Y_s(k_w R_c) P_s(k_w R_c)} A^c. \quad (\text{A.54})$$

Then, extracting the third equation from system (A.47), or directly recalling Eq. (A.45),  $A^e$  can be deduced as

$$A^e = \sqrt{\frac{n_e}{n_w}} \frac{J_s(k_w R_e) A_1^w + Y_s(k_w R_e) A_2^w}{Y_s(k_e R_e)} \quad (\text{A.55})$$

where  $A_1^w$  and  $A_2^w$  are already known from Eq. (A.53) and Eq. (A.54), respectively. It is worth noticing that Equations (A.53), (A.54) and (A.55) depend from the  $\ell$  number through  $s = \ell + 1/2$  and from  $\lambda_0^{(n,\ell)}$  through the wavenumbers  $k_c$ ,  $k_w$ ,  $k_e$ . Therefore, modes with the same  $(n, \ell)$  combination have the same  $F(kr)$  function.

The combinations coefficients for the TM modes can be obtained with the same procedure, starting from the matrix  $\mathcal{M}_{\text{TM}}$  in Eq. (A.51). Keeping  $A^c$  as the free parameter,

the expressions for  $(A_1^w, A_2^w, A^e)$  are the following:

$$\left\{ \begin{array}{l} A_1^w = \sqrt{\frac{n_c}{n_w}} \frac{J_s(k_c R_c) V_s(k_w R_c) - q^2 Y_s(k_w R_c) P_s(k_c R_c)}{J_s(k_w R_c) V_s(k_w R_c) - Y_s(k_w R_c) P_s(k_w R_c)} A^c \quad (\text{A.56}) \\ A_2^w = \sqrt{\frac{n_c}{n_w}} \frac{q^2 J_s(k_w R_c) P_s(k_c R_c) - J_s(k_c R_c) P_s(k_w R_c)}{J_s(k_w R_c) V_s(k_w R_c) - Y_s(k_w R_c) P_s(k_w R_c)} A^c \quad (\text{A.57}) \\ A^e = \sqrt{\frac{n_w}{n_e}} \frac{J_s(k_w R_e) A_1^w + Y_s(k_w R_e) A_2^w}{Y_s(k_e R_e)} \quad (\text{A.58}) \end{array} \right.$$

where  $q = n_w/n_c$  in Equations (A.56) and (A.57) is introduced for better visualisation of the fractions. Comparing the expressions for the TE and TM cases, one notices that the refractive index ratio  $q = n_w/n_c$  plays a more important role in the TM case, due to the  $q^2$  in the fraction numerators.



# List of Publications

The implementation of the MBR as a PA sensor presented in Chapter 3 led to the publication of three articles as first author on the journals *Physical Review Applied*, *Sensors* and *Il Nuovo Cimento C*:

1. *G. Frigenti*, L. Cavigli, A. Fernández-Bienes, F. Ratto, S. Centi, T. García-Fernández, G. Nunzi Conti and S. Soria, Resonant Microbubble as a Microfluidic Stage for All-Optical Photoacoustic Sensing, *Physical Review Applied* **12**, 014062 (2019)
2. *G. Frigenti*, L. Cavigli, A. Fernández-Bienes, F. Ratto, S. Centi, T. García-Fernández, G. Nunzi Conti and S. Soria, Microbubble Resonators for All-Optical Photoacoustics of Flowing Contrast Agents, *Sensors* **20**, 1696 (2020)
3. *G. Frigenti*, Microbubble whispering gallery mode resonator as an all-optical platform for the characterisation of photoacoustics contrast agents, *Il Nuovo Cimento C* **43**, 127 (2020) (invited paper)

During the PhD programme I also contributed to activities of the research group outside of the ones described in this thesis, which led to the following publications:

4. *G. Frigenti*, M. Arjmand, A. Barucci, F. Baldini, S. Berneschi, D. Farnesi, M. Gianfreda, S. Pelli, S. Soria, A. Aray, Y. Dumeige, P. Féron and G. Nunzi Conti, Coupling analysis of high Q resonators in add-drop configuration through cavity ringdown spectroscopy, *Journal of Optics* **20**, 065706 (2018)
5. X. Roselló-Mechó, D. Farnesi, *G. Frigenti*, A. Barucci, A. Fernández-Bienes, T. García-Fernández, F. Ratto and M. Delgado-Pinar, M.V. Andrés, G. Nunzi Conti and S. Soria, Parametrical Optomechanical Oscillations in PhoXonic Whispering Gallery Mode Resonators, *Scientific Reports* **9**, 7163 (2019)
6. *G. Frigenti*, D. Farnesi, G. Nunzi Conti and S. Soria, Nonlinear Optics in Microspherical Resonators, *Micromachines* **11**, 303 (2020)

In particular, the first article stemmed from the activity of my master thesis (*Characterisation of high-Q whispering gallery mode optical resonators in add-drop configuration through cavity ring down spectroscopy*, defended on 19/04/2017, Florence University) and focused on the development of a general characterisation technique for optical resonators by studying their response to a non-stationary excitation. The second article,

instead, is a study on the mechanical oscillations of the MBR triggered by radiation pressure and their interaction with optical non-linearities. Lastly, the third article is a review on non-linear optical effects of the third order that can be produced in spherical micro-resonators, with a particular focus on microspheres and microbubbles.

In addition to journal articles, I also contributed to the preparation of the following conference proceedings:

7. *G. Frigenti*, M. Arjmand, A. Barucci, F. Baldini, S. Berneschi, D. Farnesi, M. Gianfreda, S. Pelli, S. Soria, A. Aray, Y. Dumeige, P. Féron and G. Nunzi Conti, Cavity-ringdown-spectroscopy-based study of high Q resonators in add-drop configuration, *Proceedings of SPIE volume 10904, Laser Resonators, Microresonators, and Beam Control XXI*, 1090416 (2019)
8. S. Berneschi, F. Cosi, D. Farnesi, *G. Frigenti*, G. C. Righini, S. Pelli, S. Soria, F. Baldini, F. Prudenzano, G. Persichetti, R. Bernini, Y. Dumeige, P. Féron, D. Ristić, M. Ivanda and G. Nunzi Conti, Glass based microresonators, *Proceedings of SPIE volume 10683, Fiber Lasers and Glass Photonics: Materials through Applications*, 106830F (2018)

Even in this case, the first proceeding is related with the master thesis activity; while the second is an overview of the decade-long activity of the group in the wide context of glass-based microresonators.

Finally, an article regarding the measurement of nanoparticles absorption spectrum through an MBR presented in Chapter 4 is in preparation.

# Bibliography

- [1] Lord Rayleigh. The problem of the whispering gallery. *Phil. Mag.*, 20(120):1001, 1910.
- [2] Lord Rayleigh. The problem of whispering gallery. *Scientific papers*, 5:617, 1912.
- [3] G. Mie. Beitung zur optik trüber melien, speziell kolloidaler metallosungen. *Ann. Phys.*, 25:377–445, 1908.
- [4] P. Debye. Der lichtdruck auf kugeln von beliebigem material. *Ann. Phys.*, 30:57–136, 1909.
- [5] B.R. Johnson. Morphology-Dependent Resonances of a dielectric sphere on a conducting plane. *Journal of Optical Society of America A*, 11(7):2055, 1994.
- [6] M.L. Gorodetsky, A.A. Savchenkov, and V.S. Ilchenko. Ultimate  $Q$  of optical microsphere resonators. *Optics Letters*, 21:453–455, 1996.
- [7] G.C. Righini, M. Brenci, A. Chiasera, P. Féron, M. Ferrari, G. Nunzi Conti, and S. Pelli. Whispering gallery mode resonators for microlasers and microsensors. *Proc. of SPIE*, 6029:602903, 2006.
- [8] F. Vollmer, D. Braun, A. Libchaber, M. Khoshshima, I. Teraoka, and S. Arnold. Protein detection by optical shift of a resonant microcavity. *Appl. Phys. Lett.*, 80:4057, 2002.
- [9] H. Zhu, J. D. Suter, I. M. White, and X. Fan. Aptamer based microsphere biosensor for thrombin detection. *Sensors*, 6:785, 2006.
- [10] D. Farnesi, F. Cosi, C. Trono, G. C. Righini, G. Nunzi Conti, and S. Soria. Stimulated anti-Stokes Raman scattering resonantly enhanced in silica microspheres. *Opt. Lett.*, 39(20):5993, 2014.
- [11] H.M. Tzeng, M.B. Long, R.K. Chang, and P. W. Barber. Laser-induced shape distortions of flowing droplets deduced from morphology-dependent resonances in fluorescence spectra. *Optics Letters*, 10:209–211, 1985.

- 
- [12] A.J. Campillo, J.D. Eversole, and H.B. Lin. Cavity quantum electrodynamics enhancement of stimulated emission in microdroplets. *Physical Review Letters*, 67:437, 1991.
- [13] Y. F. Yu, T. Bourouina, A. Q. Liu, M. K. Chin, C. S. Lim, and Y. C. Soh. Sandwiched droplet resonator for low concentration protein detection. *IEEE Conf. Proc. - 2008 PhotonicsGlobal@Singapore*, DOI: 10.1109/IPGC.2008.4781393:1 – 2, 2008.
- [14] M. R. Foreman, S. Avino, R. Zullo, H.-P. Looock, F. Vollmer, and G. Gagliardi. Enhanced nanoparticle detection with liquid droplet resonator. *European Physical Journal special topics*, 223:1971–1978, 2014.
- [15] Anatoliy A. Savchenkov, Vladimir S. Ilchenko, Andrey B. Matsko, and Lute Maleki. Kiloherz optical resonances in dielectric crystal cavities. *Physical Review A*, 70(5):051804, Nov 2004.
- [16] D. K. Armani, T. J. Kippenberg, S. M. Spillane, and K. J. Vahala. Ultra-high-Q toroid microcavity on a chip. *Nature*, 421:925–928, 2003.
- [17] Wim Bogaerts, Peter De Heyn, Thomas Van Vaerenbergh, Katrien DeVos, Shankar Kumar Selvaraj, Tom Claes and Pieter Dumon, Peter Bienstman, Dries Van Thourhout, and Roel Baets. Silicon microring resonators. *Laser Photonics Reviews*, 6(1):47 – 73, 2012.
- [18] A. Dousse, J. Suffczyński, R. Braive, A. Miard, A. Lemaitre, I. Sagnes, L. Lanco, J. Bloch, P. Voisin, and P. Senellart. Scalable implementation of strongly coupled cavity-quantum dot devices. *Applied Physics Letters*, 94:121102, 2009.
- [19] G. S. Solomon, M. Pelton, and Y. Yamamoto. Single-mode spontaneous emission from a single quantum dot in a three-dimensional microcavity. *Physical Review Letters*, 86(17):3903 – 3906, 2001.
- [20] M. Sumetsky, Y. Dulashko, and R. S. Windeler. Optical microbubble resonator. *Opt. Lett.*, 35(7):898–900, April 2010.
- [21] S. Berneschi, D. Farnesi, F. Cosi, G. Nunzi Conti, S. Pelli, G. C. Righini, and S. Soria. High Q silica microbubble resonators fabricated by arc discharge. *Opt. Lett.*, 36(17):3521–3523, September 2011.
- [22] Yong Yang, Sunny Saurabh, Jonathan M. Ward, and Sile Nic Chormaic. High-Q, ultrathin-walled microbubble resonator for aerostatic pressure sensing. *Optics Express*, 24(1):294 – 299, 2016.
- [23] M. Sumetsky. Whispering-gallery-bottle microcavities: the three-dimensional etalon. *Opt. Lett.*, 29:8–10, 2004.



- 
- [24] G Senthil Murugan, M N Petrovich, Y Jung, J S Wilkinson, and M N Zervas. Hollow-bottle optical microresonators. page 12, 2011.
- [25] Razvan-Ionut Stoian, Khoa V Bui, and A T Rosenberger. Silica hollow bottle resonators for use as whispering gallery mode based chemical sensors. *Journal of Optics*, 17(12):125011, December 2015.
- [26] Giancarlo C Righini. *Advanced sensing with micro-optical whispering-gallery-mode resonators*. Society of Photo-Optical Instrumentation Engineers (SPIE), Bellingham, 2017.
- [27] G. C. Righini, Y Dumeige, P Féron, M. Ferrari, G. Nunzi Conti, D Ristic, and S Soria. Whispering gallery mode microresonators: Fundamentals and applications. *La Rivista del Nuovo Cimento*, 34(7):435–488, June 2011.
- [28] K. J. Vahala. Optical microcavities. *Nature*, 424:839–846, August 2003.
- [29] A. Chiasera, Y. Dumeige, P. Feron, M. Ferrari, Y. Jestin, G. Nunzi Conti, S. Pelli, S. Soria, and G.C. Righini. Spherical whispering-gallery-mode microresonators. *Laser & Photonics Reviews*, 4:457 – 482, 2010.
- [30] J. Ward and O. Benson. WGM microresonators: sensing, lasing and fundamental optics with microspheres. *Laser & Photonics Reviews*, 5(4):553 – 570, 2011. DOI: 10.1002/lpor.201000025.
- [31] A. B. Matsko and V. S. Ilchenko. Optical resonators with whispering gallery modes- part i: basics. *IEEE J. Sel.Top. Quantum Electron*, 12(1):3–14, 2006.
- [32] A. B. Matsko and V. S. Ilchenko. Optical resonators with whispering gallery modes- part ii: applications. *IEEE J. Sel.Top. Quantum Electron*, 12(1):15–32, 2006.
- [33] A. Matsko. *Practical Applications of Microresonators in Optics and Photonics*. Taylor and Francis, 2009.
- [34] S. Soria, S. Berneschi, M. Brenci, F. Cosi, G. Nunzi Conti, S. Pelli, and G. C. Righini. Optical microspherical resonators for biomedical sensing. *Sensors*, 11:785–805, 2011.
- [35] Matthew R. Foreman, Wei Liang Jin, and Frank Vollmer. Optimizing detection limits in whispering gallery mode biosensing. *Optics Express*, 22(5):5491 – 5511, 2014.
- [36] G. C. Righini and S. Soria. Biosensing by WGM micro spherical resonators. *Sensors*, 16(6):905, 2016.

- 
- [37] L. Maleki and A. B. Matsko. Lithium niobate whispering gallery mode resonators: Applications and fundamental studies. *Ferroelectric Crystals for Photonics Applications*, Springer-Verlag, Berlin Heidelberg, 2009. P. Ferraro and S. Grilli and P. De Natale, Editors.
- [38] J.M. Ward, N. Dhasmana, and S. Nic Chormaic. Hollow core whispering gallery resonator sensors. *Eur. Phys. J. Special Topics*, 223:1917–1935, 2014.
- [39] J. M. Ward, Y. Yang, and S. N Chormaic. Highly sensitive temperature measurements with liquid-core microbubble resonators. *IEEE Phot. Techn. Lett.*, 25(23):2350–2353, 2013.
- [40] Kewen Han, Kaiyuan Zhu, and Gaurav Bahl. Opto-mechano-fluidic viscometer. *Appl. Phys. Lett.*, 105:014103, 2014.
- [41] K. Han, J. Kim, and G. Bahl. High-throughput sensing of freely flowing particles with optomechanofluidics. *Optica*, 3(6):585–591, 2016.
- [42] Kyu Hyun Kim, Gaurav Bahl, Wonsuk Lee, Jing Liu, Matthew Tomes, Xudong Fan, and Tal Carmon. Cavity optomechanics on a microfluidic resonator with water and viscous liquids. *Light: Science and Applications*, 2, 2013.
- [43] D. Farnesi, G.C. Righini, G. Nunzi Conti, and S. Soria. Efficient frequency generation in phoxonic cavities based on hollow whispering gallery mode resonators. *Sci.Rep.*, 7:44198, 2017.
- [44] S. Berneschi, F. Baldini, A. Barucci, A. Cosci, F. Cosi, D. Farnesi, G. Nunzi Conti, G. C. Righini, S. Soria, S. Tombelli, C. Trono, S. Pelli, and A. Giannetti. Localized biomolecules immobilization in optical microbubble resonators. *Proc. SPIE*, 9727:972719, 2016.
- [45] S. Berneschi, A. Barucci, M. Brenchi, F. Cosi, D. Farnesi, G. Nunzi Conti, S. Pelli, S. Soria, and G. C. Righini. *Optical Microbubble Resonator: A Novel Structure for Sensing Applications*, volume Sensors - Proc. First National Conference on Sensor ( Rome 15–17 February, 2012), chapter 64, pages 359–362. Springer, 2014.
- [46] S. Berneschi, D. Farnesi, F. Cosi, G. Nunzi Conti, S. Pelli, G. C. Righini, and S. Soria. High Q silica microbubble resonators fabricated by arc discharge. *Optics Letters*, 36(17):3521–3523, 2011.
- [47] M. Li, X. Wu, L. Liu, X. Fan, and L. Xu. Self-referencing optofluidic ring resonator sensor for highly sensitive biomolecular detection. *Analytical Chemistry*, 85(19):9328 – 9332, 2013.
- [48] G. Bahl, J. Zehnpfennig, M. Tomes, and T. Carmon. Stimulated optomechanical excitation of surface acoustic waves in a microdevice. *Nat. Commun.*, 2:403, 2011.

- 
- [49] K. Han, J.H. Kim, and G. Bahl. Aerostatically tunable optomechanical oscillators. *Opt. Express*, 22(2):1267–1276, 2014.
- [50] Xavier Roselló-Mechó, Daniele Farnesi, Gabriele Frigenti, Andrea Barucci, Alberto Fernández-Bienes, Tupak García-Fernández, Fulvio Ratto, Martina Delgado-Pinar, Miguel V. Andrés, Gualtiero Nunzi Conti, and Silvia Soria. Parametrical Optomechanical Oscillations in PhoXonic Whispering Gallery Mode Resonators. *Scientific Reports*, 9(1):7163, December 2019.
- [51] Gabriele Frigenti, Lucia Cavigli, Alberto Fernández-Bienes, Fulvio Ratto, Sonia Centi, Tupak García-Fernández, Gualtiero Nunzi Conti, and Silvia Soria. Resonant Microbubble as a Microfluidic Stage for All-Optical Photoacoustic Sensing. *Physical Review Applied*, 12(1):014062, July 2019.
- [52] Gabriele Frigenti, Lucia Cavigli, Alberto Fernández-Bienes, Fulvio Ratto, Sonia Centi, Tupak García-Fernández, Gualtiero Nunzi Conti, and Silvia Soria. Microbubble Resonators for All-Optical Photoacoustics of Flowing Contrast Agents. *Sensors*, 20(6):1696, March 2020.
- [53] Pierre-Henri Merrer, Khaldoun Saleh, Olivier Llopis, Simone Berneschi, Franco Cosi, and Gualtiero Nunzi Conti. Characterization technique of optical whispering gallery mode resonators in the microwave frequency domain for optoelectronic oscillators. *Appl. Opt.*, 51(20):4742–4748, Jul 2012.
- [54] G Frigenti, M Arjmand, A Barucci, F Baldini, S Berneschi, D Farnesi, M Gianfreda, S Pelli, S Soria, A Aray, Y Dumeige, P Féron, and G Nunzi Conti. Coupling analysis of high Q resonators in add-drop configuration through cavity ringdown spectroscopy. *Journal of Optics*, 20(6):065706, June 2018.
- [55] Gabriele Frigenti, Mojtaba Arjmand, Andrea Barucci, Francesco Baldini, Simone Berneschi, Daniele Farnesi, Giancarlo C. Righini, Stefano Pelli, Silvia Soria, Ayda Aray, Yannick Dumeige, Patrice Féron, and Gualtiero Nunzi Conti. Cavity-ringdown-spectroscopy-based study of high Q resonators in add-drop configuration. In Alexis V. Kudryashov, Alan H. Paxton, and Vladimir S. Ilchenko, editors, *Laser Resonators, Microresonators, and Beam Control XXI*, page 40, San Francisco, United States, March 2019. SPIE.
- [56] Srirang Manohar and Daniel Razansky. Photoacoustics: a historical review. *Adv. Opt. Photon.*, 8(4):586–617, Dec 2016.
- [57] Minghua Xu and Lihong V Wang. Photoacoustic imaging in biomedicine. *Rev. Sci. Instrum.*, page 23.
- [58] Lihong V Wang. *Photoacoustic imaging and spectroscopy*. CRC press, 2009.
- [59] Paul Beard. Biomedical photoacoustic imaging. *Interface Focus*, 1(4):602–631, August 2011.

- 
- [60] Sung-Liang Chen, L. Jay Guo, and Xueding Wang. All-optical photoacoustic microscopy. *Photoacoustics*, 3(4):143–150, December 2015.
- [61] Liang Cheng, Jingjing Liu, Xing Gu, Hua Gong, Xiaoze Shi, Teng Liu, Chao Wang, Xiaoyong Wang, Gang Liu, Huaiyong Xing, Wenbo Bu, Baoquan Sun, and Zhuang Liu. Pegylated ws2 nanosheets as a multifunctional theranostic agent for in vivo dual-modal ct/photoacoustic imaging guided photothermal therapy. *Advanced Materials*, 26(12):1886–1893, 2014.
- [62] Liwen Zhang, Shi Gao, Fan Zhang, Kai Yang, Qingjie Ma, and Lei Zhu. Activatable hyaluronic acid nanoparticle as a theranostic agent for optical/photoacoustic image-guided photothermal therapy. *ACS Nano*, 8(12):12250–12258, 2014. PMID: 25402600.
- [63] Stanislav Y. Emelianov, Pai-Chi Li, and Matthew O’Donnell. Photoacoustics for molecular imaging and therapy. *Physics Today*, 62(5):34–39, May 2009.
- [64] Srivalleesha Mallidi, Geoffrey P. Luke, and Stanislav Emelianov. Photoacoustic imaging in cancer detection, diagnosis, and treatment guidance. *Trends in Biotechnology*, 29(5):213–221, May 2011.
- [65] Yijing Liu, Pravin Bhattarai, Zhifei Dai, and Xiaoyuan Chen. Photothermal therapy and photoacoustic imaging *via* nanotheranostics in fighting cancer. *Chemical Society Reviews*, 48(7):2053–2108, 2019.
- [66] Ekaterina I. Galanzha, Evgeny V. Shashkov, Paul M. Spring, James Y. Suen, and Vladimir P. Zharov. In vivo, noninvasive, label-free detection and eradication of circulating metastatic melanoma cells using two-color photoacoustic flow cytometry with a diode laser. *Cancer Research*, 69(20):7926–7934, 2009.
- [67] L. V. Wang and S. Hu. Photoacoustic Tomography: In Vivo Imaging from Organelles to Organs. *Science*, 335(6075):1458–1462, March 2012.
- [68] Biqin Dong, Hao Li, Zhen Zhang, Kevin Zhang, Siyu Chen, Cheng Sun, and Hao F. Zhang. Isometric multimodal photoacoustic microscopy based on optically transparent micro-ring ultrasonic detection. *Optica*, 2(2):169, February 2015.
- [69] Leonid Vigderman and Eugene R. Zubarev. High-Yield Synthesis of Gold Nanorods with Longitudinal SPR Peak Greater than 1200 nm Using Hydroquinone as a Reducing Agent. *Chemistry of Materials*, 25(8):1450–1457, April 2013.
- [70] Judith Weber, Paul C Beard, and Sarah E Bohndiek. Contrast agents for molecular photoacoustic imaging. *Nature Methods*, 13(8):639–650, August 2016.
- [71] Pandian Senthil Kumar, Isabel Pastoriza-Santos, Benito Rodríguez-González, F Javier García de Abajo, and Luis M Liz-Marzán. High-yield synthesis and optical response of gold nanostars. *Nanotechnology*, 19(1):015606, January 2008.

- 
- [72] J Perezjuste, I Pastorizasantos, L Lizmarzan, and P Mulvaney. Gold nanorods: Synthesis, characterization and applications. *Coordination Chemistry Reviews*, 249(17-18):1870–1901, September 2005.
- [73] Qinrui Fu, Rong Zhu, Jibin Song, Huanghao Yang, and Xiaoyuan Chen. Photoacoustic Imaging: Contrast Agents and Their Biomedical Applications. *Advanced Materials*, page 1805875, December 2018.
- [74] Adam De La Zerda, Cristina Zavaleta, Shay Keren, Srikant Vaithilingam, Sunil Bodapati, Zhuang Liu, Jelena Levi, Bryan R. Smith, Te-Jen Ma, Omer Oralkan, Zhen Cheng, Xiaoyuan Chen, Hongjie Dai, Butrus T. Khuri-Yakub, and Sanjiv S. Gambhir. Carbon nanotubes as photoacoustic molecular imaging agents in living mice. *Nature Nanotechnology*, 3(9):557–562, September 2008.
- [75] Georg Wissmeyer, Miguel A. Pleitez, Amir Rosenthal, and Vasilis Ntziachristos. Looking at sound: optoacoustics with all-optical ultrasound detection. *Light: Science & Applications*, 7(1):53, December 2018.
- [76] Adam Maxwell, Sheng-Wen Huang, Tao Ling, Jin-Sung Kim, Shai Ashkenazi, and L. Jay Guo. Polymer Microring Resonators for High-Frequency Ultrasound Detection and Imaging. *IEEE Journal of Selected Topics in Quantum Electronics*, 14(1):191–197, 2008.
- [77] Cheng Zhang, Sung-Liang Chen, Tao Ling, and L. Jay Guo. Review of Imprinted Polymer Microrings as Ultrasound Detectors: Design, Fabrication, and Characterization. *IEEE Sensors Journal*, 15(6):3241–3248, June 2015.
- [78] Philip McCord Morse and K Uno Ingard. *Theoretical acoustics*. Princeton university press, 1986.
- [79] Ahmad Safari and E Koray Akdogan. *Piezoelectric and acoustic materials for transducer applications*. Springer Science & Business Media, 2008.
- [80] Lucia Cavigli, Sonia Centi, Sarah Lai, Claudia Borri, Filippo Micheletti, Paolo Tortoli, Ilaria Panettieri, Ingolf Streit, Francesca Rossi, Fulvio Ratto, and Roberto Pini. Light and ultrasound activated microbubbles around gold nanorods for photoacoustic microsurgery. In Vasilis Ntziachristos and Roger Zemp, editors, *Opto-Acoustic Methods and Applications in Biophotonics III*, page 7, Munich, Germany, August 2017. SPIE.
- [81] Lucia Cavigli, Alberto Cini, Sonia Centi, Claudia Borri, Sarah Lai, Fulvio Ratto, Marella de Angelis, and Roberto Pini. Photostability of Gold Nanorods upon Endosomal Confinement in Cultured Cells. *The Journal of Physical Chemistry C*, 121(11):6393–6400, March 2017.
- [82] Lucia Cavigli, Sonia Centi, Claudia Borri, Paolo Tortoli, Ilaria Panettieri, Ingolf Streit, Daniele Ciofini, Giada Magni, Francesca Rossi, Salvatore Siano, Fulvio Ratto, and Roberto Pini. 1064-nm-resonant gold nanorods for photoacoustic

- theranostics within permissible exposure limits. *Journal of Biophotonics*, 12(10), October 2019.
- [83] Ming Li, Xiang Wu, Liying Liu, Xudong Fan, and Lei Xu. Self-Referencing Optofluidic Ring Resonator Sensor for Highly Sensitive Biomolecular Detection. *Analytical Chemistry*, 85(19):9328–9332, October 2013.
- [84] Kyu Hyun Kim, Wei Luo, Cheng Zhang, Chao Tian, L. Jay Guo, Xueding Wang, and Xudong Fan. Air-coupled ultrasound detection using capillary-based optical ring resonators. *Scientific Reports*, 7(1):109, December 2017.
- [85] Zihao Li, Chenggang Zhu, Zhihe Guo, Bowen Wang, Xiang Wu, and Yiyan Fei. Highly Sensitive Label-Free Detection of Small Molecules with an Optofluidic Microbubble Resonator. *Micromachines*, 9(6):274, May 2018.
- [86] Vladimir P. Zharov, Ekaterina I. Galanzha, Evgeny V. Shashkov, Nicolai G. Khlebtsov, and Valery V. Tuchin. In vivo photoacoustic flow cytometry for monitoring of circulating single cancer cells and contrast agents. *Opt. Lett.*, 31(24):3623–3625, Dec 2006.
- [87] Ekaterina I. Galanzha and Vladimir P. Zharov. Photoacoustic flow cytometry. *Methods*, 57(3):280–296, July 2012.
- [88] Dmitry A. Nedosekin, Tariq Fahmi, Zeid A. Nima, Jacqueline Nolan, Chengzhong Cai, Mustafa Sarimollaoglu, Enkeleda Dervishi, Alexei Basnakian, Alexandru S. Biris, and Vladimir P. Zharov. Photoacoustic flow cytometry for nanomaterial research. *Photoacoustics*, 6:16–25, June 2017.
- [89] Vaskar Gnyawali, Eric M. Strohm, Jun-Zhi Wang, Scott S. H. Tsai, and Michael C. Kolios. Simultaneous acoustic and photoacoustic microfluidic flow cytometry for label-free analysis. *Scientific Reports*, 9(1):1585, December 2019.
- [90] Fei Liu, Tian Jin, Ruopeng Yan, Tingting Li, Biao Hu, Lei Yao, Tianye Huang, Chaolong Song, and Lei Xi. An opto-acousto-fluidic microscopic system with a high spatiotemporal resolution for microfluidic applications. *Opt. Express*, 27(2):1425–1432, Jan 2019.
- [91] Jonathan P. Dowling and Gerard J. Milburn. Quantum technology: the second quantum revolution. *Philosophical Transactions of the Royal Society of London. Series A: Mathematical, Physical and Engineering Sciences*, 361(1809):1655–1674, August 2003.
- [92] Jeremy L. O’Brien, Akira Furusawa, and Jelena Vučković. Photonic quantum technologies. *Nature Photonics*, 3(12):687–695, December 2009.
- [93] Alán Aspuru-Guzik and Philip Walther. Photonic quantum simulators. *Nature Physics*, 8(4):285–291, April 2012.

- 
- [94] Max F Riedel, Daniele Binosi, Rob Thew, and Tommaso Calarco. The European quantum technologies flagship programme. *Quantum Science and Technology*, 2(3):030501, September 2017.
- [95] Jianwei Wang, Fabio Sciarrino, Anthony Laing, and Mark G. Thompson. Integrated photonic quantum technologies. *Nature Photonics*, 14(5):273–284, May 2020.
- [96] Igor Aharonovich, Dirk Englund, and Milos Toth. Solid-state single-photon emitters. *Nature Photonics*, 10(10):631–641, October 2016.
- [97] Brahim Lounis and Michel Orrit. Single-photon sources. *Reports on Progress in Physics*, 68(5):1129–1179, May 2005.
- [98] Th. Basché, W. E. Moerner, M. Orrit, and H. Talon. Photon antibunching in the fluorescence of a single dye molecule trapped in a solid. *Physical Review Letters*, 69(10):1516–1519, September 1992.
- [99] Ph. Tamarat, A. Maali, B. Lounis, and M. Orrit. Ten Years of Single-Molecule Spectroscopy. *The Journal of Physical Chemistry A*, 104(1):1–16, January 2000.
- [100] B. Lounis and W. E. Moerner. Single photons on demand from a single molecule at room temperature. *Nature*, 407(6803):491–493, September 2000.
- [101] Sofia Pazzagli, Pietro Lombardi, Daniele Martella, Maja Colautti, Bruno Tiribilli, Francesco Saverio Cataliotti, and Costanza Toninelli. Self-Assembled Nanocrystals of Polycyclic Aromatic Hydrocarbons Show Photostable Single-Photon Emission. *ACS Nano*, 12(5):4295–4303, May 2018.
- [102] T. Grange, N. Somaschi, C. Antón, L. De Santis, G. Coppola, V. Giesz, A. Lemaître, I. Sagnes, A. Auffèves, and P. Senellart. Reducing phonon-induced decoherence in solid-state single-photon sources with cavity quantum electrodynamics. *Phys. Rev. Lett.*, 118:253602, Jun 2017.
- [103] Zhao-Chen Duan, Yu-Hao Deng, Ying Yu, Si Chen, Jian Qin, Hui Wang, Xing Ding, Li-Chao Peng, Christian Schneider, Da-Wei Wang, Sven Höfling, Jonathan P. Dowling, Chao-Yang Lu, and Jian-Wei Pan. Quantum beat between sunlight and single photons. *Nano Letters*, 20(1):152–157, 2020. PMID: 31841348.
- [104] Rosa Brouri, Alexios Beveratos, Jean-Philippe Poizat, and Philippe Grangier. Photon antibunching in the fluorescence of individual color centers in diamond. *Opt. Lett.*, 25(17):1294–1296, Sep 2000.
- [105] Elke Neu, David Steinmetz, Janine Riedrich-Möller, Stefan Gsell, Martin Fischer, Matthias Schreck, and Christoph Becher. Single photon emission from silicon-vacancy colour centres in chemical vapour deposition nano-diamonds on iridium. *New Journal of Physics*, 13(2):025012, feb 2011.

- 
- [106] P. Lombardi, A. P. Ovyvan, S. Pazzagli, G. Mazzamuto, G. Kewes, O. Neitzke, N. Gruhler, O. Benson, W. H. P. Pernice, F. S. Cataliotti, and C. Toninelli. Photostable molecules on chip: Integrated single photon sources for quantum technologies. In *2017 Conference on Lasers and Electro-Optics Europe & European Quantum Electronics Conference (CLEO/Europe-EQEC)*, pages 1–1, Munich, June 2017. IEEE.
- [107] Matthew Pelton, Charles Santori, Jelena Vuckovic, Bingyang Zhang, Glenn S. Solomon, Jocelyn Plant, and Yoshihisa Yamamoto. Efficient Source of Single Photons: A Single Quantum Dot in a Micropost Microcavity. *Physical Review Letters*, 89(23):233602, November 2002.
- [108] V. Giesz, S. L. Portalupi, T. Grange, C. Antón, L. De Santis, J. Demory, N. Somaschi, I. Sagnes, A. Lemaître, L. Lanco, A. Auffèves, and P. Senellart. Cavity-enhanced two-photon interference using remote quantum dot sources. *Phys. Rev. B*, 92:161302, Oct 2015.
- [109] M. Brune, F. Schmidt-Kaler, A. Maali, J. Dreyer, E. Hagley, J. M. Raimond, and S. Haroche. Quantum rabi oscillation: A direct test of field quantization in a cavity. *Phys. Rev. Lett.*, 76:1800–1803, Mar 1996.
- [110] Karl H. Drexhage. Iv interaction of light with monomolecular dye layers. volume 12 of *Progress in Optics*, pages 163 – 232. Elsevier, 1974.
- [111] X. Fan, P. Palinginis, S. Lacey, and H. Wang. Coupling semiconductor nanocrystals to a fused-silica microsphere: a quantum-dot microcavity with external high  $Q$  factors. *Optics Letters*, 25(21):1600–1602, 2000.
- [112] J. Haase, S. Shinohara, P. Mundra, G. Risse, V. G. Lyssenko, H. Fröb, M. Hentschel, A. Eychemüller, and K. Leo. Hemispherical resonators with embedded nanocrystal quantum rod emitters. *Applied Physics Letters*, 97:211101, 2010.
- [113] Wolf von Klitzing, Romain Long, Vladimir S. Ilchenko, Jean Hare, and Valérie Lefèvre-Seguin. Frequency tuning of the whispering-gallery modes of silica microspheres for cavity quantum electrodynamics and spectroscopy. *Optics Letters*, 26(3):166–168, 2001.
- [114] Peng-Bo Li, Shao-Yan Gao, and Fu-Li Li. Quantum information transfer with nitrogen-vacancy centers coupled to a whispering-gallery microresonator. *Phys. Rev. A*, 83:054306, 2011.
- [115] S. M. Spillane, T. J. Kippenberg, K. J. Vahala, K. W. Goh, E. Wilcut, and H. J. Kimble. Ultrahigh-q toroidal microresonators for cavity quantum electrodynamics. *Physical Review A*, 71:013817, 2005.
- [116] Y.Z. Wang, B.L. Lu, Y.Q. Li, and Y.S. Liu. Observation of cavity quantum electrodynamic effects in  $Nd$ :glass microsphere. *Optics Letters*, 20:770–772, 1995.



- 
- [117] P.E. Barclay, C. Santori, K.-M.Fu, R.G.Beausolei, and O. Painter. Coherent interference effects in a nano-assembled diamond nv center cavity-qed system. *Opt. Express*, 17:8081–8097, 2009.
- [118] Gabija Kiršanskė, Henri Thyrrestrup, Raphaël S. Daveau, Chris L. Dreeßen, Tommaso Pregolato, Leonardo Midolo, Petru Tighineanu, Alisa Javadi, Søren Stobbe, Rüdiger Schott, Arne Ludwig, Andreas D. Wieck, Suk In Park, Jin D. Song, Andreas V. Kuhlmann, Immo Söllner, Matthias C. Löbl, Richard J. Warburton, and Peter Lodahl. Indistinguishable and efficient single photons from a quantum dot in a planar nanobeam waveguide. *Phys. Rev. B*, 96:165306, Oct 2017.
- [119] M. Arcari, I. Söllner, A. Javadi, S. Lindskov Hansen, S. Mahmoodian, J. Liu, H. Thyrrestrup, E. H. Lee, J. D. Song, S. Stobbe, and P. Lodahl. Near-unity coupling efficiency of a quantum emitter to a photonic crystal waveguide. *Phys. Rev. Lett.*, 113:093603, Aug 2014.
- [120] S. M. Mansfield and G. S. Kino. Solid immersion microscope. *Applied Physics Letters*, 57(24):2615–2616, 1990.
- [121] C. Toninelli, I. Gerhardt, A. S. Clark, A. Reserbat-Plantey, S. Götzinger, Z. Ristanovic, M. Colautti, P. Lombardi, K. D. Major, I. Deperasińska, W. H. Pernice, F. H. L. Koppens, B. Kozankiewicz, A. Gourdon, V. Sandoghdar, and M. Orrit. Single organic molecules for photonic quantum technologies, 2020.
- [122] Sanli Faez, Pierre Türschmann, Harald R. Haakh, Stephan Götzinger, and Vahid Sandoghdar. Coherent interaction of light and single molecules in a dielectric nanoguide. *Phys. Rev. Lett.*, 113:213601, Nov 2014.
- [123] Stéphane Balac and Patrice Féron. Whispering gallery modes volume computation in optical micro-spheres. [*Research Report*] *FOTON, UMR CNRS 6082*, 2014.
- [124] Stéphane Balac. WGMode : A Matlab toolbox for whispering gallery modes volume computation in spherical optical micro-resonators. *Computer Physics Communications*, 243:121–134, October 2019.
- [125] Ian M. White, Hesam Oveys, and Xudong Fan. Liquid-core optical ring-resonator sensors. *Opt. Lett.*, 31(9):1319–1321, May 2006.
- [126] Clifford R. Pollock. *Clifford R. Pollock-Fundamentals of optoelectronics-Irwin (1995).djvu*. Irwin, 1995.
- [127] B.E. Little, J.-P. Laine, and H.A. Haus. Analytic theory of coupling from tapered fibers and half-blocks into microsphere resonators. *Journal of Lightwave Technology*, 17(4):704–715, April 1999.
- [128] H. Haus, W. Huang, S. Kawakami, and N. Whitaker. Coupled-mode theory of optical waveguides. *Journal of Lightwave Technology*, 5(1):16–23, 1987.

- 
- [129] Milton Abramovitz and Irene A. Stegun. *Handbook of Mathematical Functions*. Us department of commerce, national bureau of standards edition, 1964.
- [130] Gabriele Frigenti. Microbubble whispering gallery mode resonator as an all-optical platform for the characterisation of photoacoustics contrast agents. *Il Nuovo Cimento C*, 43:127.
- [131] Amy Watkins, Jonathan Ward, Yuqiang Wu, and Síle Nic Chormaic. Single-input spherical microbubble resonator. *Opt. Lett.*, 36(11):2113–2115, June 2011.
- [132] Alessandro Cosci, Simone Berneschi, Ambra Giannetti, Daniele Farnesi, Franco Cosi, Francesco Baldini, Gualtiero Nunzi Conti, Silvia Soria, Andrea Barucci, Giancarlo Righini, and Stefano Pelli. Resonance Frequency of Optical Microbubble Resonators: Direct Measurements and Mitigation of Fluctuations. *Sensors*, 16(9):1405, August 2016.
- [133] Luciano Bachmann, Denise Maria Zzell, and Edison Puig Maldonado. Determination of Beam Width and Quality for Pulsed Lasers Using the Knife-Edge Method. *Instrumentation Science & Technology*, 31(1):47–52, January 2003.
- [134] A. Yariv. Universal relations for coupling of optical power between microresonators and dielectric waveguides. *Electronics Letters*, 36(4):321, 2000.
- [135] Alessandro Cosci, Franco Quercioli, Daniele Farnesi, Simone Berneschi, Franco Cosi, Andrea Barucci, Gualtiero Nunzi Conti, Giancarlo Righini, and Stefano Pelli. Confocal reflectance microscopy for determination of microbubble resonator thickness. *Optics Express*, page 9, 2015.
- [136] T Toyoda and M Yabe. The temperature dependence of the refractive indices of fused silica and crystal quartz. *Journal of Physics D: Applied Physics*, 16(5):L97–L100, May 1983.
- [137] Joseph A. Curcio and Charles C. Petty. The Near Infrared Absorption Spectrum of Liquid Water. *Journal of the Optical Society of America*, 41(5):302, May 1951.
- [138] Maja Colautti. *Integrated single-molecule based single-photon sources for photonic quantum technologies*. PhD thesis, Università degli Studi di Firenze, 2020.
- [139] E. T. Jaynes and F. W. Cummings. Comparison of quantum and semiclassical radiation theories with application to the beam maser. *Proceedings of the IEEE*, 51(1):89–109, 1963.
- [140] Christopher Gerry, Peter Knight, and Peter L Knight. *Introductory quantum optics*. Cambridge university press, 2005.
- [141] Daniel F Walls and Gerard J Milburn. *Quantum optics*. Springer Science & Business Media, 2007.

- [142] Thomas Grange, Gaston Hornecker, David Hunger, Jean-Philippe Poizat, Jean-Michel Gérard, Pascale Senellart, and Alexia Auffèves. Cavity-Funneled Generation of Indistinguishable Single Photons from Strongly Dissipative Quantum Emitters. *Physical Review Letters*, 114(19):193601, May 2015.
- [143] H. J. Kimble. Strong Interactions of Single Atoms and Photons in CavityQED. *Physica Scripta*, T76(1):127, 1998.
- [144] W. W. Hansen. A New Type of Expansion in Radiation Problems. *Physical Review*, 47(2):139–143, January 1935.
- [145] Julius Adams Stratton. *Electromagnetic theory*. Wiley IEEE Press Series, 2007.
- [146] F Bowman. *Introduction to Bessel Functions*. Dover Publications, 1958.